Electrical and Computer Engineering ETDs   Engineering ETDs

1-30-2013

Detection and Classification of Diabetic Retinopathy Pathologies in Fundus Images

Carla Paola Agurto Rios

Follow this and additional works at: https://digitalrepository.unm.edu/ece_etds

Carla Paola Agurto Rios

Candidate

Electrical and Computer Engineering

Department

This dissertation is approved, and it is acceptable in quality and form for publication:

Approved by the Dissertation Committee:

MARIOS PATTICHIS , Chairperson

RAMIRO JORDAN

SIMON BARRIGA

ROBERT AVERY

Detection and Classification of Diabetic Retinopathy Pathologies in Fundus Images

BY

CARLA AGURTO

B.Sc., Electrical Engineering, Pontificia Universidad Católica del
Perú, 2004
M.Sc., Computer Engineering, University of New Mexico, 2009
PhD., Computer Engineering, University of New Mexico, 2012

DISSERTATION

Submitted in Partial Fulfillment of the
Requirements for the Degree of

Doctor of Philosophy
Engineering

The University of New Mexico
Albuquerque, New Mexico

Dec, 2012

DEDICATION

To God, who always helps me,

to my family, who always supports me,

and especially to my husband, who always

understands me, encourages me and makes me

happy.

"Success is not the key to happiness. Happiness is the key to success.
If you love what you are doing, you will be successful."

Albert Schweitzer

Acknowledgments

I would like to express my gratitude to Marios, my advisor, for all the support he has given me all these years. Besides helping me acquire knowledge in this field, he has always supported his students and helped them with any kind of problem.

I would also like to thank Pete, my boss, for all the help I have received from him. From him, I learned that engineers really grow when they work with people from other specialties. Now, I like medical imaging much more.

In addition, I want to thank Simon for being a good bridge between my studies and my job, for all his advice, and for the time he spent reviewing all of my papers.

Special thanks to Sheila, whose medical knowledge and advice were very helpful all these years, and to Eduardo, Vico, Daniel, Honggang, Elizabeth, and all the people that have contributed in different ways to the completion of this work.

Detection and Classification of Diabetic Retinopathy Pathologies in Fundus Images

by

Carla Agurto

B.Sc., Electrical Engineering, Pontificia Universidad Católica del Perú, 2004

M.Sc., Computer Engineering, University of New Mexico, 2009

PhD., Engineering, University of New Mexico, 2012

Abstract

Diabetic Retinopathy (DR) is a disease that affects up to 80% of diabetics around the world. It is the second greatest cause of blindness in the Western world, and one of the leading causes of blindness in the U.S. Many studies have demonstrated that early treatment can reduce the number of sight-threatening DR cases, mitigating the medical and economic impact of the disease.

Accurate, early detection of eye disease is important because of its potential to reduce rates of blindness worldwide. Retinal photography for DR has been promoted for decades for its utility in both disease screening and clinical research studies. In recent years, several research centers have presented systems to detect pathology in retinal images. However, these approaches apply specialized algorithms to detect specific types of lesion in the retina. In order to detect multiple lesions, these systems generally implement multiple algorithms. Furthermore, some of these studies evaluate their algorithms on a single dataset, thus avoiding potential problems associated with the differences in fundus imaging devices, such as camera resolution.

These methodologies primarily employ bottom-up approaches, in which the accurate segmentation of all the lesions in the retina is the basis for correct determination. A disadvantage of bottom-up approaches is that they rely on the accurate segmentation of all lesions in order to measure performance. On the other hand, top-down approaches do not depend on the segmentation of specific lesions. Thus, top-down methods can potentially detect abnormalities not explicitly used in their training phase. A disadvantage of these methods is that they cannot identify specific pathologies and require large datasets to build their training models.

In this dissertation, I merged the advantages of the top-down and bottom-up approaches to detect DR with high accuracy. First, I developed an algorithm based on a top-down approach to detect abnormalities in the retina due to DR. By doing so, I was able to evaluate DR pathologies other than microaneurysms and exudates, which are the main focus of most current approaches. In addition, I demonstrated good generalization

capacity of this algorithm by applying it to other eye diseases, such as age-related macular degeneration.

Due to the fact that high accuracy is required for sight-threatening conditions, I developed two bottom-up approaches, since it has been proven that bottom-up approaches produce more accurate results than top-down approaches for particular structures. Consequently, I developed an algorithm to detect exudates in the macula. The presence of this pathology is considered to be a surrogate for clinical significant macular edema (CSME), a sight-threatening condition of DR.

The analysis of the optic disc is usually not taken into account in DR screening systems. However, there is a pathology called neovascularization that is present in advanced stages of DR, making its detection of crucial clinical importance. In order to address this problem, I developed an algorithm to detect neovascularization in the optic disc.

These algorithms are based on amplitude-modulation and frequency-modulation (AM-FM) representations, morphological image processing methods, and classification algorithms. The methods were tested on a diverse set of large databases and are considered to be the state-of the art in this field.

Table of Contents

List of Figures

List of Tables

Chapter 1: Introduction

1.1 Motivation

According to the International Diabetes Federation, throughout the world, in 2010, the number of people with diabetes had reached 285 million [1]. "Bad habits" in the population such as lack of exercise, consumption of fast food with high content of fat, etc. contribute to the increase of overweight population that leads to diabetes type II. For this reason, the number of diabetes cases is increasing each year making it difficult for the health care system to screen all of diabetic people for retinopathy. As an alternative to help cover the high demand, automatic Diabetic Retinopathy (DR) screening algorithms have been developed using fundus images.

The motivation of this work is to apply different image analysis techniques for the detection of pathologies associated with DR in the retina with more emphasis on the detection of two sight threatening diseases that can lead to severe vision damage. First, we develop an image analysis algorithm to detect abnormalities in the macula, in which high visual resolution is obtained, to look for macular edema. Second, we propose to develop an algorithm to detect neovascularization. Neovascularization in the optic disc can produce significant problems since it can produce hemorrhages that can cause significant vision impairment.

We expect that by developing and applying these algorithms to actual patients, we can achieve early detection of critical diseases. Then, this early detection will lead to timely treatment that can prevent blindness.

1.2 Thesis statement

This PhD dissertation research will develop image processing techniques for the classification of diabetic retinopathy. New image analysis methods will be developed for the detection and identification of pathologies in the macula area of the retina. Special emphasis will be placed in detecting neovascularization in the optic disc (NVD). These algorithms are based on the use of multi-scale AM-FM representations. The main interest of this dissertation topic is to help develop an eye disease screening system for application to large populations.

1.3 Innovations and Contributions

A list of the primary innovations and contributions includes:

- Development of an image processing system through the integration of existing image processing components for detecting diabetic retinopathy lesions (excluding diseases in the optic disc, but see below). Specific contributions include: feature selection, characterization of the lesions based on AM-FM scales, classifier design, and system validation.

- A new image processing algorithm to detect the presence of exudates in the macula which are surrogates for a sight threatening condition called clinical significant macular edema (CSME)

- A new image processing algorithm for the detection of neovascularization in the optic disc.

1.4 Organization

This dissertation is organized into seven chapters. In what follows, a summary of each chapter is provided.

In chapter 2, a literature review of the most relevant approaches developed to detect abnormalities in the retina as a consequence of diabetic retinopathy is presented. In this review, diabetic retinopathy (DR) screening is presented, as well as all the modules required by a system in order to successfully detect the presence of these lesions. In this chapter, retinal image acquisition, image quality assessment, vasculature segmentation, detection and segmentation of the optic disc, detection of DR pathologies is described as well as the current methodologies to assess them. The material presented will be submitted for publication:

- C. Agurto, H. Yu, J. Wigdahl, M. S. Pattichis, S. Nemeth, S. Barriga and P. Soliz, "Literature review of processing methods for diabetic retinopathy screening using fundus images," *to be submitted for publication.*

In chapter 3, a new approach developed to capture the presence of pathologies in the retina is presented. This material is the study of more than 2 years of how a technique implemented in [2] of amplitude modulation-frequency modulation can be used to detect the presence of these pathologies. The work presented in this chapter has been published in two journal papers:

- C. Agurto, V. Murray, S. Barriga, S. Murillo, M. S. Pattichis, H. Davis, S. Russell, M. D. Abramoff and P. Soliz, Multiscale AM-FM Methods for Diabetic Retinopathy Lesion Detection, *IEEE Transactions on Medical Imaging.*, vol. 29, no. 2, pp. 502-512, 2010.

- C. Agurto, S Barriga, V Murray, S Nemeth, M Pattichis, W Bauman, G Zamora, and P Soliz, "Automatic algorithm for detection of diabetic retinopathy pathologies", *Invest Ophthalmol Vis Sci.,* vol. 52, no. 8, pp. 5862-5871, 2011.

The content of both papers was modified in order to provide a better understanding to the reader.

In chapter 4, we present an approach that was developed in order to detect lesions in the macula related to DR. These lesions are microaneuryms, hemorrhages, and hard exudates. The material presented in this chapter was presented at:

- C Agurto, H Yu, V Murray, M Pattichis, S Barriga, P Soliz, "Detection of Hard Exudates and Red Lesions in the Macula Using a Multiscale Approach", *IEEE Southwest Symposium on Image Analysis and Interpretation*, 1043, 2012.

Chapter 5 presents a modification of the algorithm presented in Chapter 4. This algorithm was tuned to obtain high accuracy in the detection of exudates in the macula. This algorithm includes color normalization. In addition, we modified the optimization procedure to be more robust in presence of noise and tested in two large databases (1000 images). This material has been submitted for publication:

- C. Agurto, V. Murray, H. Yu, M. S. Pattichis, S. Nemeth, S. Barriga and P. Soliz, "Detection of hard exudates in the macula using a multiscale amplitude-modulation frequency-modulation analysis," *submitted to Transactions on Medical Imaging.*

Chapter 6 presents a method to detect neovascularization in the optic disc. This method is based on the characterization of the vasculature in the optic disc. The algorithm was successfully applied to a 300 images (200 control). The material of this chapter has been submitted for publication:

- C. Agurto, H. Yu, V. Murray, M. S. Pattichis, S. Nemeth, S. Barriga and P. Soliz, "A Multiscale Decomposition Approach to Detect Neovascularization in the Optic Disc," *submitted to Transactions on Medical Imaging.*

Finally, in chapter 7, we present conclusions, future work, and recommendations. Additionally the document has an appendix section with the list of publications related with this dissertation

Chapter 2: Image Processing Methods for Diabetic Retinopathy Screening using fundus images

Abstract

The number of blind people is increasing at higher rates than ever before. Recent studies have demonstrated that the number of cases with diabetic retinopathy (DR) has increased by 89% since 2000. To provide healthcare for the high number of diabetics, a means for large scale retinal screening systems will be needed. This work presents an introduction to techniques which have been applied to the analysis of DR digital images. Specifically, this paper will focus on the previously published algorithms to detect DR. Components of DR screening systems that are reported in the literature are composed of the following modules: retinal image acquisition, image quality verification, pre-processing, vasculature segmentation, optic disc detection and segmentation, macula localization, and detection of lesions. The algorithms implemented for each module throughout the years are analyzed sequentially in time until early 2012. In addition, the latest results of the DR screening systems are discussed. This review will provide researchers a broader knowledge of this area and it will encourage people from multi-disciplinary fields of study to provide solutions to the limitations of the current algorithms, thus improving the capabilities and the robustness of DR screening systems.

2.1 Introduction

Diabetes is a group of metabolic diseases characterized by hyperglycemia, or high

blood sugar, resulting from defects in insulin secretion, insulin action, or both. Chronic hyperglycemia from diabetes is associated with long-term damage especially the eyes, kidney, nerves, heart and blood vessels. The global number of predicted increases in the prevalence of diabetes is staggering. In the United States, the prevalence of Type 2 diabetes has tripled since the 1980s, while the health care costs surrounding diabetes is projected to rise from the present $194 billion to $500 billion by 2020 [3].

Diabetic retinopathy (DR) is a term applied to the effects of diabetes in the eye, or more specifically, the specialized neural tissue in the eye, the retina. DR affects up to 80% of diabetics around the world and it is one of the leading causes of blindness in the U.S. It is the second greatest cause of blindness in the western world, and the leading cause of blindness among people of working age [4]. The prevalence rate for retinopathy for adults aged 40 years and older in the United States is 3.4% (4.1 million persons); the prevalence rate for vision-threatening retinopathy (the most visually damaging type) is 0.75% (899,000) [5]. Assuming a similar prevalence of diabetes mellitus, the projected numbers in 2020 would be 6 million persons with DR and 1.34 million with the sight-threatening type.

Many studies have demonstrated that early detection and early treatment can reduce the amount of DR cases, mitigating the medical and economic impacts of the disease [6]. Accurate, early detection of eye disease using retinal photography, also known as retinal screening, is important because of its potential for reducing the number of cases of blindness around the world. Systematic screening for DR using retinal photography has been shown to reduce the incidence of blindness among people with diabetes [7], [8], [9]. In Britain, there was substantial evidence that supported the introduction of a national

screening program for DR, and in 2000, they began the introduction of a systemic national screening program based on digital photography, which successfully continues to this day [10], [11]. Digital Retinal images are amenable to the application of sophisticated image analysis techniques that can assist in the screening process by creating more efficiency in the grading/reading process and consequently increasing the throughput as the demand simultaneously increases. The aim of the automatic screening algorithms is to detect lesions of DR and refer the patients to an eye care provider when abnormalities which are considered high risk are found in the retinal fundus images. In this way two purposes can be achieved: 1) Evaluation and timely referral for treatment in the DR population, and 2) Increased efficiency in the use of healthcare resources for those that require the timeliest care.

This paper is organized as follows: In section 2.2, a discussion of the relevant retina anatomy is presented. The goal of the anatomical discussion is to present some basic information to understand the eye disease associated with DR. Diabetes and its consequences are described in section 2.3, and a more detailed explanation of DR is presented in section 2.4. In section 2.5, we present different image processing methods associated with a general automated DR screening system, from the first approaches to the state of the art in algorithms to assess the quality of the image, locate and segment the optic disc, macula and fovea localization, segmentation of the retinal vasculature and detection of pathologies. In addition, we present the latest results of implemented DR screening systems. Finally in section 2.6, we discuss each of these modules.

2.2 The Retina

An anatomical view of the human eye is shown in Fig. 2.1 [12]. The retina contains the photochemicals and neurologic connections that process light energy. It is composed of two types of photoreceptors: rods and cones. These photoreceptors convert the light into electromagnetic waves, which are subsequently transmitted to the visual cortex of the brain through the optic nerve. These structures allow us to see approximately a 140-degree field horizontally [13]. The retina, which receives all the visual information, has an extension of 32 mm from ora to ora along the horizontal meridian. The area of the human retina is $1094mm^2$, calculated from the assumption that the average length of the human eye is 22 mm from anterior to posterior poles, and that the retina occupies 72% of the area inside of the globe [14]. Fig. 2.2 shows the most relevant features in the retina. These are: arteries, veins, optic nerve head, and fovea. The dimensions of the optic nerve head or disc (the term used for the presentation of the optic nerve as it appears in the posterior segment of the eye) are 1.86 mm vertically by 1.75 mm horizontally on average. In [15], the variation of disc size diameter is measured between individuals. They found a range of 0.96 to 2.91 mm for the vertical axis and 0.91 to 2.61 mm for the horizontal axis. An extremely critical landmark of the retina is the fovea since it has the most concentration of photoreceptors in the retina. The fovea sits in the center of the macula, which is 1.5mm of the central retina. The fovea represents the center, or peak, of highest visual resolution and the site of the most detailed color vision. The normal macula appears darker than the rest of the retina because of an increase in the amount of melanin at this location, which is a pigment that helps absorb light. Any disease which affects the macula will directly affect visual resolution, or clinically known as visual acuity. Age-

related macular degeneration, known as ARMD, is a relatively common cause of acquired central visual loss in the over 60 year old age group. In this disorder, the macula is affected by degeneration of one of the posterior layers of the retina or by aberrant new blood vessels which grow and bleed under the retina, causing destruction to fine, central vision.
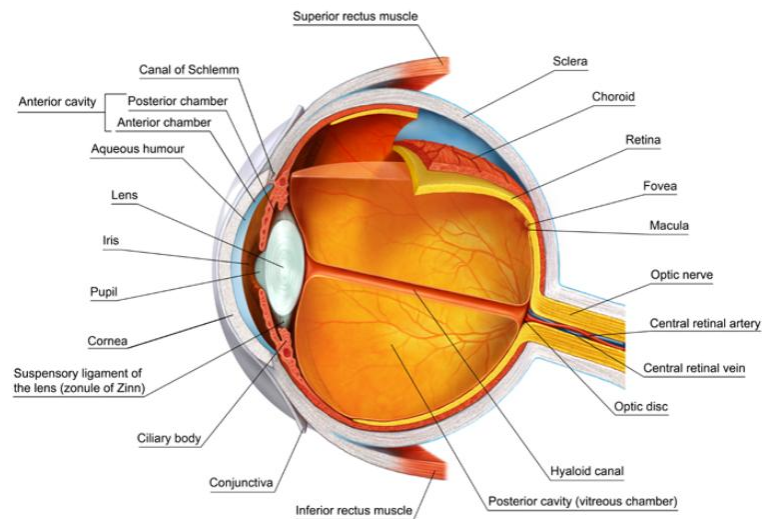
Figure 2.1 Eye anatomy and retinal layers. (Image courtesy of [7])
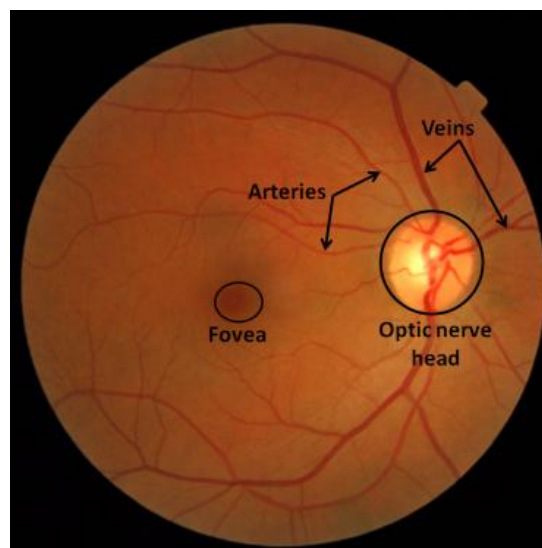
Figure 2.2 Parts of the retina in a fundus image.

2.3 Diabetes

Diabetes is a group of metabolic diseases characterized by hyperglycemia, or high blood sugar, resulting from defects in insulin secretion, insulin action, or both. Insulin is a hormone that is made by cells of the pancreas and is critical in assisting glucose (sugar) in entering the body's cells for constant energy and brain function. It is the major fuel-regulating hormone of the body and human survival is dependent on it. Diabetes is classified in three different types: Type 1, Type 2, and gestational diabetes. Type 1 is associated with an absolute lack of insulin production and accounts for 5-10% of those with diabetes, and was previously known as juvenile-onset diabetes. Type 1 is a consequence of a cellular-mediated autoimmune destruction of the beta cells of the pancreas. Once diagnosed, these patients will require insulin injections the rest of their lives. Type 1 is most commonly diagnosed in children 9-16 years of age. Type 2, also known as adult-onset diabetes, accounts for approximate 90-95% of those with diabetes. This large category of diabetics encompasses individuals who have insulin resistance and can have relative insulin deficiency. Many patients who have Type 2 diabetes are obese, and obesity itself causes some degree of insulin resistance. It also is often associated with a strong genetic predisposition, more so than Type 1. The genetics however, are complex and not clearly defined. Gestational diabetes (GDM) is defined as any degree of glucose intolerance with onset or first recognition during pregnancy. A person that does not have diabetes and is pregnant may register an increment in his/her glucose levels. In some cases, the women who contract this type of diabetes develop overt type 2 diabetes after pregnancy. Approximately 7% of all pregnancies are complicated by GDM, resulting in more than 200,000 cases annually [16].

The presence of diabetes around the world is rapidly increasing. Poor eating habits and lack of exercise, factors which contribute to type 2 diabetes [17], have led to an increasingly overweight population. According to the International Diabetes Federation, there are 285 million cases of diabetes in the world as of 2010. This number is expected to increase to 438 million by 2030 [1]. Diabetic patients who do not control their levels of blood sugar are more vulnerable to other co-morbidities diseases. One potential risk that diabetics can face is that the excess of glucose can adhere to proteins in blood vessels, thus altering both their regular structure and normal function. In fact, diabetes can make vessels become thicker and stiffer, which can in turn reduce the blood flow. In diabetic nephropathy, the blood vessels in the kidney can also become leaky, allowing the proteins to be excreted with urine. In the end, some vessels collapse and put more pressure on the remaining ones. The increment of the load in these vessels can also damage them and in turn the kidney may fail, requiring kidney dialysis or kidney transplantation.

The nerves can also become damaged as a consequence of diabetes. Nerves allow us to sense temperature, pressure, texture, or pain. In most people with diabetes, the damage in the nerves (diabetic neuropathy) affects their feet and lower legs, causing numbness or tingling. People with diabetic neuropathy can acquire foot injuries such as open wounds but do not realize they have these injuries due to the loss of sensation from nerve damage. Such injuries can lead to serious infections and ulcerations which can progress quickly. The extreme consequence of an infection not treated in a diabetic is foot or leg amputation due to the gangrenous progression which can be life threatening. Finally, perhaps the damage to the eye and our visual perception of the world can have the most

effect on the quality of life among diabetics. Ocular disease present in the retina is termed retinopathy; hence, the lesions and tissue changes in the retina that comes as a consequence of diabetes is referred to as DR. In this chapter, we are going to focus in this disease as well as the currently available approaches used in the different steps for its detection, which could enable health systems to cover the high demand of people being screened to detect DR.

2.4 Diabetic Retinopathy

DR is a term applied to the effects of diabetes in the eye, or more specifically, the specialized neural tissue in the eye, the retina. DR is a highly specific vascular complication of both types 1 and 2 diabetes, with prevalence strongly related to the duration of diabetes. DR is the most frequent cause of new cases of blindness among adults aged 20-74 years. In addition to the duration of diabetes, other factors that increase the risk of, or are associated with, retinopathy include chronic hyperglycemia, nephropathy and hypertension [18]. This disease is usually asymptomatic in its early stages and, as a consequence, diabetics do not consider being examined on a regular basis. However, once DR has been detected in the retina, ocular examinations by an eye care specialist will require more frequent monitoring and visits. DR affects nearly half of the population with diabetes [1]. The global prevalence of diabetes has been continually increasing and current projections estimate that 438 million adults will be affected by 2030. With this estimate, a minimum of 2.4 million eyes would need to be evaluated for retinopathy every day [1].

2.4.1 Stages of DR

There are four stages which are described for the National Eye Institute (NEI) as indicated below:

a)   Mild Nonproliferative Retinopathy (NPDR): In this stage, a few microaneurysms, which are defined as small outpouchings in the walls of the tiny blood vessels (called capillaries) appear in the retina.

b)   Moderate Nonproliferative Retinopathy (NPDR): More lesions appear in this stage as more capillaries that nurture the retinal tissue become damaged, and the retina become more ischemic (lack of blood flow, and therefore lack of oxygen).

c)   Severe Nonproliferative Retinopathy (NPDR): At this level of DR, many blood vessels are affected. Blood vessel supply of oxygen to the retina is severely compromised due to accumulated vessel damage. When this occurs, certain areas of the retina start sending biochemical signals to the body that they need oxygen.

d)   Proliferative Retinopathy (PDR): In response to the need for oxygen, new vessels (neovascularization) begin to grow within the retina. These new vessels are an aborted attempt of the retina to regain its oxygenation need, but these vessels are compromised and fragile. These vessels "break" easily causing severe bleeding into the vitreous gel of the eye and consequent loss of vision. Also, these new vessels can attach themselves into the vitreous gel and cause traction on the retinal plane, causing retinal detachments.
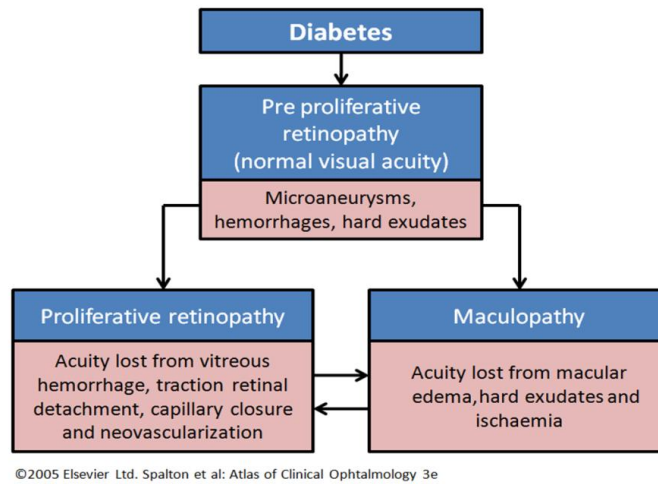
Figure 2.3 Development of eye disease produced by diabetes. (Image courtesy of [19])

Figure 2.4 Eye disease simulations. (a)Normal image, (b) Image seen by an advanced case of DR. (Image courtesy of [20])

As Fig. 2.3 shows, DR may advance in two ways [19]: proliferative retinopathy, which has been described before, and maculopathy, which can be frequently termed as diabetic macular edema, or, DME. As its name suggests, maculopathy is a disease that affects the

macula, which is the part of the retina that is most sensitive to light. This condition happens when fluid leaks into the macula, making it swell and causing blurred vision. This disease is very common in patients with proliferative retinopathy, affecting up to 50% of the cases. It can be noticed in Fig. 2.4 how the patients who are at an advanced stage of DR see the images blurry and incomplete, with black patches produced by pathologies such as hard exudates (HE) in the macula [20].

There are several factors that contribute to the development and progression of DR. The four most important factors are:

a)   Duration and type of diabetes: the most significant predictor is the duration of the disease. This varies depending on the type of diabetes. For type 1, DR rarely develops before 5 years from the onset of diabetes. Statistically, 8% of type 1 diabetes cases develop DR in the first 3 years of being diagnosed with diabetes; 60% of these cases develop DR in the first 10 years; and 80% of them after 15 years [21]. For type 2, 23% of the people develop DR after 11 to 13 years of diabetes diagnosis, while 60% of them develop it after 16 years or more [22].

b)   Blood glucose control: studies demonstrate that controlling the glucose helps in delaying the progression of DR in both types of diabetes [23], [24].

c)   Blood Pressure: high blood pressure in diabetics is characterized by the appearance of microaneurysms, hemorrhages, cotton wool spots, HE and optic nerve swelling, which is related to the level of systolic blood pressure.

d)   Renal disease: this disease can be associated with the presence of DR and vice versa [25].

Other factors that are associated with the increasing progression of DR are: smoking, anemia, pregnancy and serum lipids [25].

2.4.2 Description of the lesions in DR

There are many lesions that are associated with DR. In a typical screening population, it is expected that between 5%-25% of the patients suffer DR in its four stages [26].

Table 2.1 shows the frequency of pathologies associated to this disease and Fig. 2.5 show each of these pathologies.

a)   Microaneurysms (MAs): They are the first signs of DR. They appear in the retinal capillaries as small, round, red spots as it is shown in Fig. 2.5a. Their diameter measures from 10 to 100 μm [26]. They have clear and definitive edges, or boundaries. MAs are reversible if the blood glucose control is improved. Rupture of MAs and increased capillary permeability give rise to intraretinal hemorrhages. MAs can transiently appear and disappear over time.

b)   Dot/Blot hemorrhages (DBH): Leakage of blood in the inner nuclear layer. They appear dark red and also have a circular shape because they occur in the deeper, vertically-arrayed layers of the retina. Their edges can be more irregular and less definitive than MAs. Dot hemorrhages hardly exceed 200 μm [26].

c)   Cotton-wool spots (CWS): the lack of oxygen in the retina, called ischemia, causes damage in the nerve fiber layer of the retina. The result of this damage causes swelling in the nerve fiber layer axoplasm. In the fundus images, these lesions appear like puffy white patches as its name indicates.

d)   Hard exudates (HE): In DR, the vasculature becomes damaged and therefore more permeable, allowing lipids (fats) with water to pass through the vessels to the inner nuclear layer. After a time, the water returns but the lipids remain in the layer. These lipid deposits are called hard HE and they usually have a bright yellow color with irregular boundaries. They commonly form in ring-like shapes called circinate HE patches.
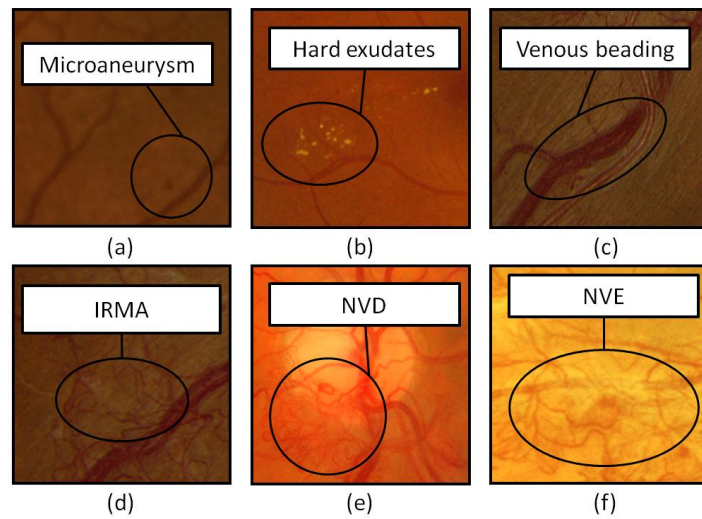
Figure 2.5 Pathologies present in DR. (a)Microaneurysms, (b)Hard Exudates, (c)Venous beading, (d)IRMA, (e)NVD, (f)NVE.
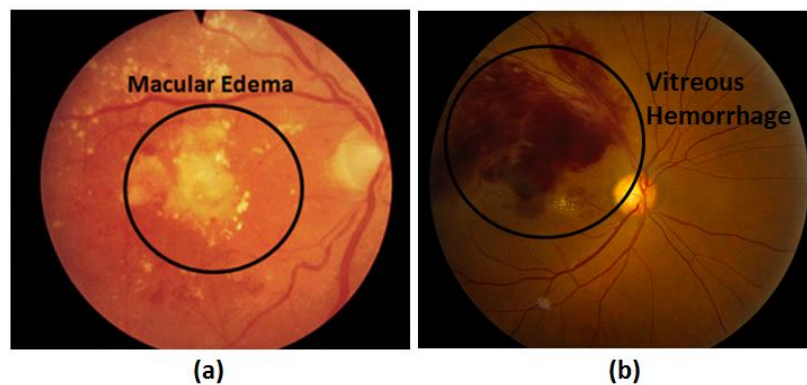
Figure 2.6 Advances pathologies. (a)Macular Edema with retinal thickening, (b)Vitreous Hemorrhage.

e)   Venous beading: This vascular abnormality (See Fig. 2.5c), which occurs in segments in the veins, is produced when there is capillary closure due to ischemia. Rather than smooth vessel walls, the veins appear highly irregular, much like beads strung on a necklace. Venous beading is a significant finding for the severe category of DR.

f)   Intra-retinal microvascular anomalies (IRMA): There are two theories about IRMA. One defines it as new vessels growing within the layers of the retina and the other one defines it as the dilated remnants of capillaries within a large area of capillary occlusion. Fluorescein angiography tends to favor the latter theory since IRMA is usually found within areas of capillary occlusion.

g)   Neovascularization: Large areas of ischemia (lack of oxygen) can be present in the retina. When the body detects that there is not enough oxygen provided to the retina, it produces a protein called Vascular Endothelial Growth factor (VEGF). After this is produced, new vessels that are going to compensate for the absence of oxygen appear in the retina. The problem is that these new vessels are weak and bleed easily, producing complications such as vitreous hemorrhages (see Fig. 2.6) and neovascular glaucoma. When neovascularization is present near to the optic disc (within 1 disc diameter centered in the optic disc), it is called NVD; otherwise, it is called NVE (elsewhere).

When DR is at a very advanced stage, retinal detachment could occur. If this is not treated immediately, permanent vision loss occurs.

Table 2.1 Diabetic Retinopathy pathologies

Type	Description (Figure)	Frequency*
Red Lesions	Microaneurysms (5a) + intra retinal hemorrhage	~3.50%
Bright Lesions	Hard Exudates (5b)+ CWS	~1.60%
Vascular beading	Changes in the vessel caliber (5c)	~1.00%
IRMA	Intraretinal microvascular abnormalities (5d)	~1.00%
NVD	New vessels growth in the optic disc (5e)	~0.10%
NVE	New vessels growth in the retina (5f)	<0.10%
Retinal thickening	Associate with macular edema, It is not visible with fundus images. (6a)	<1.00%
Vitreous Hemorrhage	It could be vitreous or subhyaloid hemorrhage (6b)	<0.10%

*Information retrieved from [28]

2.4.3 Treatment of DR

If the patient has DR between stages 1 to 3 but does not have macular edema (DME) no treatment is needed. The recommendations for the patients is to control their levels of blood sugar and other risk factors such as blood pressure and lipids, as this has been shown to slow the progression of DR. In the case the patient develops proliferative retinopathy (PDR), laser treatment will be recommended. In order to shrink the new vessels which appears in PDR, a treatment with laser is applied to the patient. This procedure is termed pan-retinal photocoagulation, or, PRP. In this procedure, the surgeon makes 1000 to 2000 laser burns with an argon laser in the retina avoiding the macula area. In theory, it is thought that this laser is actually causing damage to parts of the healthy peripheral retina (rather a sacrifice) to cause regression of these new fragile vessels. This treatment is most ideally applied in the cases where the new blood vessels have little bleeding or none, for best visualization of the retina. A vitrectomy is required

if the bleeding appears to be severe. In this surgical procedure, the vitreous gel which is mixed with the blood is extracted from the eye and refilled with a special saline solution.

In the case of retinal detachment, surgery is the only solution. The doctor could apply laser to try to fix the part of the retina that is torn or another procedure called cryopexy, which freezes the retina around the tear, leaving a delicate scar that helps secure the retina to the eye wall. Surgery is not always successful in reattaching the retina. Sight improvement after surgery depends in part on whether the central part of the retina (macula) was affected by the detachment before surgery, and if it was, for how long. Vision may take many months to improve after retinal detachment surgery. Some people do not improve their vision at all.

2.5 Diabetic Retinopathy Screening Systems

In this section we show all the processing steps that are commonly implemented in a DR screening system. While it is true that DR screening systems can be classified as top-down or bottom-up approaches, most of the published approaches are based on bottom-up approaches. In a bottom-up approach, the system is designed based on subsystems that perform a specific function; e.g., segmentation of HE for the detection of DR.

Fig 2.7 shows a block diagram which includes the steps involved in DR screening systems. Not all of these blocks are used in current systems, but it is necessary to take them into account to do a better assessment of DR.

In order to test the image processing methods for each step, different databases were made publicly available. A summary of these databases as well as some of the common metrics used to evaluate the performance can be found in the appendix.
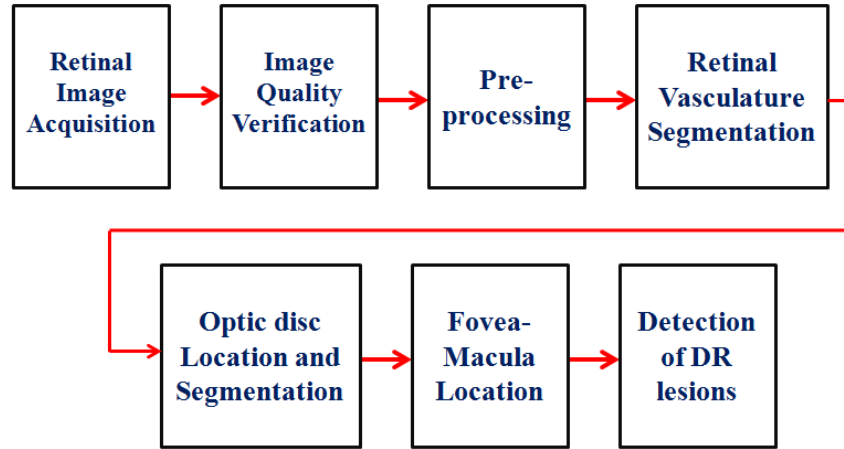
Figure 2.7 Block diagram of all the modules involved in a general DR screening system.

2.5.1 Retinal Image Acquisition

In the past, fundus images were captured on film. To analyze DR in film of 35mm, two 30 degrees field of view (FOV) images were required to capture lesions of retinal capillaries such as micronaeurysms and IRMA. Nowadays retinal images are acquired in digital format. They are usually acquired over a large FOV of 45, 50 or 60 degrees for the detection of DR. The images have a rectangular shape and the dimensions vary from hundreds to thousands of pixels [27]. The photographs of the retina are usually acquired in two ways: mydriatic (pupil dilation) or non-mydiatric.

Fig. 2.8 which shows the area of the retina that is usually captured by a camera for a specific degree setting, where R is the radius of the sphere of the eye and its length is 11mm [28]. The external angle, which is always provided by the camera, is greater than the internal angle depicted in Fig. 2.8, while the angle of the eye is considered to be twice as much as the internal angle[29]. Equations 1 and 2 are derived from Fig. 2.8. For

example, an image captured with 45 degrees corresponds to an area of 124.8mm^2 in the retina.
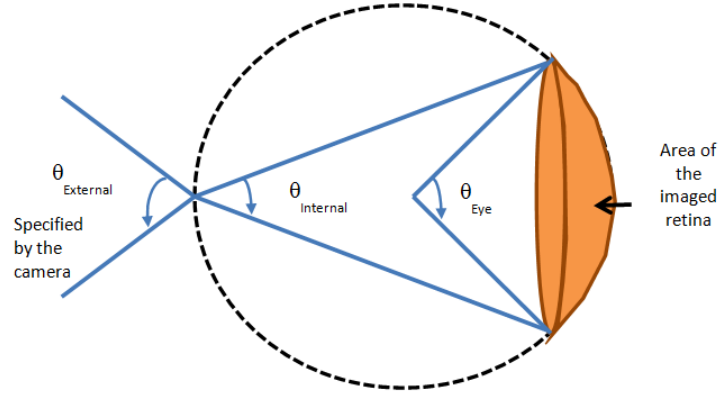
Figure 2.8 Relationship of the camera angle and the area of the imaged retina. (Image courtesy of [29])

$$A = 2\pi R^2 (1 - \cos(\frac{\theta_{Eye}}{2}))$$
(2.1)

$$\theta_{Eye} = 0.74 * 2\theta_{External}$$
(2.2)

Since the area of the retina is bigger than the area that is actually captured, many pictures of different fields of view of the retina are required. The gold standard consists of seven 30-degree fields using steoroscopic pairs [30]. Since 2 images are necessary in stereo (usually used to find the presence of glaucoma), 14 images are needed from each eye. It has been shown in [31] that reducing this to two or three 45-degree color fundus fields may be an effective tool in screening to detect DR and DME for prompt specialist referral. It also reduces costs, complexity and time.

Fig. 2.9 shows the 7-field standard for the right eye. The most common images obtained for screening purposes are from field 1, in which the optic disc is in the center of the image, and field 2, in which the macula is in the center of the image.
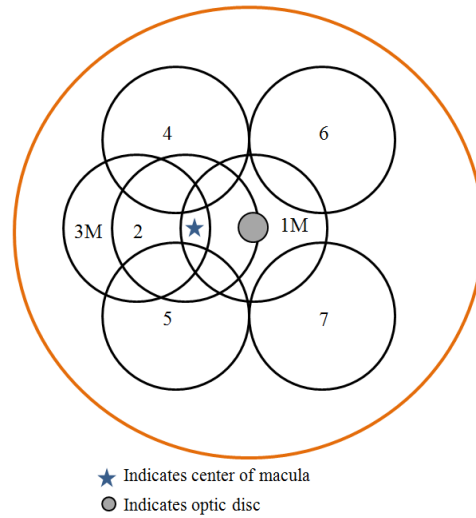
Figure 2.9 The seven standard 30-degree fields of view. (Image courtesy of [30])

In addition to retinal fundus images, other methods of image acquisition to analyze the retina are used such as fluorescein angiography and optical coherence tomography (OCT). Fluorescein angiography is a technique used to examine the circulation of blood in retinal vessels by using a dye tracing method. Patients are injected with sodium fluorescein, and then an image is captured by detecting the fluorescence emitted by the retina after having been illuminated with blue light at a wavelength of 490 nanometers. By using this method, microaneurysms, which appear as hyperfluorescent dots, can be clearly distinguished from dot-blot hemorrhages. Although, this review is focused in fundus images, first approaches in the detection of microaneurysms are based in the information of angiograms.

2.5.2 Image Quality Verification

It is important for images to be of good quality in order to provide a trustworthy diagnosis. In a typical screening environment, studies found that 10 to 20% of the images

were inadequate to provide accurate diagnosis [32],[33]. In a study performed by Scanlon et al. in 2003 [34], they found 20.8% of the images to be unreadable from a set of images collected from 1542 patients when the images were acquired in a non-mydriatic way, while 5.6% of the images acquired from 1549 patients were unreadable when the acquisition was mydriatic. Another study presented by Philip et al. in 2005 [35] reported that in a DR screening environment, 11.9% of the images from a total of 5575 patients were unreadable. In a multi-study report which used 2771 patients by Zimmer-Galler et al. [36], 11% of the images were unreadable. They found that poor patient's fixation, poor focus, media opacity and small pupil size are the major reasons for unreadable quality of the images. In general, there are two factors that affect the retinal image quality: biological inherent of the human retina and external factors. The external factors could be camera artifacts, low resolution, image compression, unfocused images and low contrast. Below, we list the biological and external factors.
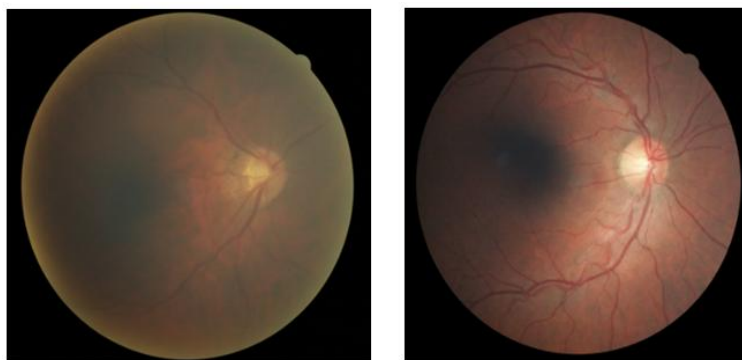
Figure 2.10 Examples of images with poor quality. In the left figure, the image is very blury. In the right side the macula is very dark; thus it very difficult to determine if there is a pathology in that area.

a) Biological Factors

These are some biological factors described in the literature that explain to a certain extent the variability in the retinal images [37].

- Lens coloration: As an individual ages, the lens becomes yellowish. This coloration changes the appearance of structures in the retina

- Lesion composition: lesions that appear in the retina have different compositions, which change their response to light

- Lesion density: the amount of light being reflected or transmitted depends on the density of lesions.

- Lesion position: since the retina is composed of different layers, lesions can develop in different positions. Their positions are another factor that changes their appearance in the fundus images.

- Pigmentation and Iris color: In the case of people with low pigmentation, their retinal images appear reddish (See Fig. 2.11(a)). Since lower pigmentation implies less reflectance, the choroidal vessels that are in a layer under the retina usually are more notorious in these subjects.

- Illumination: the spherical shape of the retina makes it difficult for all the areas to receive the same amount of light, creating artifacts. In addition to that, structures like vessels have a 3D shape, thus creating specular reflection highlights (See Fig. 2.12).

- Non-mydriatic images: retinal imaging sometimes requires the pupil to be dilated, especially in older people. The extent of this dilation varies across patients. If the pupil is not dilated enough, the iris of the eye could appear as a bright artifact at the boundary of the retinal image and the image will have poor quality.

- Others like age, race and eye color: The age of the patient affects the appearance of the retina and its coloration. In young people, specular reflection

(retinal sheen) within the retina may result in artifactual features and coloration as shown in Fig. 2.13. On the other hand, visual and macular pigment can be reduced with age [38].
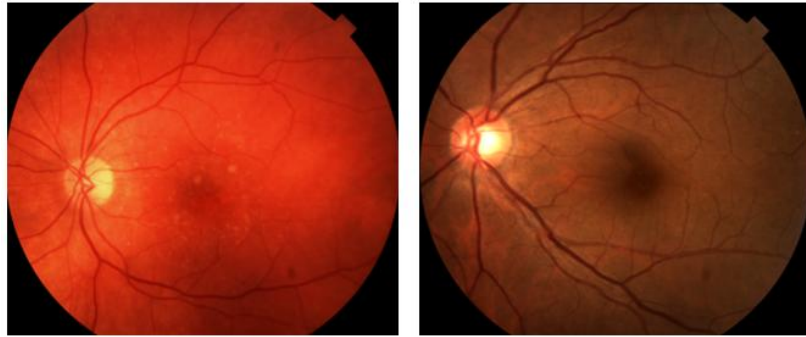
Figure 2.11 Retinas with different types of pigmentation: lower (left side), higher (right side).

Figure 2.12 Retinal images with bright artifacts.

Figure 2.13 Retina from a young patient.

b) External Factors

- Camera: The sensors of the camera do not adapt automatically to changes of illumination as well as the human vision system. The exposure must be controlled in order to obtain a good quality image. For example, the intensity of the camera flash needs to be adjusted in order to capture a good image.

- Loss of contrast: Unexpected movements of the patient eyes can make the image blurry and cause low contrast.

- Eye diseases: The healthy cornea is a transparent media, through which the light reflected from the retina passes without distortion. In a patient with cataracts, the cornea becomes opaque and causes distortion-when the light passes through. The image will appear hazy overall.

- Blurry images: movement of the patient or poor focus in the camera generates blurry images.

- Acquisition angle: the angle of the FOV could also affect the image. Images that are captured in a field different than the one centered in the macula are very difficult since the patient has to focus at an odd angle, which makes it hard for them to hold it still. Therefore more low quality images can be found in a field different from field 2.

- Compression: The images compressed to other formats like "JPEG" introduce blocking artifacts. A study performed by Conrath et al. [39] showed how the ratios of compression affect the grading of abnormalities such as microaneurysms, hemorrhages and IRMA. They also showed that the detection of pathologies is affected in both types of JPEG compression: JPEG and JPEG2000.

The quality of images, affected by all above factors, could introduce error in a screening process since an artifact could be detected as a lesion or it could mask a sight threatening condition. Many researchers have developed methods [40],[41],[42] to look for characteristics of the content of the image to determine its quality. One of the first published papers in this research area is the one developed by Lee and Wang in 1999 [40]. They measured the quality of a retinal image based on a reference histogram. Twenty images of good quality from a set of 360 were used to create a histogram model based on a Gaussian distribution as defined in Eq. 2.3, where A is the amplitude factor. A was assumed to be 1 for the analysis but the value could be calculated depending on the size of the image ($A = 6200$ for an image of 512x512 pixels). M is the desired mean value obtained from the ideal 20 images. The standard deviation σ is calculated from the retinal band I, which is the range where the total number of pixels is 99% of the total retinal pixels, divided by 6 according to the Gaussian distribution.

$$f(i) = A * \exp\left(-(i - M)^2 / 2\sigma^2\right), \text{where} \sigma = R/6 \tag{2.3}$$

To find the quality factor index of an image, first the correlation of its histogram, $H(i)$, and the template histogram $f(i)$ with $A=1$ is calculated. This coefficient, called C, is then divided by the coefficient achieved by the ideal case, which is C_{max}, giving as a result the quality factor Q, which is in the range [0 1]. If Q is near 1, then the image is supposed to have very high quality. Due to several factors, such as ethnicity, eye diseases, or the different cameras used to capture fundus images, retinal images histograms are usually dissimilar from each other. For this reason, their quality cannot be assessed based on a unique histogram template. Another approach developed by Lalonde in 2001 [41],

showed that bad quality images could also have the "ideal histogram" according to Lee's

model. They proposed two new measurements: the distribution of edge magnitudes in the

image and the local distribution of pixels to evaluate the image quality. In this case, the

dissimilarity was also measured using a reference histogram as proposed in [40]. The

contribution in this approach is that it also looks at the dissimilarity of the histograms in a

set of regions between the reference histogram and the target image. The target image

was segmented in regions, the histogram was extracted for each region and each

histogram was compared with the one obtained for the "ideal case" (See Eq. 4). Their

contribution was weighted according to the size of each region being considered ($Size_i$).

They are compared with the matching function W described in Eq. 5.

$$\text{d}_{\text{int}} = \sum_{i=1}^{Nregions} Size_i * W(H_i^{\text{Itarget}} - H_i^{\text{Imean}})$$

(2.4)

$$W(\text{h}_1, \text{h}_2) = \left[\frac{\mu_{\text{h}_1} - \mu_{\text{h}_2}}{\min(\mu_{\text{h}_1}, \mu_{\text{h}_2})} \right]$$

(2.5)

By using these two values for each image, Bayes decision theory was used to grade

the image as having good, fair or bad quality. They tested their approach in 40 images,

which were not enough to obtain conclusive results. In fact, their results show a great

variation between the 3 quality levels.

There is another group of methods that use vessel segmentation to determine image

quality. In this case, the information of the binary map of the segmented vessels of the

retina is used as basic information to determine the image quality level. The hypothesis

here is that a vessel segmentation method will not capture the vasculature correctly if the

images are blurry or have bad quality. Usher et al. were one of the first authors to use this

information in 2003 [43]. They measured the segmented vessel information in the whole

image. Given this information, they classified the images as having good or bad quality by setting a threshold value. They tested their approach in 1746 images, obtaining a sensitivity/specificity (sens/spec) of 84.3%/95%.
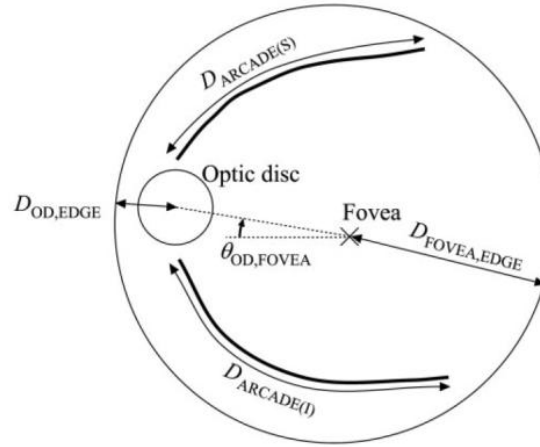
Figure 2.14 Features used to determine the field definition. (Image courtesy of [44])

A more complex algorithm which followed this approach was developed by Fleming et al. in 2006 [44]. In this paper, image quality assessment was evaluated based on two criteria. The first one was field definition, which used features of the retina such as the vessel arcades, the positions of the optic disc and the fovea to determine if the retinal image had the correct alignment, as shown in Fig. 2.14. An algorithm developed previously by Fleming's group segmented the vessels and detected the optic disc and the fovea [45], so the contribution in this approach for field definition was to find the arcades using semi-elliptical Hough transform.

The second criterion, image clarity, was used to determine if the image was adequate for the detection of lesions, especially the smallest ones such as microaneurysms. They used the assumption that the width of the vessels present in the macula area is similar to

the diameter of the MAs, so they were only focused on performing vessel segmentation in this macular region.

To measure image clarity, first, they evaluated if the detected fovea had high contrast by using the correlation coefficient between it and the "fovea model". If they found that the fovea had high contrast, they selected a square region of interest of size 3.5 disc diameters (DD) centered in the fovea to find if the vessel segmentation algorithm was able to capture the small vessels. To do that, they calculated the total length of the segmented vessels for the selected region. On the other hand, if they found that the detected fovea had poor contrast, they assumed it had not been correctly located and they would assign a new estimated position for the fovea following the following procedure. First, they selected a region of 4.5DD centered at their estimated location of the fovea and looked for a circle region of 2DD within this area that contained the minimum length of detected vessels. After they found this subset area, they fixed the new fovea location in the center of this circle. With this new fovea location, they selected the region of 3.5DD and calculated the vessels' overall length. An image that had adequate image clarity had high vessels' length. The threshold value was selected after a training process. They used 1039 images of 45 degrees field 2 to test their approach. They obtained sens/spec of 95.3%/96.4% for the field definition problem and sens/spec of 99.1%/89.4% for image clarity.

Although the results presented by Fleming show very high accuracy rates, this method requires prior segmentation of vessels and detection of the optic disc and fovea. In addition, this method fixed its analysis to images of field2, in which the macula is placed

at the center of the image, but other fields of view where the macula is placed somewhere else in the image, such as field 1 images, were not considered.

In contrast to these methods, which were based on a reference case or only on vessel segmentation, there were other methods that were based on supervised classification. The information of each image (features) along with its quality level was provided to the algorithm in order to obtain a model that could be used to predict the quality level of a new set of images. Among these methods, we can find the approach developed by Niemeijer et al. [46] in 2006. In this approach a multiscale filterbank based on Gaussian derivatives was applied to each image so that a vector containing different filter responses were obtained for each pixel. Then, image structure clustering (ISC) was used where a k-means clustering approach was applied to group the pixels in 5 clusters. After separating those pixels into 5 clusters, they counted the number of pixels that belonged to each cluster. These 5 count values plus the 5-bin histograms of each color plane in the RGB color space represented a feature vector for the classification algorithm. In order to obtain the best set of features, sequential forward floating selection (SFFS) was used. Two algorithms for classification were tested: support vector machines (SVM) with different kernels and the k-nearest neighbors classifier. To test their algorithms, 2000 images were used and divided evenly for training and testing sets. From their results, the SVM classifier performed better than the other one, obtaining an AUC of 0.9968.

In 2008, Davis et al. [42] also used a classification method to assess the image quality. They used the information of the histograms such as mean, intensity, variance, skewness, kurtosis, median, 1st quartile, 3rd quartile, and information of entropy, spatial frequency and 13 haralick features for each color plane in the RGB and CieLab space. A total of

102 features represented an image. Two experiments were performed with different databases. First, they used 600 images form MESSSIDOR [47] database. Since these images have good quality, 400 images were degraded artificially. A supervised regression classification method called partial least squares (PLS) with jack-knife as a validation method ('leave-one-out') was used to detect two quality levels: acceptable or unacceptable. An AUC=0.998 was obtained in identifying these levels. Then, 398 images were selected from the University of Iowa database. From this set, 200 images were selected randomly containing acceptable or unacceptable quality images; they obtained an average AUC of 0.993.

Giancardo et al. [48] combines a vessel segmentation approach and a classification method. They divided the retinal image in regions and calculated the vessel density for 18 regions within an image as the first set of their features. In addition to that, they calculated the 5-bin histogram as done by Niemeijer et al. [46] as the remaining features. By using a SVM classifier, an average AUC of 0.93 for the classification of good quality images was obtained from a set of 84 macula centered images.

In 2010 [49], Paulus et al., incorporated the ISC used by Niemeijer et al. [46] but performed the clustering using the intensity values as the input of the classifier. They also used the haralick features and a sharpness metric to measure the strong edges. These three types of features were used to train a SVM. A total of 301 images of field 1 (optic disc at the center of the image) of 22.5 degrees were used to test their approach, obtaining an AUC of 0.97.

A recently published paper takes into account images from field 1 and field 2. In the approach presented by Yu et al. [50], global histogram features and Haralick textural

features were used just like the methods described before. Vessel density features as [48] were added to the system using the output of the segmentation vasculature with an algorithm previously developed by the same group described in [51]. In addition, local sharpness in the image was measured using cumulative probability of blur detection (CPBD) described in [52]. This method assumes that the blurriness around an edge is more or less noticeable depending on the local contrast around that edge; in this way the degree of sharpness is more similar to human perception. These features were the input to a partial least squares (PLS) classifier. The algorithm was tested in fundus images from 412 patients (1884 images) with 45 degree FOV. The proposed approach obtained sens/spec of 99%/80%.

2.5.3 Pre-processing methods for fundus images

Although the aforementioned approaches could recognize the images with acceptable quality to be processed by a DR screening algorithm, there were some techniques of pre-processing that can be applied in order to improve the accuracy in the detection of lesions. This pre-processing step can be developed in two ways. The first one tries to deal with the variations within the same image, which is called intra-image correction; the second one normalizes the differences between images and is called inter-image normalization. To address this inter- and intra-image variability in the retinal images, the pre-processing block has been divided in 3 stages: Correction of non-uniform illumination, color normalization and contrast enhancement.

2.5.3.1 Methods for non-uniform illumination correction

Images that are generated from a physical process, such as retinal images, have their intensity values proportional to the energy radiated by the source. As a consequence, the images can be characterized by two components: the amount of illumination incident on the scene being viewed, called illumination (*i(x,y)*); and the amount of illumination reflected by the objects in the scene, called reflectance (*r(x,y)*).

$$f(x,y) = i(x,y)r(x,y), where\ 0 < i(x,y) < \infty\ and\ 0 < r(x,y) < 1 \qquad (2.6)$$

While the illumination component of a retinal image changes gradually, the reflectance component changes sharply, especially at the edges of the image [53]. This non-uniform illumination causes artifacts such as shading artifacts and vignetting [54]. Vignetting occurs when the brightness or the saturation of the image decreases at the periphery compared to the center. Many times these non-uniformities are not visible to the human observer; however, they affect the statistical information that is used to generate input features in classification algorithms. One of the most common approaches to correct the non-uniform illumination is illumination equalization. For this method each pixel is assigned a new value by using a reference value for the average intensity (*m*) and the average value of the pixels surrounding the pixel to be equalized (*A(x,y)*).

$$I_{eq}(x,y) = I(x,y) + m - A(x,y) \qquad (2.7)$$

The value for *m* is usually 128 for an 8-bit image. To compute the value of A(x,y), an NxN window was applied to each pixel so the local average intensity can be calculated. In [55] a window of 40x40 was applied to images of the STARE database [56]. As a final step, the image was smoothed to avoid any kind of artifact. A variation of this method was presented in [57], where the image in RGB color space was transformed to YUV

color space and the Y channel was equalized. After doing so, the image in the Y'UV

space was transformed again to RGB.

In [58], an adjustment was performed for the correction of non-uniform illumination.

This implementation has to deal with the different levels of brightness present in the

image. By applying Eq. 8, the pixels are adjusted with two factors:α and β. Those values

were set empirically, where *inmax* is the upper limit intensity value of the input image

desired in the transform function.

$$y = \beta * x^{\alpha}, \qquad where\ \beta = inmax^{1-\alpha}\ and\ 0 \le inmax \le 255 \qquad (2.8)$$

The problem with this method is that it is necessary to tune the parameters and that it

is mainly focused to detect bright lesions since the correction of illumination was only

applied in a range of the histogram. Other approaches like [59] use a method called shade

correction. This method was used to remove all the non-uniformities in the background.

The background was estimated creating an over-smoothed version of the image using a

mean or median filter. The size of the window was usually set to the width of the largest

structure in the retina. Finally the original image was divided or subtracted by the new

image [60], [61], [62], [63], [64].

Homomorphic filtering is another technique that is commonly applied to correct the

illumination of the images as well as to increase their contrast. Eq. 9 illustrates that

illumination and reflectance frequency terms are not separable if the Fourier transform is

directly applied to Eq. 6. Nonetheless, if the logarithm is applied to both sides of Eq. 6.,

we can separate both terms linearly as it is shown in Eqs. 10 and 11. Since the

illumination is represented in low frequencies and the reflectance is found in the high

frequencies, a high pass filter is applied to attenuate the illumination, making it more

even [65].

$$\Im\{f(x,y)\} \neq \Im\{i(x,y)\}\Im\{r(x,y)\} \tag{2.9}$$

$$z(x,y)= \ln\big(f(x,y)\big) = \ln\big(i(x,y)\big)+\ln\big(r(x,y)\big) \tag{2.10}$$

Then, $\quad \Im\{z(x,y)\}=\Im\{\ln\big(f(x,y)\big)\}=\Im\{\ln\big(i(x,y)\big)\}+\Im\{\ln\big(r(x,y)\big)\}$ (2.11)

In [66], a method called Iterative Robust Homomorphic surface Fitting (IRHSF) is proposed. This method estimates the reflectance of the retinal image by combining homomorphic filtering, surface fitting [67], and the information of the retina such as vasculature, optic disc and pathologies. The authors used a low-order parametric surface to model the illumination of the fundus image. The limitation of this algorithm is that when a big lesion appears in the retina such as a huge hemorrhage, a "halo" light effect around the lesion appears. To solve this issue, the lesions are assumed to have intensity values in either low or high percentiles. Due to this fact, an iterative adjustment was performed so the algorithm can only work with the pixels without lesions (setting the pixels with lesions to 0). This algorithm was applied to measure longitudinal changes in retinal images but it can be applied to lesions detection too. In their publication, the model used a 4$^{\text{th}}$ order polynomial with 15 parameters as shown below.

$$\vec{F_L} = \begin{pmatrix} F_L(0,0) \\ F_L(0,1) \\ \vdots \\ F_L(x_i,y_i) \\ \vdots \\ F_L(N,M) \end{pmatrix} = \begin{pmatrix} 0 & 0 & 0 & \dots & 0 & 1 \\ 0 & 0 & 0 & & 1 & 1 \\ \vdots & & & & & \vdots \\ x_i{}^4 & x_i{}^4 y_i & \dots & y_i & 1 \\ \vdots & & \dots & & \vdots \\ N^4 & N^3 M & & M & 1 \end{pmatrix} \begin{pmatrix} p_1 \\ p_2 \\ \vdots \\ p_{15} \end{pmatrix} \tag{2.12}$$
$$= S\vec{P}$$

$$\vec{P} = (S^T W S)^{-1}(S^T W)\vec{F_L} \tag{2.13}$$

where W is a weight matrix in which nonzero elements correspond to pixels that are inside the region of interest. Then the illumination and reflectance are estimated with the following equations.

$$I(x, y) = \exp\left(\boldsymbol{S}\vec{P}\right) \tag{2.14}$$

$$R(x, y) = \exp\left(F_L(x, y) - \boldsymbol{S}\vec{P}\right) \tag{2.15}$$

In order to correct the non-uniform illumination, Foracchia et al[68] used a model in which the background luminosity and contrast variability were estimated. The model is described in Eq. 16, where I is the observed image, I° is the original image and C, L are the contrast and luminosity drift factors respectively.

$$I(x, y) = f(I^{\circ}(x, y)) = C(x, y)I^{\circ}(x, y) + L(x, y) \tag{2.16}$$

To calculate the drift factors, the mean and the standard deviation were calculated in a window of N background pixels.

2.5.3.2 Methods for color normalization

This step is very important in the case of lesion detection using pixel intensity value information. The color of each of the lesions can help to discriminate them. That is the reason why many approaches have been developed to detect abnormalities in the retina using color information [69], [70] , [71]. Different color channels provide different kinds of information. For example, some authors like Shin et al. [72] and Soares et al. [73] used the green channel since it has more contrast in the RGB space. This color plane is considered the most informative one and less subject to non-uniform illumination [74]. Other approaches used the red channel color plane in the detection and segmentation of the optic disc since the vessels appear very smooth and do not interfere with the segmentation [75], [76]. Finally, the blue channel contains little to non-useful information and for that reason it is almost not considered in monochromatic implementations. Fig. 2.15 shows the retinal images in the different color spaces.

Even for color or grayscale implementations, the normalization of the range of intensity pixel values is very useful in order to extract features which are consistent across images. For example, HE are bright lesions which are the most distinguishable lesions in DR. By using an image as a reference, an algorithm based in thresholding can be tuned to detect them. The problem with this kind of methods is the inter-image variability, which makes the model created with a particular image potentially invalid for a new image if it has low contrast. In such a case, it is possible for HE not to be above the tuned threshold; therefore, they would be confused with retinal background [26], [58]. The most common methods of color normalization are described in this subsection. These methods were tested in different databases and their contributions to the detection of structures in the retina have been analyzed in [37].

A. Color Transformation

This technique deals with the processing of the components of a color image. Some of the automated screening systems prefer to use color spaces that are different from RGB. Most of the common color spaces are shown in Fig. 2.15. By weighting each channel and combining them with different mathematical operations, some transformations are generated.
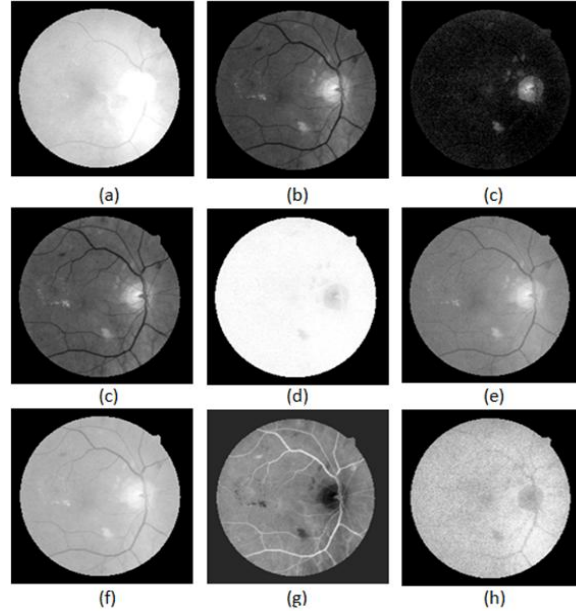
Figure 2.15 Most Common color space used in eye screening algorithms. (a) Red channel, (b) Green channel, (c)Blue channel, (d)Hue, (e)Saturation, (f)Intensity, (g)Component L from CieLab color space, (h)Component a from CieLab color space, (i)Component b from CieLab.

The most commonly used normalization approach is greyworld. This normalization procedure models changes in illumination spectrum by means of three constant multiplicative factors, which are applied to red, green, and blue channels. This normalization divides each color component by its mean value within the image. The new values for each pixel (r,g,b) in the image are defined by:

$$r^{new} = \frac{r}{R_{avg}}, \qquad g^{new} = \frac{g}{G_{avg}}, \qquad b^{new} = \frac{b}{B_{avg}} \qquad (2.17)$$

where R_{avg}, G_{avg} and B_{avg} are the mean values of the R, G, and B color planes, respectively. Fig 2.16 shows the output of the color image after the normalization. As it can be appreciated in Fig. 2.16, the normalization works for one case but it does not work for the other one. In the case of Fig. 2.16(b), it can be noticed that the yellow color around the main arcades is more uniform. The problem with this method is that when the blue channel is also normalized, the overall contribution is not good. It could be inferred

from this observation that the blue channel by itself does not provide informative retinal features. In fact, the histogram equalization subsection will provide further support to this claim.
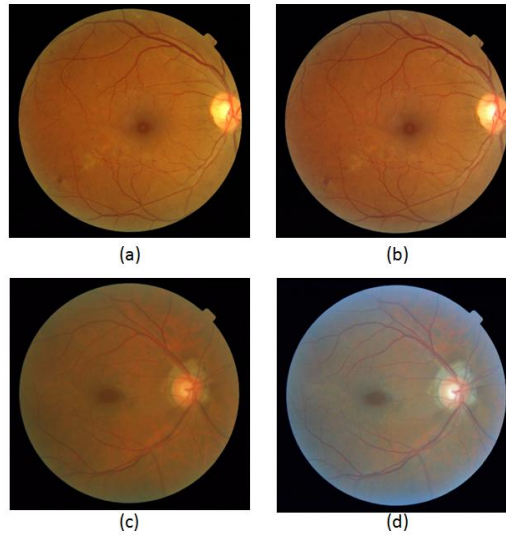
Figure 2.16 Greyworld normalization. (a) and (c) Original images, (b) and (d) Greyworld normalization.

B. Histogram equalization

It has been shown that histogram equalization performed individually in red, green and blue channels achieves a better performance than the greyworld approach [77]. This method is based in maintaining the pixel rank order for each RGB plane under different illuminants. For example, if under one illuminant the red values of two pixels are r_1 and r_2, where $r_1 < r_2$, then under another illuminant, although the magnitudes of r_1 and r_2 may change, r_1 should still be less than r_2 (there are, however, some conditions where this will not be true). Histogram equalization is a monotonically increasing non-linear transform (mapping) which maintains pixel rank. One issue of the aforementioned method is that it magnifies the intensity of the blue channel, when in fact the retina reflects a small amount of blue light [78]. This can be appreciated in Figure 2.17, where the images appear with a

blue tone when the contrast is low. Although the red lesions are enhanced by the method, it can also be seen that the optic disc and its surroundings are affected. The problem with this method is that it depends on the global statistics of an image, when equalization is sometimes needed only on a part of the image so that it does not affect important landmarks of the retina such as the optic disc or the fovea.

(a)   (b)
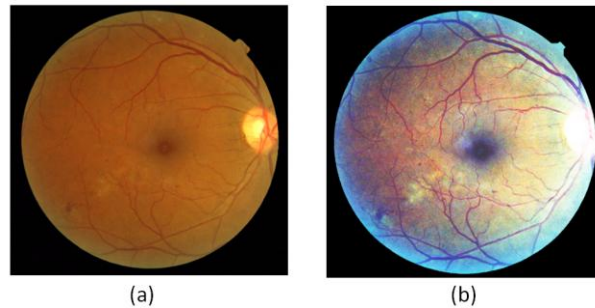
Figure 2.17 Histogram Equalization. (a) Original images, (b) Result of histogram equalization.

C. Histogram specification

This method is an alternative to histogram equalization. It works with histograms but in this case it transforms the red, green, and blue histograms to match the shapes of three specific histograms [79]. This approach has two main advantages over equalization. First, the images produced with this method appear to be visually more real than the ones generated with histogram equalization. Second, this method makes it possible not to overestimate the contribution of the blue channel. To apply this method, an image graded by an expert as having good contrast is taken as a reference.

Goatman et al. [37] compared the performance of the three aforementioned normalization methods by analyzing the chromaticity coordinates of 4 types of lesions. In this way, he proved that by using histogram specification, the information of the lesions (the one embedded in the red and green channels) could be better discriminated.

Approaches that used this technique are usually found in the detection of hard HE [72], [80]. However the limitation of this method is the choice of the reference image since the histograms of images from normal and abnormal patients could be very dissimilar. In Fig. 2.18, which reports results of the histogram specification method, it can be noticed that the color is uniform in Fig. 2.18b and Fig. 2.18c, but when the image has more lesions or presents saturation such as Fig. 2.18d, the processed image is distorted.
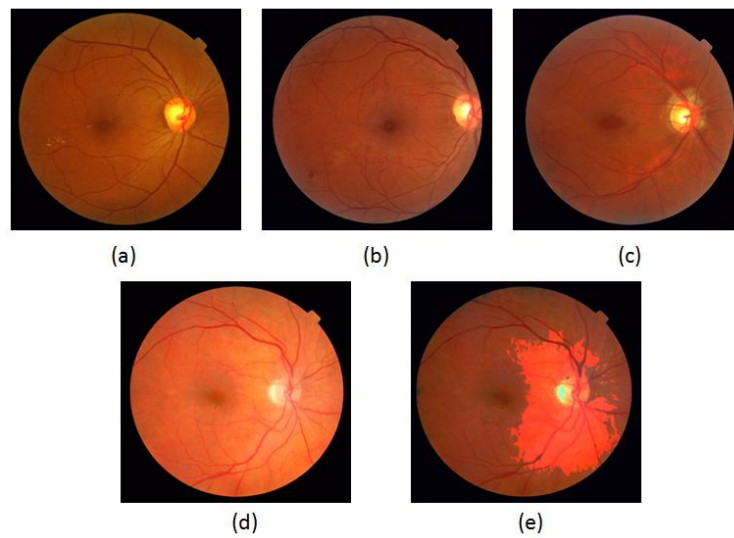
Figure 2.18 Histogram Specification. (a) Reference Image, (b) and (c) Results of histogram specification for images in Fig. 16, (d) Original Image, (e) Result of histogram specification using (a) for image in (d).

An alternative was proposed by Cree et al. [81] in which a shade correction method to deal with the intra-image variability and a histogram normalization to deal with the inter-image variability are combined. In this normalization scheme, the histogram was adjusted to have a specific mean and standard deviation; hence, it retains the overall shape of the histogram and shifts the hue plane to be consistent between images.

2.5.3.3 Methods for Contrast Enhancement

These techniques are developed in order to make the structures in the image more distinguishable than the background or other structures. For this particular topic, many approaches have developed or used techniques to increase the contrast between the lesions or vasculature and the retinal background. There is not a quantitative measurement to evaluate the contrast enhancement; only visual inspection or improvements in the results based on a specific algorithm are the metrics used. Given the shape of the retina, conventional methods such as contrast stretching or others based on global histogram information are not useful since the retinal image was characterized by its higher contrast in the center and lower contrast in the edges of the image [78], [82], [83]. For that reason, local enhancement methods are preferred. The methods found in the literature are usually followed by a noise reduction technique since the noise was also enhanced. In some publications, only noise reduction without contrast enhancement was applied to the images. Chaudhuri et al. in [84] smoothed an image of 512x480 pixels with an average filter of window size 5x5 to reduce the effect of spurious noise.

A technique used to assess the limitations of global enhancement, which is called adaptive local contrast enhancement was proposed by Sinthanayothin et al. in [85] and used by Park et al. in [86]. In this technique, contrast enhancement was applied to local areas depending on their mean and variance. If a window W of size MxM is centered at pixel(x,y), then the output of this pixel is defined by:

$$g(x,y) = 255 * \left[\frac{\Psi_w(f) - \Psi_w(f_{min})}{\Psi_w(f_{max}) - \Psi_w(f_{min})} \right] \qquad (2.18)$$

where f_{min} and f_{max} are the minimum and the maximum intensities in the whole image. The sigmoidal function is defined by the following equation:

$$\Psi_w(f) = \left[1 + exp\left(\frac{<f>_w - f(x,y)}{\sigma_w}\right)\right]^{-1} \qquad (2.19)$$

and $<f>_w$ and σ_w are the mean and the variance in the window W. Sinthanayotin et al. [85] also recommend the application of a 2-D Gaussian or median filter to the image before the enhancement in order to minimize the enhancement of noise. This pre-processing was applied to the intensity plane of the HSI color space to locate the optic disc, fovea and blood vessels in [83], and to detect bright lesions in [71], [87]. This transformation works very well for regions with small variance where the contrast was highly increased; otherwise the contrast was minimally enhanced. Another technique called adaptive histogram equalization (AHE) was applied in [88], [89] to enhance the contrast in the images. This method achieved good results especially for detecting vessels in areas with low contrast. The following equation shows the formula used to perform the equalization of an image where *M = 255*, *h* is the length of the square window, *R(p)* denotes the set of neighbors of the pixel *p* to be equalized in the window, and *s(d)=1* if *d>0*; otherwise *s(d)=0.* In both applications, the values of *h* and *r* are set to 81 and 8 for images of 605x700 pixels and 768x584 pixels.

$$I_{AHE}(p) = \left(\sum_{p' \in R(p)} \frac{s(I(p) - I(p'))}{h^2}\right)^r * M \qquad (2.20)$$

In [70], the contrast of the images was improved by using a contrast-limited adaptive histogram equalization (CLAHE) [90] to detect HE. This method, which is an extended version of AHE, allows adjustment of the amount of enhancement required [79]. By using this method, a reduction of the amplification of the noise can be obtained by selecting the clipping level of the histogram.

An alternative approach to increase the images contrast was proposed by Rapantzikos et al. in [74] to detect drusen. This method, which is called multilevel histogram equalization (MLE), is based on applying histogram equalization sequentially to smaller non-overlapping neighborhoods obtaining enhancement in the drusen without being affected for the small brightness variations.

Other pre-processing methods are more specific, being designed based on its application. For example, to detect lesions in retinal images, Spencer et al. [60], Frame et al. [91], and Niemeijer et al. [92] removed the slow gradients in the background of the green channel of each image, yielding a shade corrected image to detect red lesions. On the other hand, for detecting the optic disc, Lu [93] generated a new intensity image by combining the intensity values of the red (75%) and green (25%) channels. By doing so, he reduced the presence of vessels in the optic disc, maintaining the image variation across the optic disc. Other approaches are focused on the development of pre-processing steps for the detection and subsequent removal of normal anatomical "background" structures in the image. Fleming et al. [94] applied a 3x3 pixel median filter to reduce this variation. They convolved the retinal image with a Gaussian filter and then normalized the image for the detection of HE.

2.5.4 Retinal Vasculature Segmentation

This is a research area that presents a large variety of algorithms to segment the retinal vasculature. Among the purposes for the development of algorithms to segment retinal vasculature, the most important are: to reduce the number of false positive red lesions in DR screening systems, to calculate the width of the vessels in order to detect

cardiovascular diseases (CVD) [95], and to measure geometrical attributes at vessel bifurcations like angles to find features that capture other diseases. For instance, in [96], they show that in patients with hypertension, the angle between the 2 offspring arterioles was reduced. For that reason, accurate segmentation of the retinal blood vessels is very important not only to identify parts of the retina such as the optic disc or the fovea as shown in [97], but also to assist in the detection of other diseases such as high blood pressure, stroke, etc. In Barker et al. [98], they concluded that hypertensive retinopathy signs like focal retina arteriolar narrowing, arterio-venous nicking and other common signs of DR like microaneurysms and HE are considered to be markers of risk of stroke. A more complete review study of the association to incident stroke was presented by Doubal et al. [99]. In this comparison, ratios of abnormalities in the vasculature are presented and compared with previous studies. Despite the large variation in the studies, it was demonstrated that retinal microvascular abnormalities and stroke are associated. In addition to that, Patton et al. in [100] state that the retinal microvascular changes reflect cerebral microvascular changes in aging as well as vascular dementia and stroke. This is because the brain and the retina have similar vascular regulatory processes [101], [102]. Therefore, retinal image analysis can be an alternative to other techniques like transcranial doppler ultrasound, positron emission tomography (PET), single-photon tomography (SPECT) and functional neuroimaging using magnetic resonance imaging (FMRI) to detect those diseases. In addition to the already mentioned diseases, the Blue Mountain Eye study indicates that large retinal venular caliber may even predict the incidence of obesity over a 5-year period, suggesting the existence of altered microvascular function in the pathogenesis of obesity.

In the case of DR screening algorithms, some of the current approaches segment the vasculature to remove them from the retina in order to calculate more accurate features in the detection of lesions. As it has been described in the image quality section, segmented vessels are also used as features to determine the quality level of the image. Another common application of vasculature segmentation is to register retinal images using the vasculature map to spatially align them [103]. More recently, vessel segmentation was used to detect neovascularization in the optic disc [104]. For all these reasons, the following paragraphs describe and compare some of the approaches that have been developed in the literature. Before we explain the developed approaches for vessel segmentation, a summarized list of the characteristics of the retinal vasculature is presented.

- It is composed by arteries and veins.

- The central retinal artery bifurcates at or on the optic disc into ramifications that supply blood to the whole retina.

- The vasculature presents lower reflectance, which is the reason why it appears dark in the fundus image.

- Biological factors in the vessels such as variations in their wall thickness or their refraction index do not affect the appearance of their width in the retinal images.

- The width of the vessels varies from 36-180 μm

- The width of the vessels is reduced from their origin (optic disc) to the end of their trajectories.

The current approaches can be separated in 4 groups: window-based, morphology, classifier-based and tracking-based.

2.5.4.1 Window based

As its name indicates, these methods are developed using approaches based on windows such as edge detection and matched filters, which are the most common in this area. One of the earliest approaches was the one developed by Chaudhuri et al. [84]. This approach was based on the assumption that the cross section of a vessel approximates to a Gaussian distribution, which was described in Eq. 21. In it, k is the measurement of the reflectance, d is the perpendicular distance between the point *(x,y)* and the straight line passing through the center of the blood vessel in a direction along its length, and A is the local intensity of the background. In addition to this assumption, the vessels are considered to have small curvatures that can be represented by piece-wise linear segments. Therefore, a 2-D matched filter in 12 different positions, assuming 15 degrees of separation between them, was generated as a template. Then, the 12 kernels were convolved with the image and the highest response from the filter was selected as an indicative that the pixels belong to a vessel. After that a threshold was applied to obtain the vessel map.

$$f(x, y) = A\{1 - k\exp(\frac{-d^2}{2\sigma^2})\} \tag{2.21}$$

Zhou et al. [105] also proved that the Gaussian curve is the most adequate function to model the cross sectional vessel in the retina. They estimated the vessel width using the Gaussian model reporting promising results. There are two main problems with this method. First, it is computational expensive, and second, it only works well in normal

retinas. When the retina has lesions such as DR, the method fails. In 2000, Hoover et al. [106] used this method as a basis in their approach but they incorporated the use of global and local features to segment the vessel network. In this method the threshold for the output of the match filter response (MFR) was selected with a method called threshold probing. This method used a number of region-based properties in different regions in the image. Contrary to other techniques, this method allows to examine each pixel in multiple regions before assigning it a class.
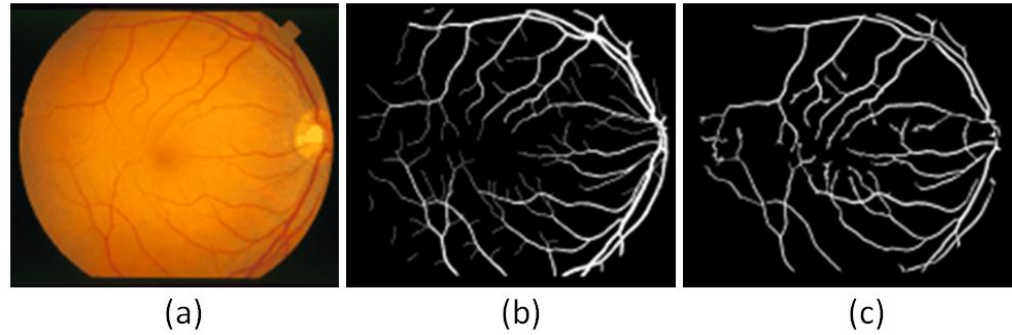
Figure 2.19 Vessel segmentation results of Hoover et al. [106]. (a) Original image, (b)Ground truth of the vasculature, (c) Results of the segmentation. (Image courtesy of [106])

Gang et al. [107] also used the matched filter methodology. They said that the width control parameter in the Gaussian curve is linearly related to the vessel width. Eq. 22 shows the Gaussian curve they used for fitting, where w is the parameter that controls the window.

$$g(x) = A * e^{\frac{-(x-z)^2}{2w^2}}$$
(2.22)

In order to measure the width of the vessels, the amplitude-modified second-order Gaussian filter is applied. The evaluation of its performance shows that the algorithm was

not only suitable for measuring the vessels, but also for improving the common matched filter detection algorithm.

In another approach, Lowell et al. [108] proposed the use of a non-linear order-statistics based "tramline" filter instead of using the Gaussian matched filter. They stated that this filter was more robust with bright object distraction. This filter was the generalized grey-level morphological top-hat filter with two specialized structuring elements: a line that follows the same orientation as the blood vessels and 2 tramlines that have the same direction of the blood vessels but are positioned in the sides of the vessel. The response of the filter was the difference between the minimum intensity and the maximum intensity of the inner line and the outer tramline structuring elements, respectively. As Chaudhuri et al. [84], 12 directions were used; however, since the maximum and minimum values of the outputs of the filter can introduce some noise, the third largest and the third smallest values were selected. They also stated that the algorithm fails at major vessel branch points, crossing points or where there are parallel vessels in close proximity.

2.5.4.2 Morphology

Other approaches have been implemented using morphology. Morphology is a technique that is used to extract image components such as structures that are useful in the interpretation and the description of an image. Since the vessel structure in the retina is well-known by its shape and piecewise linear connected components, morphology is ideal for the segmentation of vessels. In addition, the processing time for this method was very small and it was also robust against noise. One of the best known papers in this area

is the one developed by Zana and Klein in 2001 [109]. They modeled the vessel-like pattern as: being uniform in color, having a cross section shape as a Gaussian curve, being connected like a tree, and having a certain width with a minimum distance between them. They used morphology to recognize the linear parts in different orientations and also to remove the noise. To remove patterns that were not desired in the segmentation, a Gaussian filter followed by a Laplacian operator and a designed alternative filter were used. The algorithm was tested in 200 angiograms and qualitative results were presented.

Miri et al. [110] presents an algorithm for detecting vessels using the curvelet transform [111] to enhance the ridges. Then, the enhanced images were processed with morphological operators using multistructure elements to obtain a coarse segmentation of the vasculature. Then, morphological operators by reconstruction were used to obtain the final segmentation.

2.5.4.3 Classifier-based

In this kind of approaches, features are extracted from the images and a classification algorithm was trained to detect if a pixel belongs to a vessel using that information. The most common classifier method is Artificial Neural Networks [83], [112],[113]. The limitation of supervised classification methods is the necessity of ground truth. For that reason, some databases were made publicly available in order to obtain the ground truth and to standardize the evaluation of the performance of different algorithms: STARE [56], DRIVE [114], REVIEW [115].

Among the approaches developed in this area, Staal et al. [116] used the information of images ridges which concur with the vessel centerlines. First, they calculated the

ridges from the image. Next, they formed primitives for the vessels by grouping the ridge pixels that belonged to the same ridge using a simple region growing algorithm. In order to classify a pixel as a vessel or not, a set of features were extracted and selected using sequential forward selection method. Finally, the k-nearest neighbors (k-NN) classifier was applied to the data. A more recent approach by Soares et al. [73] extracts features using the output of Gabor filters. In this approach they used the inverse of the green channel so the vessels can appear brighter than the background. The advantage of using filters is that they can be tuned in order to reduce noise and enhance the vessels. The filters have different scales and different orientations (10 degrees of separation) and the feature space was selected to be the highest value from all the outputs at each pixel [117]. In this case, a Bayesian classifier with Gaussian mixtures as probability density functions was used.

Support Vector Machines (SVM) was used as a classifier in Ricci et al. [118] approach. In their algorithm, linear operators were used to extract the features. These operators follow the same principle as matched filters and directional filters. In this paper, just as the previous method did, they inverted the green channel to put the vessels brighter and no contrast enhancement was applied to avoid loss of information of the vessels. Niemeijer et al. [119] defines a pixel classification based method in which features were extracted for each pixel in the green channel. These features consisted in the outputs of applying Gaussians and its derivatives up to order 2 for 5 scales (1, 2, 4, 8 and 16 pixels). Then, the features were normalized to zero mean and unit variance. To classify that information, k-NN classifier was selected among others since its performance was superior. They also compared their method with the previous methods

available [84], [109], [120], [121] in the DRIVE database [114] proving that the AUC obtained for this method was higher.

2.5.4.4 Tracking

In these approaches, the vasculature was found by tracing the vessel using its characteristics. An initial point is required for the algorithm which is usually a known position such as the location of the optic disc. At the beginning, angiograms were used. An approach developed by Liu and Sun in [122] used a tracking algorithm based in a 3-stage recursive procedure to detect vessels in coronary and radial arteries. They used an approach called detection-deletion, in which the detected segment is deleted from the angiogram to avoid the problem of tracking-path reentry in those areas. Matched filters were applied to the edges of the vessels to find the branches points. Their results show a range between 81% and 97% in the pixel detection of the vasculature. Retinal angiograms were used later by Zhou et al. in [105]. Their approach consisted in the use of Gaussian filters to improve the estimation of the vessels diameters. A technique that uses the information in the neighborhood area, called adaptive densitometric tracking, was used. An alternative to the initialization problems in tracking vessels in retinal angiograms was proposed by Tolias et al. [123]. Vessels and non vessels regions were found using an unsupervised clustering technique called Fuzzy C-means. Since this clustering method is based on membership, pixels along the vessels can be found by looking at the degree of properties being shared among them.

One of the first publications that used the tracking approach in retinal fundus images was the one developed by Chutatape et al. in [124]. In their paper, 4 properties of the

vessels were analyzed in order to detect the vasculature of the retinal image. These are: 1) Continuity of position since the centerline and edges of the blood vessels vary continuously, 2) Continuity of the curvature since the vasculature present bifurcations in a branching vessel, 3) Continuity of diameter since the vessel width varies along a vessel, and 4) Continuity of density since along the vessels, the density range varies relatively continuously. In a tracking algorithm, a blood vessel is defined by many vessel segments. Each segment, as it shown in Fig. 2.20, is defined by 3 parameters: direction (V_i), width of the vessel lumen (W_i) and centerline midpoint (C_i). In their algorithm, a Gaussian matched filter is used to detect the centerline of the vessel. Then, a Kalman filter is used to obtain the new vessel segments using the information of the previous ones [$S_1... S_i$]. Since the origin of the vessels can be found in the optic disc, the tracking algorithm starts from that point.

An approach published in 2010 by Vlachos et al. [125] used a multi-scale line-tracking procedure. In this approach, the authors perform tracking in different images scales. The results on all scales were combined, obtaining a vessel map. The initial points were found using a brightness selection rule and the end points were determined when the cross-sectional profile condition becomes invalid. Median filtering and morphological reconstruction were applied as post-processing steps to remove non-vessel objects.
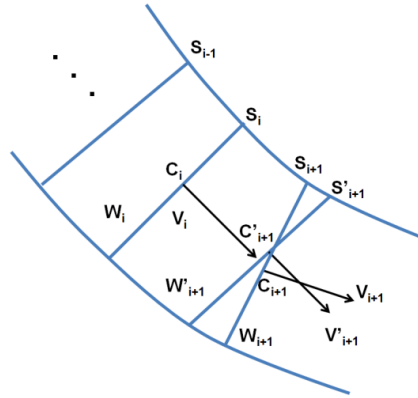
**Figure 2.20 Estimated vessel segment S'$_{i+1}$ and the actual one S$_{i+1}$ located by matched filter.
(Image courtesy of [124])**

Tracking methods need a starting and sometimes an end point. For that reason, different techniques such as matched filters are used to find these points. The main advantage of tracking methods is that they can provide accurate measurements of the width of the vessels and tortuosity. The disadvantage of this technique is that it may be confused by vessel crossings and bifurcations [126].

2.5.4.5 Others

Another method that has been applied in this area, and it is well-known for its properties in segmentation, is active contour (snakes) models. It can be found in the literature that Gooya et al. in [127] applied a level-set algorithm based on geometric regularization for the detection of blood vessels in humans. They applied their algorithm to synthetic images and retinal angiograms. A later approach developed by Al-Diri et al. in 2009 [128] used a "Ribbon of Twins" active contour model explained in [129] to segment and measure the retinal vessels. This algorithm was initialized using morphology to find the centerline. After the centerline was identified, two pairs of contours were

initialized for each side to be able to capture each edge of the vessel. In addition to the results presented in Table 2.2, they also reported results for the width vessel measurement using the REVIEW database [115]. The problem with this method is the high processing time to obtain the results. Al-Diri et al. reports in their paper that to obtain the segmented vessels in one image of the DRIVE database, 11 minutes were required.

Vessel enhancement has also been used for the segmentation of vessels. Yu et al. [51] used Frangi filters [130]. This method creates a vessel probability map by computing the eigenvalues of the second derivatives of Gaussian filtered image at multiple scales. Then, the second order local entropy thresholding was applied to segment the vessel probability map. Finally, a rule-based decision was applied to differentiate a lesion from a vessel; thus reducing false positives. A most recent approach developed by Yuan et al. [131] used a technique called VE-LLI-VO that is a vessel enhancement method based in local line integrals and variational optimization. This method is less sensitive to local intensity abnormalities. The authors state that it performs better than Frangi filters. This could be observed in Table 2.2, where their results for the STARE and DRIVE databases are compared with Yu et al. [51]. The current limitation of this method is the computation time, which is 4 hours. As the authors stated this time can be reduced by the use of graphical processing units (GPUs).

Since most of these methods used standard databases, a comparison among them is possible. A summary of the results of most relevant methods for vessel segmentation are detailed in Table 2.2.

Table 2.2 Results of vessel segmentation approaches.

Year	First author	Methods	Datasets	Results
1989	Chaudhuri	Two dimensional matched filters	DRIVE*	Acc = 0.877, AUC=0.788
1995	Gregson	Thresholding, morphology, fast fourier transform is applied to find the diameter of the vessel.	51 retinal images	
1998	Chutatape	Matched gaussian and kalman filters		Visual Verification Acc= 0.794 (for major vessels Acc=0.980)
1998	Tolias	Fuzzy C-means	3 images	
1999	Zana	Morphology using Hough Transforms	DRIVE*	Acc=0.938, AUC=0.898
2000	Hoover	Matched filters and thresholding	STARE	Acc=0.759, AUC=0.927
2002	Gang	Second-order gaussian filter	40 images	Acc=0.914
2003	Jiang	Adaptive Thresholding	STARE, DRIVE*	Acc=0.930, AUC=0.900 and Acc=0.933, AUC=0.891
2004	Vermeer	Laplace thresholding	STARE	Acc=0.929, AUC=0.919
2004	Niemeijer	Pixel based classification using k-NN	DRIVE	Acc=0.94, AUC=0.90
2004	Staal	Ridges, k-NN classifier	STARE, DRIVE	Acc=0.961, AUC=0.952 Acc=0.952, AUC=0.944
2006	Soares	2D Gabor Filters, bayesian classifier	STARE, DRIVE	Acc=0.967, AUC=0.948 Acc=0.961, AUC=0.947
2006	Sofka	Multiscale Matched Filters	STARE, DRIVE	
2006	Mendo-za	Detection of centerlines and morphological reconstruction.	STARE, DRIVE	Acc=0.948 Acc=0.946
2007	Jelinek	Gabor wavelets, linear discriminant analysis	27 fluorescein-labeled retinal images	AUC=0.90
2007	Ricci	Linear detector, SVM	STARE, DRIVE	Acc=0.97, AUC=0.96 Acc=0.96, AUC=0.96
2008	Lam	Laplacian operator and normalized gradient vector field	STARE	Acc=0.95, AUC=0.94
2009	Zhang	Matched filters and double sided thresholding	ZUEYE, STARE	Acc=0.95 Acc=0.95
2009	Al-Diri	Ribbon of twins active contour model	STARE, DRIVE	Sen/Spec=0.75 /0.97 Sen/Spec=0.73 /0.96
2010	Vlachos	Line tracking	DRIVE	Acc=0.929
2011	Marin	Neural Networks	STARE, DRIVE	Acc=0.952 Acc=0.945
2011	Miri	Curvelet transform and morphology	DRIVE	Acc=0.946
2011	Yu	Frangi filters and second order local entropy	STARE, DRIVE, Gold Standard	Acc= 0.946, Acc= 0.943, Acc=0.952
2011	Yuan	VE-LLI-VO	STARE, DRIVE	Acc=0.972, Acc=0.964

2.5.5 Optic disc Localization and Segmentation

The optic disc is one of the structures (besides the vasculature) that are the landmarks in the retina. Its shape is approximately elliptical and its width and height is around 1800 and 1900μm respectively [83]. The veins and arteries originate from it. The absence of the pigmented epithelium in this zone is responsible for the color of the optic disc in the retinal fundus image (yellowish). It is very common to see, as it can be appreciated in Fig. 2.21, a brighter central region inside the optic disc. This region which is called the "pallor" usually includes the cup.

Some considerations that must be taken into account by the reader are that the size and shape of the optic disc can vary significantly and that the color of the boundary of the optic disc (the rim) is brighter in the temporal side than in the nasal side In addition to those, a screening system should also consider the presence of diseases in the optic disc such as peripapillary atrophy, which appears as a brighter ring area that surrounds the optic disc [132], thus affecting the results of any boundary segmentation algorithm.

The knowledge of the location of the optic disc is very important since it can help identify other main parts in the retina such as the macula, fovea or pathologies [53]. Other approaches, as it was mentioned in the previous section, used the optic disc in vessel tracking. Many approaches have been developed not only to detect it, but also to segment its boundary. The segmentation is required for two important tasks: 1) To analyze the optic disc separately in order to detect abnormalities like NVD, glaucoma (using stereo images), and papilledema; 2) To remove the information of the optic disc in the retina in order to obtain better accuracy in the detection of pathologies in the retina. This latter procedure is used in most of the DR screening algorithms. Since the signature

of the optic disc is the most distinguishable of all the structures present in the retina, and it shares some pixel information with the bright lesions, DR algorithms avoid including features that contain optic disc information.
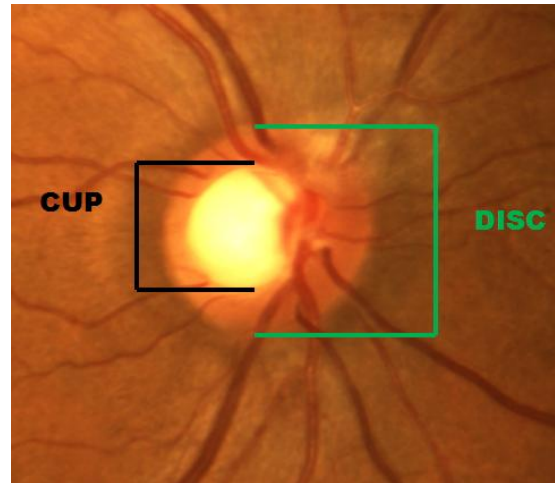
Figure 2.21 Parts of the optic disc.

2.5.5.1 Optic Disc Location

Since one of the properties of the optic disc is the bright intensity pixel values by which it is composed, one of the first published methods by Chaudhuri et al. in 1989 [84] used the intensity to locate the optic disc. In their algorithm they assumed that the only region with bright pixels in the image corresponded to the position of the optic nerve. For that reason, using the information of the intensity pixels, they look for the cluster which contains the higher intensity values.

In 1998, two published papers used the Hough transform methodology to locate the optic disc. This methodology, originally proposed to detect lines, has been used to detect accurately other shapes such as circles or ellipses. As it was pointed out in [53], this technique is well-suited to detect image noise that corresponds to the broken segments of the optic disc, which cannot be correctly detected in the segmentation. While the Hough

transform was used in both location methods, different methods for extraction of features are used. Kochner et al. [133] used steerable filters (1st order Gaussian with different orientations) to obtain the points that belong to the edges of the main vessels. These points were then fitted to an ellipse by Hough transform to find the correct location of the optic disc. Pinz et al. [134] used another method for feature extraction. In their method, the position (left or right) of the optic disc was known. Therefore, they restricted the search to 1/3 of the area of the image. The information of three imaging modalities of the scanning laser ophthalmoscope (SLO) modality was used: Argon-blue reflexion (ARC), Infrared and HeNe reflexion (IRC), Static scotometry (SK). In this approach, edgels (edge elements) were detected along the boundary of the optic disc. Morphology was used to remove edgels which are suspected to belong to a vessel.

Lee et al. in 1999 [135] also used the information of the intensity to locate not only the optic disc, but also the macula. In their work, they also used the shape information as a relevant feature for the localization. A matched filter with round shape, characteristic of the optic disc, was also used.

In a publication of Sinthanayothin et al. in the same year [83], they used the information of the vessels that are in the optic disc in addition to the bright pixel information. The vessels are one of the darkest structures in the retina and since the optic disc is one of the brightest ones, the variation that they obtain in a region containing the optic disc is high since the main vessels originate from the optic nerve. They analyzed these variations in regions of 80x80 pixels. These regions correspond to 1/7 of the retinal area, which covered the optic disc in the images that they used. The optic disc was

located in the point with maximum variance. To evaluate their method, 40 images were used obtaining a sensitivity/specificity of 99.1%/99.1%

Li and Chutatape in 2001 [136], combined two approaches. First, all the bright pixels in the images were selected and clustered in different areas in the retinal image. They applied the following criterion: if a cluster of bright pixels has less than 100 pixels, it was eliminated from the analysis since the optic disc contains more pixels than 100. After all the clusters were found, Principal Component Analysis (PCA) method was used. The vessel information present in the optic disc was used in this part. Ten regions containing the optic disc and vessels were analyzed with PCA finding the significant features (eigenvectors) which will project an image into a new space called "disc space". After finding this vector, distances were measured from the candidate bright pixels to their projection in the "disc space". The minimum distance indicates the center of the optic disc. In their results, they mentioned that their algorithm provides accurate results but no quantitative information was provided. In the same year, Lalonde et al. [137] published another method to locate the optic disc in fundus images using Hausdorff-based template matching technique on edge map, guided by a pyramidal decomposition for large scale object tracking. In order to find the optic disc, 3 assumptions were made: 1) A priori knowledge of the region in the image that contains the optic disc could be obtained from the field of view and the eye (left or right) from which the picture was taken, 2) The pixels that belong to the optic disc are brighter (not necessarily the brightest), and 3) A circular shape can be assumed for the optic disc. In their algorithm, potential regions containing the optic disc are found with pyramidal decomposition. The example in Fig 2.22 shows the results of 4 and 5 levels of decomposition of the image using the Haar-

based discrete wavelet transform in their dataset. After performing this operation and using the information of the first two assumptions, 10 candidates were selected to be the optic disc. With this selected candidates, canny edge detection was performed followed by Hausdorff-based matching (between the candidates and the ground truth template) to find which candidate fulfills condition 3. Their algorithm was tested using 40 low quality images and one metric besides the location rate was presented. Their results showed a 7% false detection rate with 80% area overlap between the ground truth and the optic disc found with this method.
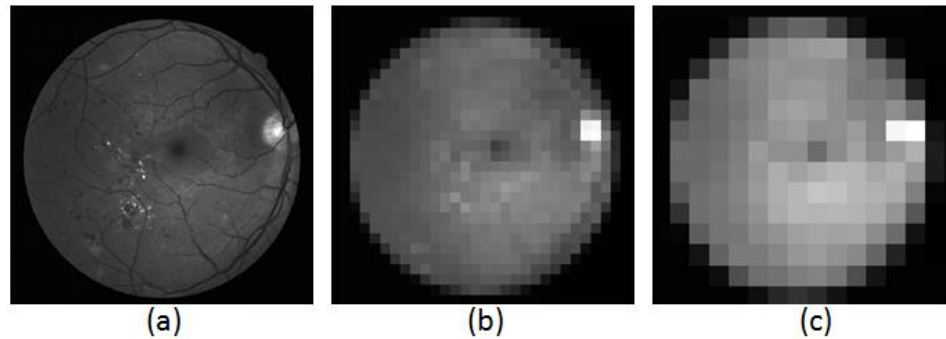
Figure 2.22 Pyramidal decomposition. (a)Green channel of the original image. (b)Four level decomposition, (c)Five level decomposition.(Image courtesy of [41])

One of the problems of the previous methods was that they were not robust enough to work well with retinal images with lesions. For that reason, Hoover et al. [54] in 2003, selected 81 images showing a variety of retinal diseases that can affect the location of the optic disc to test their methodology. They used the convergence of retinal vessels to find the optic disc. This concept that was previously applied by Akita et al. [112], who use the fact that the optic disc is the origin of the blood vessel network. In their approach, they used a method previously developed by them called Fuzzy convergence [138]. This method is a voting-based method. First, they obtained six binary vessel segmentation

maps from different scales. Then, each line-like shape was modeled by a Fuzzy segment. After that, an image map was created with the summation of votes of the Fuzzy segments at each pixel. With, the smoothed version of this image, a threshold value was applied to find the strongest point(s) of convergence. If they cannot determine a point for the location of the optic disc, the green channel was equalized and Fisher's linear discriminant was applied to the regions that contain the brightest pixels to detect it.

Osareh et al.[139], also used matched filters to locate the optic disc. In their approach, 75 images of size 540x536 pixels were tested. The template of this approach was obtained by averaging the OD region of 25 color-normalized images to produce a 110x110 template image. In 2004, Lowell et al. [132] presented an approach to locate and segment the optic disc. In their approach, a correlation filter was used to locate the optic nerve head. They used a template that consists of a Laplacian of Gaussian with a vertical channel in the middle that corresponds to the major vessels in the optic disc. This template was correlated in a set of 100 images. Although the size of the optic disc varies in their dataset, the size of the template was fixed since their main interest for the location is that the detected point is found within the optic disc. By using the Pearson-R correlation coefficient, the location of the optic disc was found for the maximum value. A correctly locate optic disc center was defined by an area equal to a radius of 15 pixels of the center located by an ophthalmologist.

The inclusion of vessel information in the detection of the optic disc increased the performance of many algorithms. As it has been previously discussed, the vessels present in the optic nerve or their vertical position were used as a point of convergence to estimate the location of the center of the optic disc. Besides the already mentioned

properties of the vasculature to detect the optic disc, Foracchia et al.[140] used the location of the main arcades of the vasculature. They based their algorithm in the anatomy of the vasculature in which the branch vessels presents higher divergence with respect to the main vessels. This effect can be more clearly observed in the temporal side in Fig. 2.23, where these vessels bend toward the macula. It can also be observed that the main arcades of retinal vessels in both sides (nasal and temporal) follow a specific trajectory that can be geometrically approximated by two parabolas. These two parabolas share a common vertex, which was used as an indicator of the location of the optic disc. In order to test their algorithm, two methods [106], [141] that segment the vessels were used to measure the vessel directions.
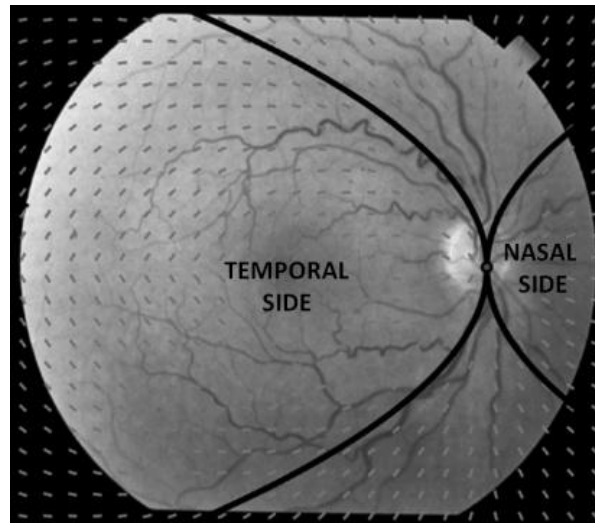
Figure 2.23 Vessel directions for arbitrary points and the parabolic model of main vessel course (black curves). (Image courtesy of [140])

The method of Zana and Klein to segment vessels described in the previous section was used by Tobin et al. in 2007 [142]. In order to use their method in retinal fundus images, the red-free fundus images were inverted so the vessels appear with high intensity values as they appear in the fluorescein angiograms. This method is interesting

since they used the information of the properties of the vessels in the optic disc. Four different features were extracted from each image: 1) Luminance, since it is well known that the optic nerve reflects the fundus camera illumination appearing very bright in the fundus image; 2) Vessel density, since the vessels are most dense in the optic disc region because they enter through it; 3) Average vessel thickness, since the width of the main vessel arcades that originate from the optic disc is higher than the vessel thickness in other regions of the retina; and 4) Average vessel orientation, since the vessels that originate from the optic disc are usually perpendicular to the horizontal axis of the retina. To calculate these 4 values in the images, the information that the optic nerve corresponds to a 5 degree angle in the direction of the macula respect to the horizontal axis of the image is used to calculate the size of the regions to be analyzed. By using this fact, the diameter of the optic disc (1DD) for an image of 50 degree centered in the macula is 130 pixels. For the luminance, a window of 1DDx1DD was used while for the other 3 type of features, a window of 0.6DD x 3DD was used since this shape helps to find the vertical vessels characteristic inside the optic disc. A Bayesian classifier was used to determine the location of the optic disc using these 4 features. The method was tested in a population of 269 patients (394 images) containing eye diseases such as AMD, choroidal lesions, Stargardt disease, etc.

Another interesting method published in the same year was the one developed by Niemeijer et al [97]. In their methodology not only the optic disc was located and segmented, but also the macula and the main arcades were located. This algorithm was based in a point distribution model (PDM) in which 16 points were selected from each image as it is indicated in Fig 2.24. The points were selected for 500 images in the

training stage. With these points, the PDM can be obtained by computing the mean and the covariance matrix from all the images in the training set. From the latter estimate, the eigenvectors with the largest eigenvalues were selected in a matrix ϕ so any set of points can be modeled by the mean plus ϕb, where b represents variations in location, rotation or scaling of the points. Then, a cost function which is based on vessel properties; outputs of Gaussian filters, their derivatives and invariants at different scales; and the RGB values was calculated from each image given a set of points. This cost function was optimized to find the minimum value using three steps based on Simulated Annealing, dynamic programming and Powell's optimization. After the convergence in the third step, the final set of points for the image was obtained.
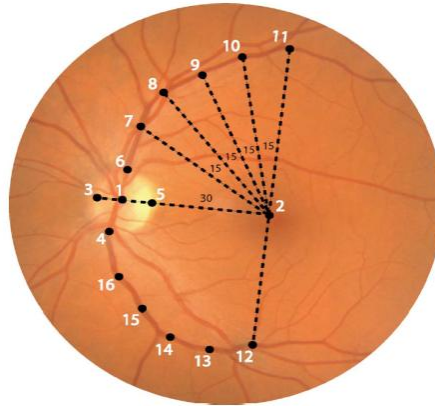
Figure 2.24 The point distribution model proposed by Niemeijer et al. on a retinal image. (Image courtesy of [97])

Note that this method also recognizes if the eye is left or right since in the training stage, all the right eye images were flipped to the left position and the cost function was found for the original image and the flipped version of the image. For that reason, if the image corresponds to the right eye, its cost will be higher than the cost of its flipped version.

As it was indicated in the pre-processing subsection, one of the characteristics present in retinal images is the non-uniform illumination due to vignetting. Fixing this problem helps the algorithms obtain more precise results. For that reason, Youssif et al. [89] in 2008 applied illumination equalization and adaptive histogram equalization in order to improve the quality of the image. After this process, optic disc candidates were selected using a threshold rule to the highest 4% of the brightest pixels in the retina. In addition to that, retinal vessels were extracted using the Chaudhuri et al. method [84] described before with Otsu's global threshold algorithm to obtain the binary vessel map [143]. In their approach, 4 different sizes of templates (241x81, 361x21, 481x161 and 601x201) were used to match the structures in the vessels at different scales.

In 2010, Aquino et al. [76] presented a method to detect and segment the optic disc based only on the intensity content of the green channel of the image. Three candidates of optic disc were extracted as follows: 1) Maximum and minimum filters are applied to the image, the pixel with the highest variance among the output of the filters will be the first candidate; 2) A second candidate is selected by calculating the variance of all the pixels within windows of 71x71; the pixel with maximum variance which also has 10 bright pixels in its neighborhood is selected; in this case the bright pixels are defined by applying Otsu's method to the blue channel of the image; 3)The highest intensity value pixel after applying the low pass filter to the green channel is selected as the third candidate. By comparing the distances between these candidates, the optic disc was located at the centroid. If one of the candidates was far away from the other two, it was eliminated of the analysis. The OD obtained by the maximum variance method was chosen if the three candidates are too far away from each other. This method uses the

1200 images of the available online database MESSIDOR [47]. Since these images do not have a ground truth of the position of the optic disc, the images were graded by 4 ophthalmologists. In the same year, Mahfouz et al. [144] presented another approach that did not require the segmentation of vessels to detect the optic disc. This approach has a great advantage with respect to the other ones since it only needs 0.46s of processing in comparison with other methods that have good results but need more than 1 minute to obtain higher results. To obtain this fast localization, the image was projected in 1D signals. First, two feature maps were obtained: the first one was obtained by calculating the difference between the horizontal and vertical edge maps and dividing the result by the intensity map; and the second one was obtained by calculating the summation of the edge maps and multiplying the result by the intensity map. Then, the feature maps were projected. The first map was projected by sliding a rectangle window of length equal to the retinal diameter and width approximately double of the size of the main vessel disc through the horizontal axis. In this case, the peak was expected to be near the optic disc, which was where the major concentration of vessels in the vertical direction is found. The second map was projected by sliding a square window of the size of the optic disc diameter. The maximum peak will define the location in the vertical axis. To improve the robustness of the location of the optic disc, an additional step was added. In this last step, the possible candidates of the optic disc were analyzed using the intensity value information. To do so, a score was calculated using the information of the segmentation of the brightest 10% pixels in regions of 2DDx2DD (centered in each candidate). This score was found by calculating the eccentricity of the largest brightest object in the analyzed region. To test their methodology, 4 publicly available databases were used,

which include the previously mentioned STARE and DRIVE. The new databases included in the evaluation of the performance of this algorithm were DIARETDB0 [145] and DIARETDB1 [146].

An approach presented by Lu and Lim in [147] used linear operators to locate the optic disc. First, the lightness component was extracted from the Lab color space of the retinal image. Then, a smoothing filter described in [148] that combines geometric closeness and photometric similarity was applied to the image. Next $n=R/8$ line detectors of $p=R/8$ pixels of distance at multiple orientations were applied to the image, where R is the radius in pixels of the analyzed retinal image. By looking at the image variation along those lines, maps were created with the maximum and minimum variation as it is shown in Fig 2.25c. This variations map was binarized using a threshold according to the number of segments and then it was convolved with the mask shown at the top left corner of Fig 2.25d. The difference of the retinal images pixels between the different peak centers in the image and their surrounding pixels were calculated using two concentric circles of different ratios. When the difference is positive, it can be assumed that the circle with less radius contains a brighter object than the surrounding pixels such as the optic disc. By combining the image intensity difference and the peak amplitude after the convolution, a score was obtained. This score determines the center of the optic disc.
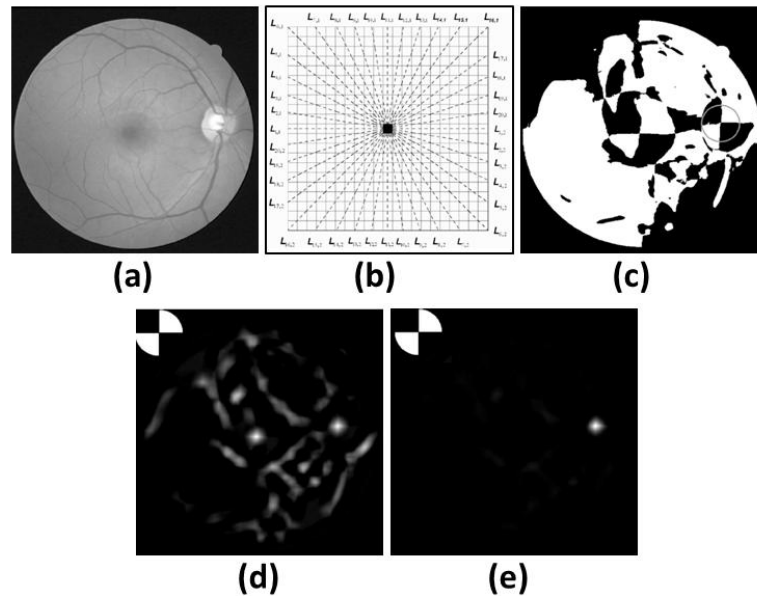
Figure 2.25 Procedure applied in the Lu and Lim approach. (a)Original image, (b)Set of line detectors at 20 orientations, (c)Binary orientation map, (d) Peak image after the convolution mask that appear at the top left corner is applied to c, (e)Score image for optic disc detection. (Image courtesy of [147])

Although their approach achieves very good results, the authors stated that the algorithm could fail in cases where the optic disc was darker than the surrounding areas and does not have a clear circular shape. A more recent approach by the same author [93] detects the optic discs with more accuracy. This method works in downsample images. It also reduced the area for the search of the optic disc by using [144]. Then, a method called circular transformation was used to find possible boundary pixels. For each pixel in the retina, this method detects multiple pixels with the maximum variation along 180 evenly-oriented radial lines of length R/5, where R is the radius of the retinal image. The authors report an execution time of 5s for the detection of the optic disc in STARE images.

Recently Yu et al. [149] presented a method to detect the optic disc. The method was based on matching filtering as previous approaches. The first template matching, which

was applied to the lightness component of the CieLab, was used to detect possible OD

candidates. Then, the OD was located using vessel information. To do so, a directional

matched filter as [84] in the green channel was applied within the OD candidates.

Table 2.3 Results of the optic disc detection algorithms

Year	First author	Methods	Datasets	Results
1999	Sinthanayothin	Highest average variation	STARE, 100 images	Acc=0.420, Acc=0.804
2001	Lalonde	Haussdorf template matching-pyramidal decomposition	STARE,40 images	Acc=0.716, Acc = 0.800
2001	Walter	Largest brightness connected object	STARE, 75 images	Acc= 0.580, Acc =1
2001	Li	Brightness guide, PCA model-based		Qualitative results
2002	Osareh	Average OD-images model-based	75 images	Acc=0.904
2002	Chrastek	Highest average intensity	263 images	Acc=0.973
2003	Hoover	Fuzzy convergence	STARE	Acc=0.890
2004	Foracchia	Geometrical model based	STARE	Acc=0.975
2004	Lowell	OD Laplacian of gaussian template	100 images,	Acc=0.960
2007	Tobin	Vasculature properties - Bayesian classifier	394 images	Acc=0.904
2007	Niemeijer	Point distribution model	500 images, 100 images wih pathologies	Acc=0.984, Acc=0.940
2008	Youssif	Vessels' direction matched filter	STARE, DRIVE	Acc= 0.988, Acc= 1
2010	Mahfouz	Projection of images features	STARE, DRIVE, 4 databases*	Acc=0.926, Acc=1, Acc=0.970
2010	Aquino	Statistical and frequency information of the intensity green plane.	1200 images MESSIDOR	Acc=0.988
2011	Lu+Lim	Line operators.	4 databases*	Acc=0.974
2011	Lu	Circular transformation	STARE, ARIA, MESSIDOR	Acc=0.995
2012	Yu	Matched filters	MESSIDOR	Acc=0.990

*All the images of the 4 databases: STARE, DRIVE, DIARETDB0 and DIARETDB1

2.5.5.2 Optic Disc Segmentation

As it was explained before, the segmentation of the optic disc is very important for

accurate detection of optic disc diseases. Segmentation methods have not been explained

before because it is very common to find the location of the optic disc before the application of segmentation. In fact, some of the methods described below are the extensions of the work presented for optic disc location.

Active contours model is a technique that is very common in image segmentation. This method, also called snakes, may be understood as a special case of a more general technique of matching a deformable model to an image by means of energy minimization. In this method a curve (snake) is initialized and it evolves at each iteration, minimizing the internal and external energies. The following equation shows the energy of the snake [150].

$$E_{snake} = \int_0^1 \frac{1}{2}(\alpha|X'(s)|^2 + \beta|X''(s)|^2) + E_{ext}(X(s))ds \qquad (2.23)$$

where $X(s)=(x(s),y(s))$ is a parametric curve with $0 \leq s \leq 1$, α and β are coefficients to control the snake tension and rigidity respectively, and E_{ext} is the external energy, which can be replaced by an edge map or gradient vector flow (GVF) to overcome the problems in the boundary concavities produced by the edge map.

Another common technique to find boundaries of structures in images is the Hough transform. This technique is used to separate features of a particular shape in an image. Originally developed to detect lines, it has been extended to detect circles, ellipses, and other forms that can be specified in some parametric form.

B. Level Sets

One of the first well known methods to segment the boundary of the optic disc in the retina was the one developed by Mendels et al. [151]. The RGB images were changed to the YIQ basis and the luminance domain was used in the process. Then, they compared

two methods to remove the vessels: minima detection and morphology, being the last the one they used to get rid of the vessels in the optic disc in order to create a smooth image to apply active contours. The initial curve was set next to the real boundary and GVF was used to find the real boundary. Nine images of 285x400 pixels were used to test their algorithm. Accurately detected boundaries were reported to be found using between 50-250 iterations, but no quantitative results were presented. In 2001, Walter et al. [152] proposed a method based in watershed segmentation to find the optic disc boundary. First, they located the optic disc under two assumptions: 1) the optic disc is one of the brighter regions in the retina, and 2) the dimension of the optic disc is higher than other bright regions such as HE. After finding the optic disc using the luminance channel of the HLS color space, the red channel was selected for the segmentation. Then the image was filtered to eliminate large grey level variations and the vessels were removed with morphology. The gradient was calculated from the filtered image and the crest determines the contours of the optic disc. Thirty images were used to test their algorithm, being the optic disc correctly located in all of them and the boundary correctly identified in 27 images. As they stated in their paper, the problem in the remaining 3 images was the low contrast that the retinal fundus images had and the saturation of the red channel, which is very common in these image as we have indicated in the pre-processing subsection. In the work presented by Osareh et al. [139], the same approach with active contours that Mendels et al. [151] applied was used. Their contribution is the generation of a smooth image to be used by the active contour algorithm. Instead of using grey level morphology, color morphology was implemented in their approach. Different color spaces were analyzed, being the Lab color space the optimal one to obtain the

homogeneous region for the active contours. Their result shows a 90.32% of overlap area for 75 images.

One of the latest published approaches to segment the optic disc that used level sets can be found in [149]. Yu et al. used a fast hybrid level set model described in [153]. The images were pre-processed using alternating sequential filtering and morphological reconstruction to remove inhomogeneities in the OD. Since the final curve of the segmentation was not smooth due to the presence of strong vessels in the OD, a least-squares ellipse fitting was applied. The method was tested in the 1200 images of MESSIDOR obtaining an Acc =84.4%.

C. Hough Transform

Canny edge detector and Hough transform was used by Chrastek et al. [154]. First, the optic disc was located by applying an average filter and finding the area with maximum intensity. Then a non-linear filtering was applied to reduce the noise in order to apply the edge detector. Finally the boundary was found by using circular Hough transform. The criterion to evaluate the performance of the boundary segmentation was visual, obtaining an accuracy rate of 81.7%.

The work described by Aquino et al. [76] in the detection of the optic disc was also extended to the segmentation of the boundary of the optic disc. After they find the position of the optic disc, a region of 400x400 pixels was extracted. This selection was performed because the efficiency of the segmentation is high when the search area is decreased. As it was indicated previously, the red channel is sometimes preferred for the segmentation since the vessels are not so notorious in this color plane. As a consequence,

their approach uses the green and the red channels independently for the segmentation, and the best results (not automatically chosen) were presented. In their approach, morphology was used to eliminate any blood vessels than can affect the optic disc boundary segmentation. Binary maps with the boundary candidates were obtained after applying Prewitt edge detector, Otsu's thresholding method and morphological operations. In this approach, Hough transform was used to find the final boundary. Their algorithm was tested using the 1200 images of MESSIDOR. An ophthalmologist marked the boundary of the optic discs. This information is available online for future comparisons [155]. An overlap area of 86% was obtained for the whole dataset.

D. Others

In a recent paper of Lu et al. [93], which has been described in the optic disc location section, the authors report an accuracy rate of 93.4% and 91.7% for the optic disc segmentation in retinal images from STARE and ARIA databases, respectively.

2.5.6 Localization of the Macula and Fovea

The macula appears in the temporal side to the optic nerve. In an image without lesions, the macula region is usually darker to the surrounding retinal tissue. This color is due to the high presence of caratenoid pigments in the retina. In addition to that, the retinal pigment epithelial (RPE) presents pigment granules in this area. The center of the macula is the fovea, and it usually does not present structures like vessels near its center. An important property of the macula area in a retinal fundus image is its location. By definition the fovea is located approximately at 2-2.5DD from the optic disc and at an

angle range from the horizontal line that includes the center of the optic disc in retinal images as it is shown in Fig. 2.26.

As it was specified in the previous section, the first relevant feature used to identify structures in the retina such as the optic disc was the intensity value information. This can be found in one of the papers of Lee et al. [135] (mentioned in the previous section), which assumes that the area of the retina with low average intensity contains the macula.

In the work presented by Tobin et al. [142], the relative position between the optic disc and the fovea was used. In their analysis the fovea was fixed at a distance of 2.5DD of the optic disc center at an angle in the range [-24° 17 °] from the horizontal axis in the retina. They find the OD center based on their method in parabolas explained in [140], so the vertex of the two parabolas in Fig. 2.23 is fixed to that location in the *x* direction. Then, theses parabolas were rotated in the angle range previously specified to match the main arcades previously segmented in the retinal image. A detection rate of 92.5% was obtained in 345 images.
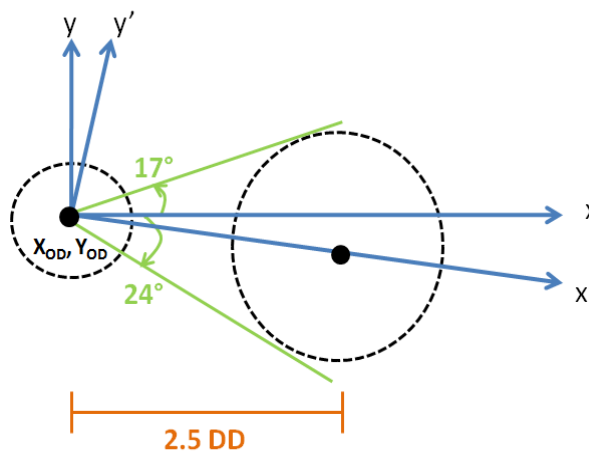
Figure 2.26 Coordinate system used to detect the fovea in [142] (Image courtesy of [142])

Niemeijer et al. [97] used the method described in the optic disc location to detect the main arcades and the macula obtaining an accuracy rate of 93.2% and 94.4% respectively. By using the same methodology explained for the optic disc detection, Lu et al. [147] also found the macula in the images. In Fig 2.25d, it can be observed that also the pixels in the center of the macula have high intensity. For this reason, instead of looking for a positive difference, peak pixel values in Fig 2.25d constrained to the maximum negative difference were extracted as a relevant information. This indicates that the surrounding pixels have higher intensity values than at the peak center pixel such as the fovea. Although the optic disc detection algorithm was not initially developed for the detection of the fovea, this approach can be extended as it was explained in their work. Their results demonstrate that the method works for images where the macula is discernible in 98.2% of all the images in STARE, DRIVE, DIARETDB0 and DIARETDB1.

2.5.7 Localization and Segmentation of DR pathologies

As it was indicated before, MAs are the first sign of DR. As a result, many approaches have been focused in the detection of these types of lesions. The other most common task is the detection of bright lesions especially HE. Two main approaches for the classification of DR pathologies have been used in the past years: top-down and bottom-up. In the first one, features that characterize abnormalities are extracted per image and a classification algorithm is applied to distinguish normal from abnormal retinas. In the second type, features are extracted but for pixels or small areas in the retinal images. These methods are usually applied in the segmentation of specific lesions

such as MAs, HE, etc. The results are presented in terms of sensitivity per pixels, number of false positive rate per image, sens/spec per image and/or AUC. We summarize the algorithms that have been developed for both types of approaches in the following paragraphs.

2.5.7.1 Bottom-up approaches

A. Red Lesions

In this section, we grouped approaches that were focused in detecting microaneurysms and hemorrhages. This is one of the topics with most published work. Most of the papers at the beginning used a morphological operation called top-hat transform which is defined by the difference of the image after being applied a morphological closing operation and the original image. In Eq. 19, we present how the top-hat transform is applied for the detection of MAs.

$$T = \min_{i=0...n} \left[\Phi(I, \lambda_{\frac{i\pi}{n}}) \right] - I \qquad (2.24)$$

Where I is the image to be processed, and $\Phi(a, b)$ represents the morphological operation closing of image *a* by the structuring element *b*. Notice that the structural element γ is linear with *n* orientations.

First works in the detection of microaneurysms involved the use of fluorescein angiograms since it provides better contrast for red lesions. One of the first approaches was published in 1983 by Lay et al. in [156]. They applied top-hat transformations with a linear structuring element at different orientations. By doing so, MAs, which are circular regions, are distinguished from vessels, which are connected elongated structures. The algorithm was tested in 10 angiograms. It detected 58% of the 177 MAs found in those

images. This algorithm was later improved by the authors. The published paper by Baudoin et al. [157] includes the addition of extra morphological operations to remove the noise; thus reducing the false positives. The algorithm was tested in 25 angiograms with 1045 MAs, detecting 70% of them.

In 1992, Spencer et al. [158] applied two types of pre-processing to the images. First, the authors applied a radiometric correction for the illumination of the negatives. Then shade correction to remove the choroidal background fluorescence was applied. In their approach matched filtering was used to detect MAs. The kernel was a circularly symmetric 2D Gaussian curve with σ=1. In addition, vessels were identified using the same kernel but with σ=2. Additionally, the shape was analyzed to identify long linear structures. The algorithm was tested in 6 angiograms obtaining comparable results with the clinicians. However, the clinicians performed much better in the gradings of photographs than angiograms. Few years later, Spencer et al. [60] proposed to detect vessels before extracting MA candidates. The vessels were detected using morphological openings of the pre-processed image using a structure element long enough (11 pixels) to avoid capturing MAs and rotated in 8 orientations given the structure of the vasculature. These vessels were removed from the shade corrected image. The output image was thresholded to obtain MA candidates. In order to further improve the specificity of the algorithm, a region growing algorithm was initiated in the candidates; and shape intensity was measured in the new object. By using the information of the features, a rule-based classifier was applied in 4 digitized angiograms of 1024x1024 pixels. The specificity increased to 86% with sensitivity of 82% in the detection of MAs with 100 false positive pixels per image. The results were good but only in a very few images.

More images were studied in the approach developed by Cree et al. [159]. In their work, they included more features such as intensity of the candidates as well as the peak response of the matched filter used to find the candidates. They also made a comparison of different classifiers: linear discriminant analysis, neural networks, and rule-based, being the latter the one that produced the best results. The training and testing sets consisted of 64 and 20 angiograms of 1024x1024 pixels respectively. The algorithm detects 82% of the 297 MAs found in the testing set with 5.7 false positive per image. The result was compared with 4 independent clinicians that obtained the same sensitivity with 3.2 false positive per image.

The use of red-free photographs instead of angiograms was introduced by Hipwell et al. [160] in 2000. This algorithm that was based on [159], achieved 43% sensitivity with 0.11 false-positive per image in the detection of 88 MAs in 62 images. Although, this operating point has low sensitivity for the detection of MAs, it obtains a good performance in the detection of DR in retinal images, which is the main goal of the proposed algorithm. The model was tested in 3783 photographs obtaining sens/spec of 81%/93% for the detection of cases with MAs.

Sinthanayothin et al. [161] presented and algorithm based in MOAT operator and recursive region growing segmentation (RRGS) to detect microaneurysms and hemorrhages. The MOAT operator is basically an enhancement to the edges in the images in frequency domain. To do so, a high pass filter of the shape of an inverted Gaussian was applied to the difference of the image and its edge gradient function. This modification was performed in order to preserve the size of the lesion that was modified when only the image was filtered. The RRGS segments pixels with similar information

into a whole region. By combining this method with thresholding, microaneurysms and hemorrhages candidates were selected. Since vessels were also captured in the process, a neural network was used to identify them. A total of 30 images (14 with red lesions) were used to test the algorithm, obtaining a sens/spec of 77.5%/88.7%. The same basis of this algorithm was tested in more images by Usher et al. [82]. They enhanced the images with locally adaptive contrast enhancement. In addition, color normalization was applied to the images. The algorithm was trained with 500 patients and tested in 773 patients. Per patient basis, a sens/spec of 95.1%/46.3% for the detection of any pathology (i.e., HE and red lesions) was obtained. The algorithm was also tested for detecting DR, obtaining sens/spec of 70.8%/78.9%.

Pixel based information was introduced in 2005 by Niemeijer et al. [92]. This method used the algorithm proposed by [60] and [91]. In the pre-processing stage, it also includes bright lesions removal using the information of the shade corrected image. By using this, they decreased the number of false positives due to the "islands" that appear when the bright lesions were close together. The red lesion candidates were extracted with a hybrid system that consists of the union of the candidates extracted with the method of [60] and [91] and the proposed pixel-based classification algorithm. The latter one extracts candidates through a classification process where features in each pixel (MAs diameter is approximately 4 pixels) were input to a k-NN classifiers (k=55). The set of features consists of pixel intensities and first and second order Gaussian derivates at various scales. In order to detect red lesions that are larger than the structuring element in [60], the vasculature was removed by applying a vessel segmentation technique previously described in [119]. In addition to the features proposed in [91], color information and the

response of Gaussian filterbank outputs were added. A total of 68 features was the input of a k-NN with k=11. The system was tested in 50 images and achieved a sens/spec of 100%/87% per image and a sens of 31% with 0.8 false positive per image. Although the method has a good performance, region growing introduced limitations in the detection of candidates [26]. This was found for MAs that were present near vessels, cluster of MAs, or unusual background texture. To solve this, Fleming et al. [162] proposed a method based on localized enhancement to detect MAs. Even though this method also used the top-hat transform as in [60], a pre-processing stage was performed to the images. The noise was removed by applying a median filter of 3x3 to the green channel. The result of this operation was convolved with a Gaussian curve of σ=2. Finally the resulting image was normalized by dividing it by its standard deviation (SD). Similar to previous methods, the top-hat transformation was performed at 8 orientations. After obtaining the candidates, a sub-region of 121x121 pixels was selected, and region growing based on watershed was performed with the gradient information of this sub-region. To extract features, contrast normalization was performed to the new region by diving it by its SD after applying a high pass filter to it. This operation was performed in order to remove gradients that were not associated with MAs. In their method, they also proposed to analyze the vessel information in this sub-region; thus reducing the time of pre-processing since they will only analyze in the area of the selected candidate. Moreover, they introduce the possibility of detecting MAs within the vessel. A total of 9 features were the input to the k-NN classifier with k=15. The algorithm was trained using 78 images (71 with MAs) and tested using 1441 images (356 with MAs) of 2160x1440 pixels. A sens/spec of 85.4%/83.1% was obtained in the classification of images with

MAs. The detection of MAs was asses by analyzing 236 images (71 with MAs). The algorithm was able to detect as candidates, 63.7% of the MAs identified by the clinician.

Template matching was used by Quellec et al. in [163]. But instead of applying it to the image, which could have noise and lighting variation, it was applied to the output of the wavelet transform. The template was based in 2-D rotation-symmetric generalized Gaussian function. In addition the low and high frequency scales from the wavelets response was not considered in order to remove noise and slow image variations. A comparison of the coefficients of the wavelet response of the image and the wavelet response of the kernel was performed. By thresholding the difference of both outputs, the locations of the MAs were found. A total of 120 images from 3 different imaging modalities (color photographs (CP), green filtered photographs (GFP), angiographs) were used to test the algorithm. The authors evaluate the performance using sensitivity/positive predictive value (PPV), obtaining 90.24%/89.75% for GFP, 93.74%/91.67% for angiographs, and 89.62%/89.50 for CP.

Given, the great amount of algorithms to detect microaneurysms, Niemeijer et al. [164] presented in 2008 an online competition called Retinopathy Online Challenge (**ROC**). In this contest, 50 images for training and 50 images for testing were made available to the users. The ground truth, obtained by the logical disjunction of the annotated images of 4 experts, was also available for the training set. To find the performance in the testing set, a *XML* file with the results has to be uploaded in their webpage [165]. In addition to the annotated images, classes for the MAs were also indicated. From the 343 objects labeled as MAs, 92 were considered to be subtle, 192 are regular, 59 are obvious, and 37 are close to vessels. This was made due to the difficulties

of detecting MAs in the retina. At the time the paper was published, only 6 groups reported their results, being the Latim group [163], the one that obtained the highest score (0.381). Currently, there are 12 groups that sent their result to the organizers, being the DRscreen group [166] the one that obtained the highest score (0.434). This algorithm is described later in this section.

Zhang et al. [167] presents an approach to detect microaneurysms based on multi-scale correlation filtering (MSCF). This method was based on performing matched filtering with Gaussian kernels at different scales. Since MAs are circular of different size, 5 scales were used. The highest correlation values for the different scales will determined the final response for the detection of MAs candidates. The final response will have objects different than MAs such as vessels. Therefore, a dynamic thresholding was applied. To perform a fine level segmentation, a total of 31 features (information of shape, intensity and response of Gaussian filterbanks) were obtained for each candidate. In a training stage, the features for the true MAs and false MAs were grouped in different categories in order to determine the discrimination criteria for candidates in the testing images. The approach was tested using the **ROC** [165] and the DIARETDB1 databases, obtaining an average of 0.357 and 0.713 false positives per images respectively.

Recently, a publication [166] from Antal and Hajdu has stated that the previously proposed methods for the detection of MAs can only deal with specific problems. However, if these approaches are combined, the detection rate of MAs could potentially increase. With this hypothesis, the original image and 3 methods of pre-processing ([90],[168], [169]) were combined with 5 methods to extract candidates ([170], [60], [171], [172], [167]). Optimal combinations were found with simulated annealing [173]

which is a forward feature selection technique. The method was tested in 199 images. Although the number of false positive per image was increased with respect to individual methods, the sensitivity per lesion was highly increased in 24% respect to the best individual method for the whole dataset [172]. As it was mentioned before this method is the one that obtained the highest score in the **ROC** contest.

B. Bright Lesions

In this section, the approaches that were focused in the detection of HE and CWS are explained.

One of the first methods to detect HE was presented in 1993 by Phillips et al. [174]. In their method, the non-uniformities of illumination were eliminated with shade correction. Then, they used two different type of thresholdings for detect HE. A global thresholding for detecting large confluent HE in a region of 256x192 pixels, and local thresholding by using blocks of 32x32 pixels to detect smaller, lower intensity HE. To test their approach 14 images of 416x288 pixels were used, reporting sensitivity between 61% and 100%.

In 2000, Ege et al. [175] presents a system to detect lesions of DR. First, a mean filter of 3x3 was applied to images of size 640x480 pixels in order to reduce the noise. Additionally, the retinal background was estimated using a median filter of size 31x31 pixels. By estimating this background, the bright lesions (HE and CWS) can be extracted by thresholding the original image with respect to the intensity of the background pixels. Features such as perimeter, minor axis variance, and information of the RGB color space were extracted for each candidate. Those features were input a to k-NN classifier. The

algorithm achieved sensitivity of 99% and 80% in the detection of HE and CWS in 134 images.

Wang et al. [58] presented a pixel based classification to detect HE. First, the non-uniform illumination was corrected using Eq. 8. Features for each pixel were extracted using a transformation from the RGB space into brightness and chromacity. Those features were input to a minimum distance discriminant classifier. The approach was tested in 154 images (54 with HE). The algorithm achieved a sens/spec of 100%/70%.

By using the same approach for red lesion detection, Sinthanayothin et al. [161] detect HE by thresholding all the pixels with higher intensity than the median intensity of the background. The algorithm was tested in 30 images (21 with HE) and its performance was measured in patches of 10x10 pixels, reporting sens/spec of 88.5/99.7%.

An approach developed by Walter et al.[176] detect HE using thresholding and morphology. First, the authors removed the information of the vessels with morphological operations in order to minimize the effect of bright regions between dark vessels. Then, the images were thresholded by using the information of the high grey level variation. Finally, the contours of the HE were found using morphological reconstructions. The algorithm was tested in 30 images (15 with HE). Two false positives were detected. Only the images with HE were analyzed in more detail, obtaining a mean sensitivity of 92.8% and mean predictive value of 92.4%.

In 2007, three main publications were presented for the detection of HE. Two of them were based in Fuzzy c-means clustering [80], [177] and the other one in a combination of classifiers [178]. The latter used two k-NN classifiers to detect bright lesions. First, they extract candidates using the information of the output of 14 filters based on Gaussian

derivates. By feeding this information to the k-NN classifier, candidates were extracted. After that, 83 features were calculated per candidate. The features represents shape properties, information of the green channel and the Luv space, mean output of the filters used to extract the candidates and information of the distance to the closest red lesion which was found with the algorithm previously described in [92]. These features were input to a k-NN for detecting bright lesions. Finally a third classifier was used to differentiate HE, CWS and drusen. This classifier will be used the same features extracted for the second classifier but only in the candidates assigned to be bright lesions. In addition, other features such as the number of red lesions in the image, the number of detected bright lesions in the image and the probability of cluster were extracted. The features were input of a linear discriminant analysis for labeling all the bright lesions. The algorithm was trained using 130 images with 1113 HE and 45 cotton wool spots. The performance of the algorithm was measure using 300 images (42 with HE, 30 with cotton-wool, 54 with drusen spots and 200 normals). The algorithm achieved an AUC of 0.95 for the detection of bright lesions with sens/spec of 95%/86% for HE, 70%/93% for CWS and 77%/88% for drusen detection.

In the approach of Osareh et al. [80], they applied histogram matching and enhancement using Eq. 18 and 19 to the images. Although the enhanced image presented in their approach have a good contrast between HE and background, the authors claimed that the best color space to detect HE is the Luv. Color features were used in the Fuzzy c-means clustering to perform a coarse segmentation. In this stage, HE candidates were identified. Then, features such as mean color in the region and its neighbor pixels, size, perimeter, compactness were used to characterize the candidates. In addition to these

features, the mean response of Gabor filters (108) in 12 orientations and 4 scales were calculated. A total of 124 features characterize a candidate. Feature selection was applied with genetic algorithms, reducing the feature vector to 65 elements. Finally, neural networks was applied to assign a class to the candidates. The algorithm was trained and validated in 150 images and tested in other 150 images (75 with HE). A sensitivity of 93.5% with predictivity of 92.1% was obtained per lesion while sens/spec of 96%/94.6% was obtained per image. Sopharak et al. [177] also used Fuzzy c-means to extract candidates but the authors used more than color information. First, the image was transformed from RGB to HIS color space. Median filtering was applied to the intensity channel to remove noise and CLAHE was used for contrast enhancement. The authors used 4 features per pixel: the intensity after the enhancement, the standard deviation in a window of 15x15 pixels, the value of the Hue channel, and the edge of the image. These features were the input to the Fuzzy c-means algorithm to extract the coarse segmentation. After that, morphological reconstruction was used to obtain a fine segmentation. The authors tested their approach in 40 compressed non-dilated images, obtaining sens/spec of 86%/99%.

In order to improve the detection of hard HE, Sanchez et al. [179] proposed to add contextual information to the set of features. This algorithm includes information of neighboring structures. In addition to add information of the red lesions as in [92], they include information of the vessels. The detection of HE was measured with a fROC curve in 72 images improving from a figure of merit of 0.84 to 0.945.

C. Vessel Abnormalities

1) Venous Beading

Very little work can be found in this topic. One of the first approaches was developed by Gregson et al. [180]. In their approach, thresholding was used to perform a rough segmentation of the vein. Since the vein could present central reflex, holes in the veins were obtained after thresholding. To solve this problem, morphological closing was applied to the rough segmentation. Then, the centerline of the veins was extracted and partitioned in segments of 32 pixels. The diameter was measured in each segment. In addition, a fast Fourier transform was performed in the data to determine the magnitude spectrum of the vein segment diameter. Using this information, a venous beading index was calculated. The objective of the method was separated 51 images in 3 categories: normal, definite and advanced. The results show a statically significance with p-value of 0.005 for class discrimination.

An approach developed by Yang et al. [181] detects venous beading by extracting 13 features of shape curvature. These features were the input to a neural network system. The algorithm was trained/tested in 61 images (32 with venous beading) of 512x512 pixels. A classification rate of 85% was reported.

2) Neovascularization in the optic disc

This was also a topic with few publications. Only two publications that attempt to detect neovascularization in the optic disc are described. The first paper was published by Goatman et al. [104]. In their paper, they divided vessel segments into two classes, abnormal and normal, in order to detect neovascularization of the optic disc. Vessel-like candidate segments in the papilla were detected by using watershed lines and ridge

strength measurements. Fifteen features, such as shape, position, brightness, contrast, and density, were extracted from each candidate. Gaussian-kernel support vector machines (SVM) were used to classify data represented by those features. The results were validated with leave-one-out cross-validation. A total of 38 NVD and 71 normal cases were used to evaluate the performance of their approach. Their method achieved an AUC of 0.79 for the detection of segments with NVD and an AUC of 0.91 for the detection of optic discs with neovascularization.

The second one, developed by Agurto et al. [182], detects NVD by analyzing the vasculature of the optic disc. Properties of tortuosity, width, and density were obtained by analyzing frequency angle information of the amplitude-modulation frequency-modulation (AM-FM) technique, fractal dimension and granulometry. A total of 1048 features were extracted from each image and were processed with linear SVM. The algorithm was tested in 300 images (100 with NVD). A 10-fold was used to validate the algorithm, obtaining an AUC = 0.93.

2.5.7.2 Top-down approaches

One of the first approach, to perform a top-down approach for the detection of DR was the presented by Chaum et al. [183]. The system was based in content-based image retrieval, a process of retrieving related images from large database collections using their pictorial content. In their approach, they detected different structures such as optic disc, vessels, and lesions. Then, features were extracted an stored to create an image index for retrieval.

In the approach present by Agurto et al. [184], different structures were characterized using information of estimates from AM-FM. To do so, the images was divided in regions. These regions could contain any DR pathology, or normal structures. Then, features were extracted to characterize each region. By using k-means, the regions with similar content will be grouped in clusters. Therefore, an image could be represented by a distribution of regions in the different clusters. This distribution will be used as input for a partial least squares classifier. The algorithm was tested in a subset of the MESSIDOR database, achieving an AUC of 0.84 for the detection of DR in any stage and 0.98 for the sight threatening cases which includes high risk DR and high risk of macular edema.

In 2012, an approach based on visual dictionaries in point of interest (PoIs) was presented by Rocha et al. [185]. This is a similar approach to the one presented by Agurto et al. [184]. The authors tried to characterize the pathologies by creating visual words. A visual words is defined as the information extracted from a particular region that could contain HE, MAs or other structures. By using many visual words, a visual dictionary is created. The main difference of this approach with respect to the one presented in [184], is that they do not fixed the position of the ROIs, the authors find the regions to be analyzed in the image (PoIs) with a method called Speeded-up robust features (SURF) [186]. Then each image was represented by a histogram of visual words. This histogram was the feature vector to be input to the classifier. Since the authors tried to detect bright lesions independently of red lesions, a two-class SVM classifier was used. The algorithm was trained with 1014 images (687 normal, 245 with bright lesions, 191 with red lesions, and 109 with both bright and red lesions), and tested with images from the DIARETDB1 and MESSIDOR (risk 1 of DR images were excluded) databases. The algorithm achieved

an AUC=0.89 and AUC=0.72 for detecting bright lesions and red lesions respectively in the MESSIDOR database, and AUC=0.88 and AUC=0.76 for detecting bright and red lesions respectively in the DIARETDB1 database. Although the presented results are lower than previous approaches for the detection of an specific lesion, this method is flexible to detect other lesions; thus it could potentially increase the performance in a DR screening algorithm.

Nowadays global approaches to detect diabetic macular edema have also been published. One of them was developed by Giancardo et al. [187]. This method normalizes the images by combining the shade correction approach and morphological reconstruction. In their method thresholding was applied to detect HE candidates. However, instead of extracting features per candidate, the authors assign scores to each of them using two approaches: Kirsch's operators and stationary wavelets. By thresholding this score, the HE were differentiated. In terms of image classification, the algorithm was tested with the HEI-MED database [188] obtaining an AUC of 0.81 (Wavelets) and 0.86 (Kirsch's operators) in detecting diabetic macular edema. A more recently approach was presented by Deepak et al. [189]. They presented an approach to detect HE in the macula by generating motion patterns in the retinal image. These patterns were generated after inducing motion which was performed by rotating the image at different angles and joined the information. In order to describe the motion pattern, a descriptor derived from the Radon space was used. These features were used in two classifiers: Gaussian data description (Gaussian DD) and principal component analysis data description (PCA DD) obtaining higher results the latter one. The method was tested using 3 databases and to evaluate the performance, 10-fold cross validation was used. For images of HEI-MED

database, the authors obtained a high AUC of 0.99. For MESSIDOR (400 images), an AUC=0.96 was obtained. From the 400 images, a reduced set containing only normals and high risk of macular edema was evaluated obtaining AUC=0.99. A third group images was used to evaluate the algorithm (117 images extracted from DIARETDB0 and DIARETDB1) obtaining AUC=0.96. When all the databases were merged in a whole dataset, the performance of the algorithm decreases obtaining an average AUC of 0.92. In their approach, the authors proposed to determine the severity of macular edema by analyzing the symmetry of the content in the classified images. The hypothesis is a normal macula will have a good degree of symmetry. The algorithm obtained a sens/spec of 100%/81% in differentiate the moderate from the severe cases of macular edema.

2.5.8 Automatic DR screening systems

In this subsection, a summary of the previously published paper with the results of the automatic DR screening systems was presented. In the previous paragraphs, different methodologies were described to address the detection of retinal features such as vasculature, optic disc and fovea location as well as methods to improve the quality of the image and the detection of pathologies. In order to detect multiple lesions, the screening systems generally implement more than one of these algorithms described before.

Currently there are many research centers that have published results on an automatic DR screening system such as the ones presented by Larsen et al. [190], Abramoff et al. [191], Chaum et al.[183], and Fleming et al. [5],[192]. Of these systems, only the one by Chaum et al. [183] has implemented a top-down approach while the other two implemented a bottom-up approach.

In the system developed by the Abramoff et al. [191] at the University of Iowa, algorithms have been implemented to detect image quality, vasculature, optic disc location and two types of abnormalities: red lesions such as microaneurysms (MAs) and hemorrhages; and bright lesions such as HE, CWS and drusen. A total of 15,000 retinal examinations of patients were used to validate the system. Their results showed that individual classifiers performed with a minimum AUC of 0.653 (sens/spec = 0.62/0.60) and a maximum AUC of 0.877 (sens/spec = 0.93/0.60). The authors obtained an AUC of 0.881 (sens/spec = 0.93/0.60).

The screening system developed by Fleming et al. [192] at the University of Aberdeen was applied to 33,535 patients. Their study found that the software could detect 100% of patients with proliferative retinopathy, 100% with referable background retinopathy, 100% with observable background retinopathy, 97.3% with referable maculopathy, and 99.2% with observable maculopathy. The reported specificity of their system was 49.6%, which resulted on a workload reduction of 39.6% of the manual grading.

Chaum et al. [183] at the University of Tennessee implemented an algorithm based on CBIR described previously. The investigators defined, extracted, and tested a large number of region and lesion-based features from a dataset of 395 retinal images. Results showed that the diagnostic sensitivity for all stratified levels of age-related macular degeneration ranged from 75% to 100%. Similarly, the sensitivity of detection for proliferative DR ranged from 0.75 to 0.917 and for non-proliferative DR it ranged from 0.75 to 0.947.

2.6 Discussion

2.6.1 Retinal Image Acquisition

Most of the described methods were focused in developing techniques for detecting structures in fundus images of about 45 degrees of FOV. However, there are two new modalities that were observed in recent conferences of ophthalmology. One is the evaluation of fundus images using low-cost cameras. Although the images taken with these cameras provide sufficient information to assess the eye disease, the quality of these images is lower than the one obtained by current fundus cameras.

The other modality is the use of wide-angle cameras to perform analysis of the retina with a high degree of FOV. The images taken with these cameras have up to 200 degrees of FOV, covering 80% of the retina. A high degree of FOV may prove useful to replace the need to acquire images from different fields. The main advantage of these cameras is that they are suitable for imaging children.

It is important to consider these modalities in order to adapt or implement new algorithms that are capable of processing data collected by these new acquisition settings.

2.6.2 Image Quality Verification

Most of the presented methods achieve a very high accuracy in determining the quality of the images. The ones that are based on vessel segmentation, which are sometimes very time-consuming, can introduce errors if other global image features are not considered. On the other hand, methods that rely on classifiers to build models need a representative sample from the population of retinal images to accurately estimate the quality level of each image. A bad selection of the training set could introduce bias in the predictions.

In addition, it can be noticed that the quality assessment is mainly focused on field 2 images of 45 degrees. Only two papers cover images from fields 1 and 2 [46], [50]. Nowadays, more than one field of view has been used to improve the detection of pathologies, so it is necessary to take into account other retinal areas to obtain a more robust system.

Finally, these methods have tried to match the quality assessment of a retinal specialist. However, an algorithm does not necessarily work the same way as a specialist. For example, there are images extracted for patients with retinal diseases that show very poor quality in some areas, making it difficult for an algorithm to detect pathologies; nonetheless, the human visual perception may be capable of extracting relevant information from them, making it possible for a grader to assign an acceptable quality to those images.

2.6.3 Pre-processing methods for fundus images

As it has already been pointed out, the methods for pre-processing can be general or specific depending of the application. Large-scale retinal screening is expected to become standard in the following years. Therefore, many cameras with different settings will be distributed in many regions. This may require methods for normalization of images to help obtain accurate results in DR detection.

In addition, we expect that as large scale screening approaches are developed, non-dilated fundus images and images captured with low-cost cameras are acquired by these approaches. Moreover, telemedicine applications require compression to reduce

bandwidth costs. Therefore, the overall quality of these images will be lower than nowadays.

Another thing to consider is to develop adaptive methods modeled to enhance a subset of images, since sometimes good quality images get worse after enhancement. Alternatively, different levels of enhancement could be applied to different areas of the images as it has been proposed in [182]. Another alternative that needs to be further studied is the one described in [166], where an optimal combination of pre-processing methods in found.

2.6.4 Retinal Vasculature Segmentation

Many methods have been developed for this step; they have also been tested in similar databases allowing a comparison between them. As it can be observed in Table 2.2, recent methods achieved similar performance in terms of AUC and/or accuracy; as a consequence, processing time is also analyzed. In addition, the online databases have a small number of images, making it difficult for generalization. The problem is that getting the ground truth is a very demanding task that cannot be afforded. A solution would be to apply a proposed methodology to the different databases with different resolutions, compression, and pathologies in order to evaluate its robustness.

2.6.5 Optic disc Localization and Segmentation

There are some methods for the detection of the optic disc which estimate its center by locating the convergence point of the blood vessels. Although this point is inside the OD, it is not necessarily located at its center. If that is the case, a wrong estimation of the area

occupied by the OD may lead to its incomplete removal. In the case of DR pathology detection, this would allow the bright part of the optic disc to be processed, thus affecting the detection of lesions. This problem can be solved by using segmentation algorithms, which provide an accurate estimation of the OD at the expense of an increment in processing time. However, the current methods based on techniques like level set methods may be affected by other structures near the optic disc boundary such as pathologies or artifacts.

2.6.6 Localization of the Macula and Fovea

As it has been shown in section 2.5, algorithms to detect sight threatening conditions have been developed. The purpose for their development is to achieve high sensitivity to detect those cases in retinal screening. One of these conditions is diabetic macular edema. To detect this disease, HE need to be found in the macula area; thus the fovea has to be located correctly. Methods to locate the macula are usually embedded in the approaches to detect diabetic macular edema.

Methods based on intensity only will not achieve good detection accuracy when the image is abnormal and it has lesions than can mask the fovea location. Higher sensitivity is expected when other features such as position of structures in the retina are considered for the analysis. However these methods may take more processing time. The trade-off of the complexity of these methods with the variation in the detection results should be analyzed.

2.6.7 Localization and Segmentation of DR pathologies

In the last years, the use of angiograms to detect MAs has been avoided in automatic systems. This is because a study in [193] has shown that intravenous use of fluorescein has a mortality of 1:222000, making the process not suitable for large-scale screening purposes as it has been pointed out by [92].

It can also be observed that recent approaches use more images to validate their results. In addition, more than one reader is used to grade the images. These two facts will help these approaches mimic the conditions of a retinal screening process.

In general, the performance of the algorithms to detect pathologies in the retina has improved over time. High detection rates are reported especially in cases of advanced DR. In addition, we can find in the literature that the new tendency is the implementation of top-down approaches since they can cover a high variety of abnormalities in the retina and do not require images to be manually labeled for the algorithms to be trained. However, they need a large dataset to be able to characterize the different diseases.

Lately the groups are more focused in increasing the detection rate of pathologies associated with sight threatening conditions in DR such as neovascularization, and diabetic macular edema. By incorporating these algorithms in the current DR screening systems, a better detection of DR is expected.

Finally, large databases with a better sample of the population of diabetics such as racial and ethnicity diversity is necessary to validate the proposed algorithms. Those that achieve good results on these databases could potentially be applied on a clinical setting, allowing cost-effective early detection of DR in millions of people with diabetes [194].

2.6.8 Automatic DR screening systems

A recent publication shows that method for detection of DR based on CBIR developed by Quellec et al. [195] can be used as a second opinion in the grading, thus helping inexperienced graders. This study was based on 1176 multimodal eye fundus photographs. Cohen's kappa was used to compare the performance of the algorithm with a 2-year experience grader. The ground truth was made by a 7-year experience grader, obtaining a slightly better agreement with the algorithm results.

As it was pointed out, a general automatic DR screening system may use more than one of the described modules to detect DR. We also know that each module will introduce some error to the classification. We think that it would be interesting to see studies of how the accuracy in one module could affect the general performance of the system, since they are usually implemented sequentially.

In the previous section, we showed that there are a few groups that have already tested their DR screening systems in a large population. These results are very encouraging since a high sensitivity is obtained for PDR cases and good sensitivity is obtained for NPDR cases. This demonstrates that in a near future the assessment of DR could be performed in a semi-automatic implementation.

Chapter 3: Classification of Diabetic Retinopathy using Multi-Scale AM-FM Analysis Methods

Abstract

This chapter describes the characterization of pathologies in diabetic retinopathy by means of multi-scale AM-FM methods and presents the results of the algorithm developed to classify DR. In section 3.1, a detailed analysis of the most common DR pathologies such as: microaneurysms, hemorrhages, exudates and neovascularization using AM-FM is presented. This work has been published in [184]. Section 3.2 is an extension of the work presented in Section 3.2. Here, the detection of the most advance DR pathologies as well as AMD pathologies is performed and evaluated obtaining high performance [196].

3.1 Discrimination of pathologies using amplitude-modulation frequency-modulation

3.1.1 Database

Images were selected from the online Early Treatment Diabetic Retinopathy Study (ETDRS) database [197]. Working images are uncompressed TIF format with a size of 1000 by 1060 pixels. The ETDRS standard photographs contain 15 stereo pair images that are used to train graders on diabetic retinopathy. From these images, 120 regions of 40x40 pixels containing retinal structures of interest were selected for this study. These regions were grouped into 6 categories of 20 regions per structure: microaneurysms,

hemorrhages, exudates, neovascularization, retinal background, and vessels. Fig. 3.1a shows one of the standard ETDRS images used with abnormal retinal structures delimited by boxes. Fig. 3.1b shows samples of the structures mentioned above on regions of interest (ROI) of 40x40 pixels in size.
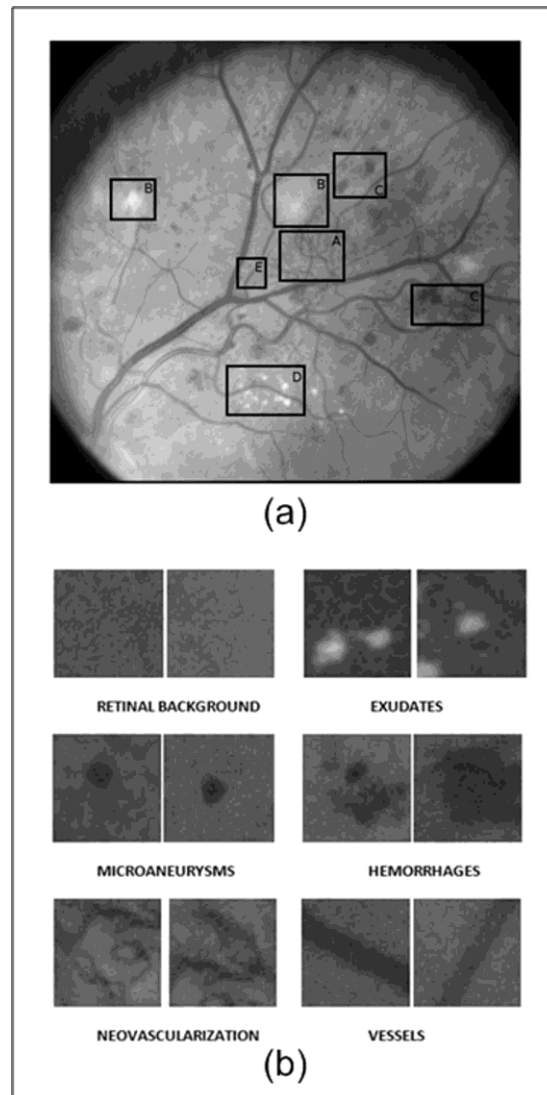
Figure 3.1 (a) Image from the ETDRS standard database. Lesions encased in the boxes are examples of A) Neovascularization, B) Cottonwool spots, C) Hemorrhages, D) Exudates, and E) Microaneurysms; (b) Examples of retinal structures on ROIs of 40 x 40 pixels.

3.1.2 AM-FM Decompositions

An image can be approximated by a sum of AM-FM components given by

$$I(x, y) \approx \sum_{n=1}^{M} a_n(x, y) \cos \varphi_n(x, y) \qquad (3.1)$$

where M is the number of AM-FM components, $a_n(x, y)$ denote instantaneous amplitude functions (IA) and $\varphi_n(x, y)$ denote the instantaneous phase functions [198]. We refer to [199] for further details on the use of AM-FM decomposition. Here, our focus will be on the extraction of AM-FM texture features.

First, we extract AM-FM components from each image scale. For each AM-FM component, the instantaneous frequency (IF) is defined in terms of the gradient of the phase φ_n:

$$\nabla \varphi_n(x, y) = \left(\frac{\partial \varphi_n(x, y)}{\partial x}, \frac{\partial \varphi_n(x, y)}{\partial y} \right). \qquad (3.2)$$

In terms of extracting textural features from each component, we are interested in using the instantaneous frequency (IF) and the instantaneous amplitude (IA). Conceptually, the IF measures local frequency content. When expressed in terms of cycles per mm, the IF magnitude is independent of any image rotations or retinal imaging hardware characteristics since it reflects an actual physical measurement of local image texture, extracted from each image scale. Furthermore, the IF magnitude is a measurement of the geometry of the texture, with a strong degree of independence from contrast and non-uniform illumination variations.

We are also interested in working with an invariant IF angle feature. To this end, instead of using the actual IF angle, we use relative angles. Here, relative angles are estimated locally as deviations from the dominant neighborhood angle. Thus, directional structures, such as blood vessels will produce a relative angle distribution concentrated around zero. We constraint the relative angle to range from -π/2 to π/2. Thus, a sign

ambiguity occurs from the fact that $\cos \varphi(x, y)$ represents the same image as $\cos[-\varphi(x, y)]$.

Local image intensity variations, including edges, are reflected in the IA. As we shall discuss next, large spatial scale variations will be reflected in the low-frequency scales.

3.1.3 Frequency Scales and Filterbanks

AM-FM components are extracted from different image scales. We consider the use of 25 bandpass channel filters associated with four frequency scales and nine possible Combinations of Scales (CoS) (see Fig. 3.2). We estimate a single AM-FM component over each combination of scales using Dominant Component Analysis [1].
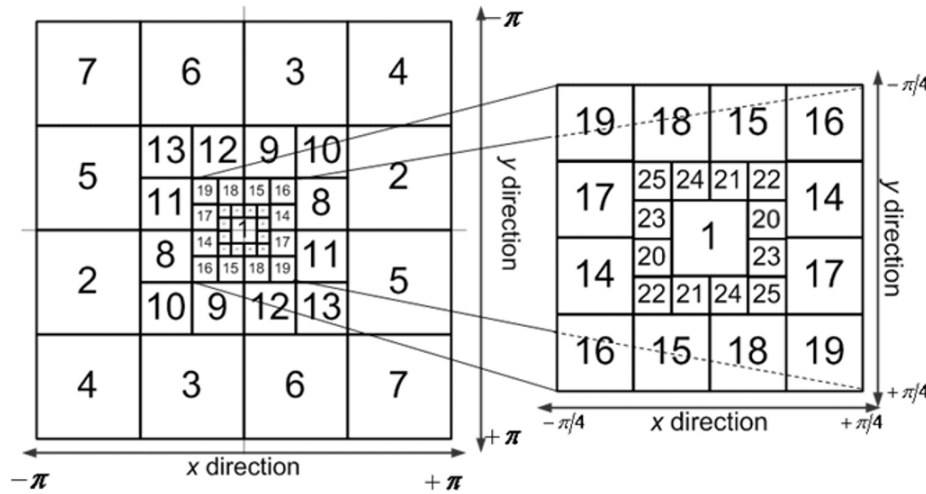
Figure 3.2 Filterbank for Multi-Scale AM-FM Decomposition. The discrete-spectrum is decomposed using 25 bandpass filters. Each scale (see Table 3.1).

At lower frequency scales, the magnitude values of the |IF| are small and the extracted AM-FM features reflect slowly-varying image texture. For example, the most appropriate scale for blood vessels is the one that captures frequencies with a period that is

proportional to their width. On the other hand, the fine details within individual lesions, such as the small vessels in neovascular structures, are captured by the higher-frequency scales. To analyze the image at different scales, we use a multi-scale channel decomposition outlined in Fig. 3.2.

The use of different scales also considers the size variability among structures such as MAs, exudates, hemorrhages, etc. A predominant characteristic of patients with diabetic retinopathy is that the lesion sizes will vary. Dark lesions such as MAs, or bright lesions such as exudates may be present in an image as structures with areas on the order of a few pixels. In the images that were analyzed for this study, the MAs' and exudates' diameters are on the order of 8 pixels, which represent a size 0.04 mm. Hemorrhages and cotton wool spots diameters are on the order of 25 pixels, representing a size of 0.12 mm. Multiple scales are used to capture these features of different sizes. The different filters (within any given scale) also consider the orientation of the feature being encoded.

Table 3.1 relates the number of pixels and the frequency ranges of each band-pass filter shown in Fig. 3.2. The combinations of scales were grouped in such a way that contiguous frequency bands were covered. In this way, structures that only appear in a specific frequency range or appear between two or three contiguous bands can also be described. For this reason, the nine combinations of scales (CoS), given in Table 3.2, were grouped to encode the features for different structures.

Twenty-seven AM-FM histogram estimates were computed corresponding to the three AM-FM features IA, |IF|, and relative angle, for each of the nine combinations of scales. Fig 3.3-3.5 shows some examples of the AM-FM estimates obtained after applying AM-FM to three of the images in the ETDRS dataset.

Table 3.1 Band Pass Filters Associated with multiple image scales.

Frequency Scale Band	Filters	Instantaneous Wavelength (period)	Range in mm
Low Pass Filter (LPF)	1	22.6 to ∞	0.226 to ∞
Very Low Frequencies (VL)	20-25	11.3 to 32	0.113 to 0.32
Low Frequencies (L)	14-19	5.7 to 16	0.057 to 0.16
Medium Frequencies (M)	8-13	2.8 to 8	0.028 to 0.08
High Frequencies (H)	2-7	1.4 to 4	0.014 to 0.04

Table 3.2 Combination of Scales

Combination Number	Filters	Frequency Bands	Range in cycles/mm
1	8:25	M + L + VL	0.028 to 0.32
2	1	LPF	0.226 to ∞
3	20:25	VL	0.113 to 0.32
4	14:19	L	0.057 to 0.16
5	8:13	M	0.028 to 0.08
6	14:25	L + VL	0.057 to 0.32
7	8:19	M + L	0.028 to 0.16
8	2:7	H	0.014 to 0.04
9	2:13	H+M	0.014 to 0.08
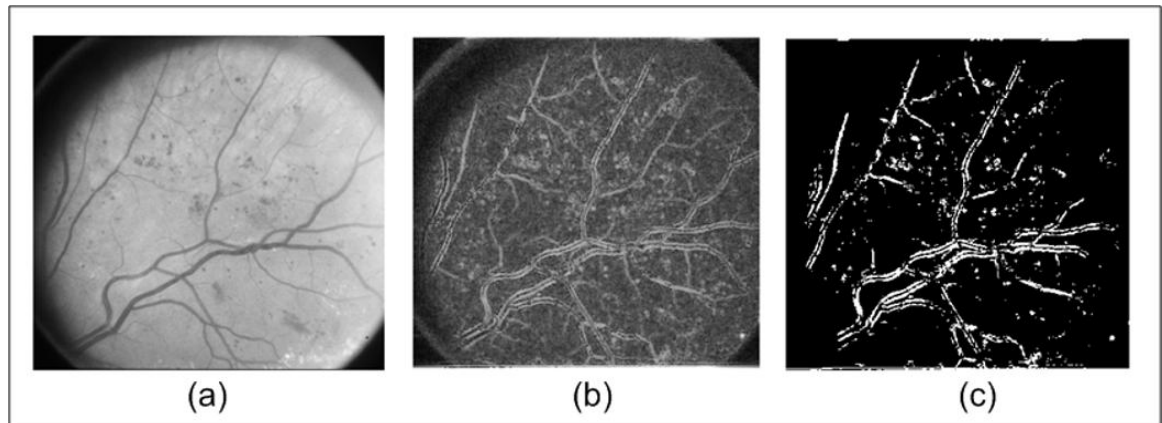
Figure 3.3 (a) Original Image from ETDRS; (b) Instantaneous Amplitude using medium, low and very low frequencies; and (c) Thresholded Image of (b).
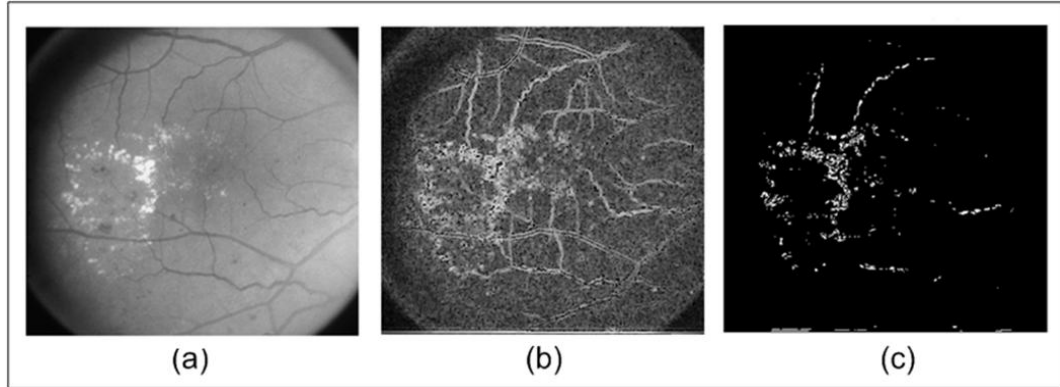
Figure 3.4 (a) Original Image from ETDRS; (b) Instantaneous Amplitude using low frequencies; and (c) Thresholded Image of (b).
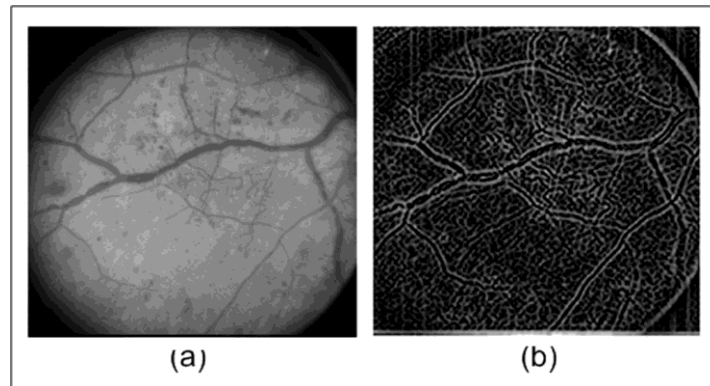
Figure 3.5 (a) Original Image from ETDRS; (b) Instantaneous Frequency Magnitude using low pass filter.

3.1.4 Encoding of structures using AM-FM

To characterize the retinal structures the cumulative distribution functions (CDF) of the IA, |IF|, and the relative angle are used. Since the range of values of each estimate varies according the CoS used, the histograms (or pdf) are computed from the global minimum value to the global maximum value. For example, for the IA using CoS 4 (low frequencies), the histograms were computed in the range of [0 72] pixels because this is the grayscale range for the IA in which the low frequencies are supported.

A region with small pixel intensity variation will also be characterized by low IA values in the higher frequency scales. This is due to the fact that low intensity variation

regions will also contain weak frequency components. Furthermore, darker regions will also be characterized by low IA values in the lower frequency scales. This is due to the linearity of the AM-FM decomposition. Low amplitude image regions will mostly need low-amplitude AM-FM components. For example, retinal background (see Fig. 3.1b) analyzed in the whole frequency spectrum will have roughly constant, low IA values. In general, for any given scale, low IA values will reflect the fact that frequency components from that particular scale are not contained in the image. Thus, since there are no high IA values to account for, the CDF of this kind of structure is expected to rise rapidly for low IA values. On the other hand, if a region contains structures with significant edges and intensity variations such as vessels, microaneurysms, neovascularization, or exudates, we expect that the rate of rise (pdf) of their CDFs will be slower due to the presence of both low and high IA components.

3.1.5 Defining Retinal Characteristics of AM-FM Feature Vectors

Here, we describe how the AM-FM estimates encode structures and how this encoding can be related to the creation of relevant feature vectors for the detection of the analyzed lesions. The instantaneous frequency magnitude ($|IF|$) is insensitive to the direction of image intensity variations. Furthermore, the IF magnitude is a function of the local geometry as opposed to the slowly-varying brightness variations captured in the IA. Thus, a single dark round structure in a lighter background will have similar $|IF|$ distribution as a single bright round structure of the same size in darker region. This is roughly the case for exudates (bright lesions) and microaneurysms (dark lesions) when they have similar areas.

|IF| estimates can be used for differentiating between two regions where one has a single vessel (as in a normal retinal vessel) and a second region that has multiple narrow vessels (as in neovascularization). Even though both regions may have information in the same frequency ranges, the counts on the histogram of the latter region will be greater. The larger histogram counts reflect the fact that a larger number of pixels exhibit these frequency components. The histogram for a region with neovascularization will have higher kurtosis (a more pronounced peak) than a region containing just one vessel.

We also analyze image regions in terms of the relative IF angle. First, we note that image structures without any dominant orientation will have a relatively flat histogram (regardless of what is chosen as the dominant orientation). This kind of feature should be observed on structures such as microaneurysms and exudates. Conversely, an area with a single vessel in a region has a unique angle of inclination. In this case, the (non-relative) IF angle estimate is expected to be highly peaked at the inclination angle, assigning much smaller count values to angles that are further away from the angle of inclination. Then, as discussed earlier, the relative angle histograms will have their peak at zero. One last case includes structures within a region which have several elements with different orientations, such as neovascularization. The histograms for these regions would include several well-defined peaks at different angles. Thus, this feature can be differentiated from the other two well-defined distributions described above.

3.1.6 Classification

In order to demonstrate that the methodology presented in this work can distinguish between the structures in the retina, we classify small regions containing structures. To

test this classification, a well known statistical metric, the Mahalanobis distance, is computed. Fig. 3.6 shows the procedure to calculate the distance between the lesions for each of the 9 CoS. First, the cumulative distribution function (CDF) is extracted for each of the 3 estimates in the 120 regions. After that, the dimensionality of the feature vectors is reduced using Principal Component Analysis (PCA), where the principal component projections are chosen so as to account for 95% of the variance. This procedure is applied for each of the 9 combinations of scales. In this way, the combinations and the estimates that produce the greatest distance between lesions can be found. It is important to mention that in order to normalize the calculation of the distance between lesions, the reduced matrix is adjusted to have standard deviation 1 and the distances of the lesions with respect to a specific lesion are calculated between mean vectors.

Table 3.3 Database Information

DR RISK	Number of Images	Number of MA	Number of Hemorrhages	Neovascularization
RISK 0	140	0	0	0
RISK 1	28	[1, 5]	0	0
RISK 2	68	<5,15>	[0, 5]	0
RISK 3	140	[15, ∞>	[5, ∞>	1

Any of the three conditions for the number of hemorrhages or the number of microaneurysms should be held to consider the image as RISK 2 and Risk 3. Some of the retinal images of Risk2 present exudates and some of the retinal images of Risk3 present exudates, and neovascularization. Macular edema was graded separately as either none, >1DD from fovea or <1DD from fovea (clinically significant Macular edema, CSME).
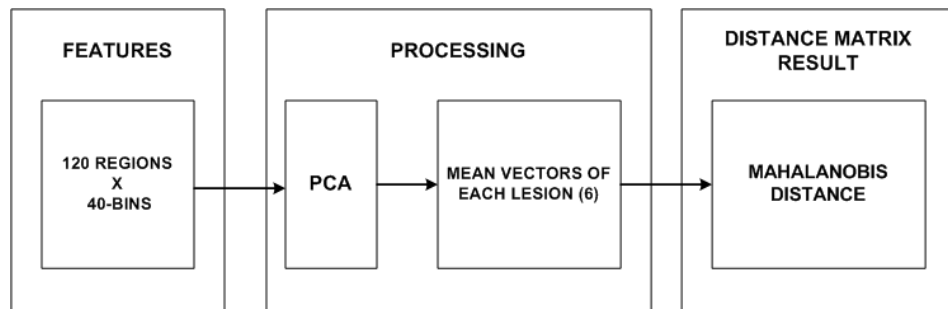
Figure 3.6 Procedure to find the Mahalanobis distance between lesions for each estimate and each CoS.

3.1.7 Results

This section presents the results of an exhaustive analysis using multi-scale AM-FM for the purposes of characterizing retinal structures and for classifying different types of lesions. As we have discussed in the previous section, the various retinal structures are encoded differently by the AM-FM features. Furthermore, we use frequency scales and filterbanks to focus on the various size structures and to eliminate noise introduced by other less meaningful structures that are present in the image.

Using the methodology previously described, the Mahalanobis distance values between features for each of the 3 estimates (IA, |IF|, and relative angle) and the 9 combinations of scales (Table 3.2) are found. Tables 3.4 and 3.5 show the maximum distance values and the corresponding estimate and combination found per lesion pair. For example, the maximum distance between hemorrhages and microaneurysms is 4.71 standard deviations and is given by the instantaneous amplitude combination of scales #2 (IA-2 on Table 3.5). Distances among the features range from 2.65 to 8.18 standard deviations, meaning that if we would use just this distance to classify the images we would have accuracies between 92% and >99.99%.

Table 3.4 Maximum Distance Matrix Between Lesions

Retinal Structures	RB	EX	MA	HE	NV
EX	6.87	0	-	-	-
MA	3.48	3.97	0	-	-
HE	4.72	4.89	4.71	0	-
NV	8.18	4.59	2.92	2.65	0
VE	6.14	3.31	2.83	3.51	3.35

RB: Retinal Background, EX: Exudate, MA: Microaneurysm, HE: Hemorrhage
NV: Neovascularization, VE: Vessel

Table 3.5 Combination of scales (see Table 2) For The Maximum
Distances between lesions

Retinal Structures	RB	EX	MA	HE	NV
EX	|IF| - 7	-	-	-	-
MA	|IF| - 6	IA -9	-	-	-
HE	|IF| - 2	IA- 1	IA- 2	-	-
NV	IA – 1	IA- 1	IA-5	IA-1	-
VE	|IF| - 2	θ - 1	θ - 1	θ - 1	|IF| - 1

Most structures have their largest Mahalanobis distance from retinal background when using the |IF| features. Regions composed of only retinal background will have a histogram in most scales that reflects its high frequency, random pixel brightness structure. Because vessels and the neovascularization (NV) appear to have a predominant orientation in the IF, the relative IF angle can be used for differentiating vessels from microaneurysms (Fig. 3.8b), exudates, and hemorrhages. It can also be seen that in the case of the NV vs. vessels, the |IF| features are the most appropriate. This happens since the IA content may reflect similar information while the NV frequency components will vary significantly from components associated with a normal vessel. The regions with NV could also be differentiated using the angle estimation. This is the case for the classification between NV and hemorrhages (Fig. 3.11b).

For differentiating between NV vs retinal background and microaneurysms, the IA works best. From the results shown on Table 3.4, we see that the lowest Mahalanobis is between NV and HE. The distance obtained in our analysis is of 2.65 standard deviations. However, the distance between NV and retinal background is 8.18. From a clinical perspective it is critically important to be able to isolate regions in the retina presenting with the high risk lesions, such as NV. Our results imply that NV will be classified or differentiated from the retinal background with greater than 99.99%

accuracy and in the worst case with 92% of accuracy (NV vs. HE).

Clinically significant macular edema (CSME) appears in an advanced stage of DR. Hard exudates that appears near to the fovea (1 disc diameter centered in the fovea) are considered to be surrogates of CSME. In this study, we show the exudates (Table 3.4) were easily differentiated from regions of retinal background (d=6.87) using the |IF| with Cos = 7. None of the other structures studied gave distances that are less than d=3.31. IA provides the greatest distances to other structures except for the distance from exudates to retinal background. It can be observed that the maximum distance between exudates and microaneurysms are obtained using the IA's extracted from medium and high frequencies. This occurs since the microaneurysms have a smaller size than the exudates, and are thus characterized by higher frequencies.

For vessels, the relative angle and the |IF| provide relevant features for the discrimination of vessels from the rest of structures. The lower, medium and higher frequencies are all involved in this characterization. This range of frequencies varies depending on the size of the element to which the vessels are compared. It is important to mention that in many MA segmentation studies, algorithms are often confounded by normal vessels segments and hemorrhages. For that reason it is not surprising that although MAs are easily differentiated from retinal background (d=3.48), they are found to be similar, as measured by the Mahalanobis distance, to neovascularization and normal retinal vessels (d = 2.83 and d = 2.92, respectively).

Using the results shown in Tables 3.4 and 3.5, we can determine which CoS and which estimate provided that most relevant features for a particular comparison. These results are of great importance for our AM-FM algorithm since they allow us to pinpoint

which are the features and CoS needed to separate the retinal structures. Knowing the relevant CoS, this step will reduce the numbers of features to be extracted. In addition to the Mahalanobis results that presents meaningful distance between CDFs of structures for all the CoS, the K-S test demonstrated that almost all the Cos and estimates provide useful information for the characterization of structures. Table 3.6 shows that all CoS (from 1 to 9) between the three estimates are specified as relevant information for the classification. It can also be observed that the pair of structures in which the vessels are presented except vessels vs. neovascularization, the angle estimation helps in the discrimination of structures.

Finally, Table 3.7 presents a statistical analysis in percentiles for the most relevant estimates. It can be observed that for the IA-CoS 2, the hemorrhage presents values that are different from the rest of structures. This CoS is adequate for large structures (> 0.226 mm) since the lower frequencies are supported by it. Using the medium frequencies (CoS 5) we notice that exudates and neovascularization are clearly distinguished from the retinal background while the microaneurysms present similar values than the retinal background. This occurs since the medium frequencies capture structures comparable to exudates, the width of the neovascularization and the smallest structures such microaneurysms which are call captured in high frequencies.

The following figures show the comparison of the mean of the CDFs between some of the pairs of structures from the list in Tables 3.4 and 3.5. The selected pairs include structures for which the majority of classification algorithms have problems distinguishing between them. In Fig. 3.10 and Fig. 3.11 neovascularization samples are compared with 3 different types of structures. This multiple comparison is presented due

to the importance of neovascularization, indicative of an advanced stage of DR. The common problem in the detection of the neovascularization is that this type of lesion may have visually similar structures to hemorrhages and vessels, and therefore similar analytical features which have previously produced inaccurate results using other image processing methods. In Fig. 3.11 the neovascularization is compared with a hemorrhage using 2 different AM-FM estimates.

Table 3.6 Relevant Scales of the AM-FM Estimates using K-S Test

Pair of Structures	Instantaneous Amplitude Scales	Instantaneous Frequency Magnitude Scales	Relative Angle Scales
RB, EX	1,3,4,5,6,7	1,3,4,5,6,7	5
RB, MA	4,6,7,	4,6,7	
RB, HE	2,3,4,6,7	3,4,6,7	2
RB, NV	1,3,4,5,6,7	1,4,5,6,7	
RB, VE	1,4,6,7	1,4,6,7	1,7
EX, MA	1,4,5,6,7	5,9	5
EX, HE	1,2,3,4,5,6,7	4,5,6	2
EX, NV	1,4,6,7	4,6	
EX, VE	1,2,4,5,6,7,8,9	2,7	2
MA, HE	1,2,4,6,7	2	2
MA, NV	1,4,5,6,7	1,7,9	
MA, VE	1,2,4,6,7	1,2,4,6	1,7
HE, NV	1,3,4,5,6,7,9	1,3,4,5,7,9	3
HE, VE	1,4,6,7	4,6	
NV, VE	1,3,4,5,6,7,8,9	1,2,4,6,7	

RB: Retinal Background, EX: Exudate, MA: Microaneurysm, HE: Hemorrhage, NV: Neovascularization, VE: Vessel

Table 3.7 Percentiles Of The Distributions For Each Structure

Retinal Structures	Retinal Background			Exudates			Microaneurysms		
Percentiles									
Estimates	25	50	75	25	50	75	25	50	75
IA CoS 2	169.30	172.38	175.30	145.95	163.28	182.77	162.69	169.07	174.11
IA CoS 4	2.47	3.19	4.08	6.84	10.97	16.10	3.15	4.56	7.28
IA CoS 5	2.03	2.58	3.21	3.19	4.55	6.23	2.16	2.79	3.59
|IF| CoS 2 (cycles/mm)	0.03	0.56	0.93	0.12	1.29	2.22	0.11	0.93	1.53
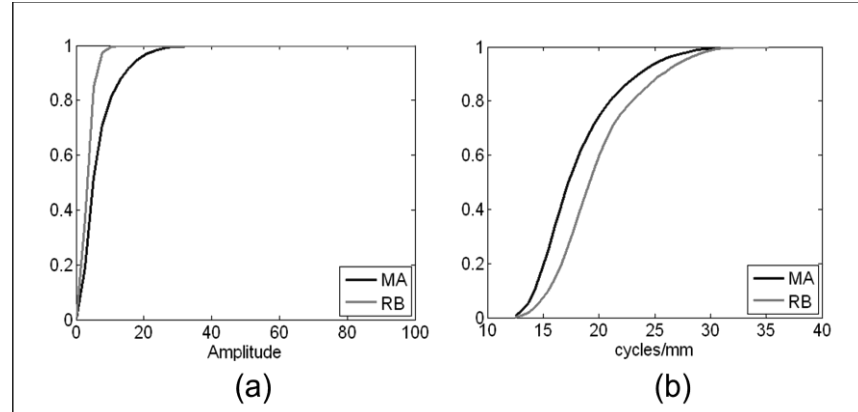
Figure 3.7 Comparison of the mean of the CDFs between Microaneurysm (MA) and Retinal Background (RB). (a) CDFs of the IA for low and very low frequencies, (b) CDFs of the |IF| for low and very low frequencies.
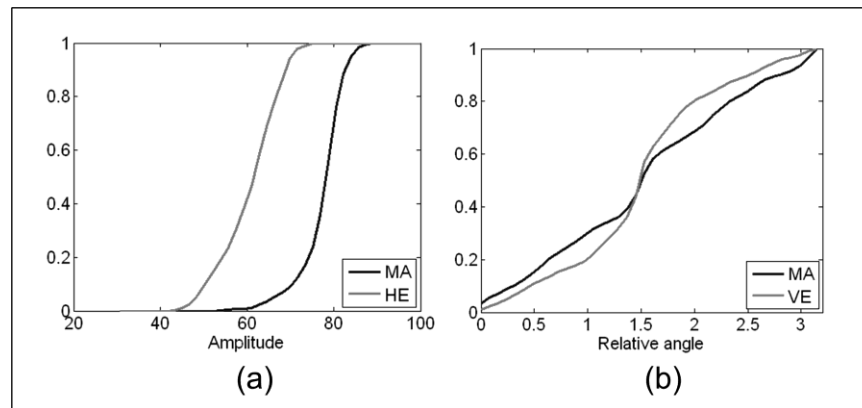
Figure 3.8 (a)Comparison of the mean of the IA CDFs between Microaneurysm (MA) and Hemorrhage (HE) for the low pass filter, (b) Comparison of the mean of the angle CDFs between Microaneurysm (MA) and Vessels (VE) for medium, low and very low frequencies.
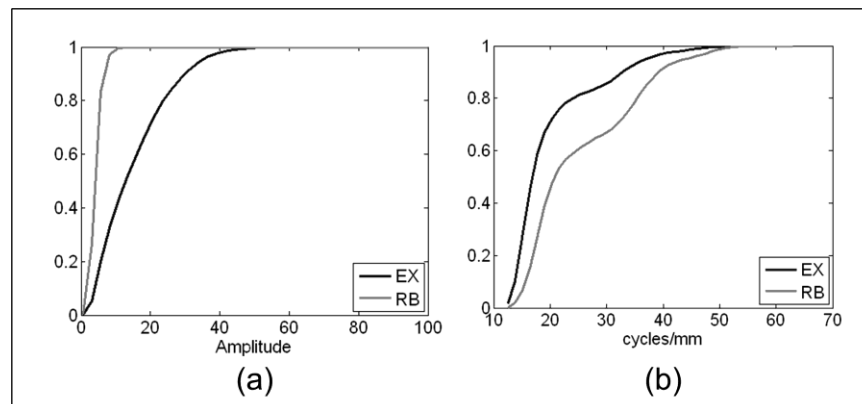
Figure 3.9 Comparison of the mean of the CDFs between Exudates (EX) and Retinal Background (RB). (a) CDFs of the IA for medium and low frequencies, (b) CDFs of the |IF| for medium and low frequencies,
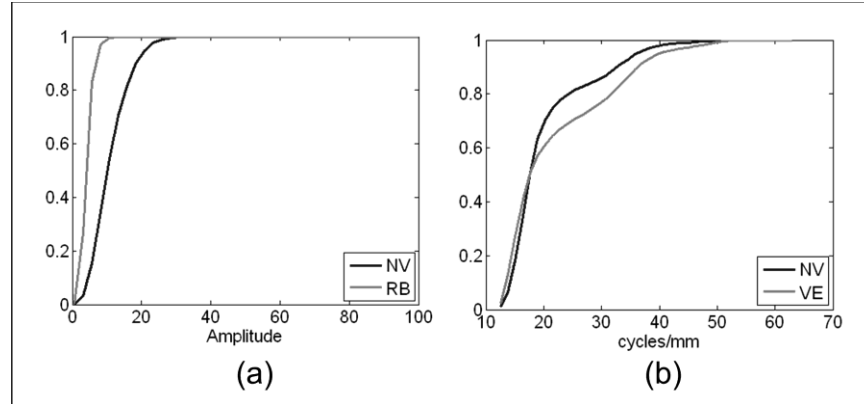
Figure 3.10 (a)Comparison of the mean of the IA CDFs between Neovascularization (NV) and Retinal Background(RB) for medium, low and very low frequencies, (b) Comparison of the mean of the |IF| CDFs between Neovascularization (NV) and Vessels (VE) for medium, low and very low frequencies.
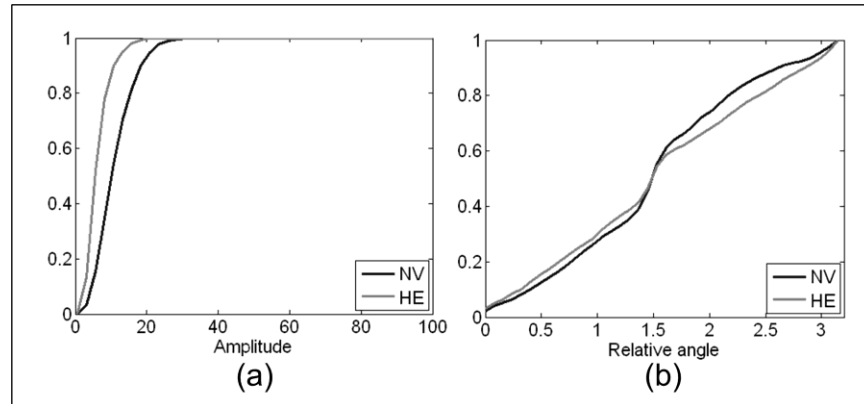
Figure 3.11 Comparison of the mean of the CDFs between Neovascularization (NV) and Hemorrhage (HE). (a) CDFs of the IA for medium, low and very low frequencies, (b) CDFs of the □ for low frequencies.

The characteristics of the AM-FM feature vectors that produced the distance table are given in Figs. 3.7 through 3.11.

A. Microaneurysms

Fig. 3.7 compares MAs and retinal background using |IF| and IA for the combined L+VL frequency bands. The ROI that contains the MA displays a distribution of the |IF| that is shifted to the smaller magnitudes with respect to those of the retinal background for the low (L) and very low (VL) frequency bands (see Fig. 3.7b). The retinal

background, because of its near homogeneous gray level, presents a CDF for IA that rises sharply to 1, while the ROI with the MA will have a slower rise in the CDF or a broader distribution of the IA histogram (see Fig 3.7b). These differences are quantified in Table 3.4, where a Mahalanobis distance of 3.48 is observed.

Fig. 3.8 presents the CDFs for ROIs with MAs and hemorrhages (3.8a) and for MAs and retinal vessels (3.8b). To differentiate MAs from hemorrhages IA from the lowest (LPF) frequency band gave the greatest Mahalanobis distance. This comes from the fact that hemorrhages exhibit strong low-frequency components due to their larger size. In comparison, ROIs with an MA were characterized by weaker low-frequency components, as seen by the faster rise in the IA CDF for MAs. MAs and retinal vessels are easily differentiated by the CDF of the relative IF angle. While MA angles are more evenly distributed, the retinal vessels clearly show a dominant orientation, as seen by the sharp rise at the central bin (~20) in the CDF for retinal vessels in Fig. 3.8b.

B. Exudates

The maximum Mahalanobis distance for differentiating exudates from the retinal background (6.87 standard deviations) was given by the |IF| for medium (M) and low (L) frequency bands. This large distance between the two groups occurs mainly due to the fact that the retinal background is characterized by weaker medium and lower frequency content, while exudates have stronger components due to their well-defined size characteristics. Fig. 3.9 presents the CDFs for |IF| and IA. As with the MAs, detecting ROIs with exudates is facilitated by the broader distribution of the IA histogram as compared to the histograms for the retinal background.

C. Neovascularization

In Figs. 3.10a and 3.10b and Figs. 3.11a and 3.11b, the neovascularization is compared with the CDF for retinal background, retinal vessels, and hemorrhages, respectively. Table 3.4 shows Mahalanobis distances between neovascular abnormalities and retinal background, retina vessels, MAs, and hemorrhages as 8.18, 6.14, 2.92, and 2.65 standard deviations, respectively. This indicates a high probability of differentiation between neovascularization and these other structures. The identifiable CDF of the ROIs with only retinal background is easily differentiated from ROIs with neovascular abnormalities through the IA CDF (Fig. 3.10a) for the M+L+VL frequency band. |IF| was used to differentiate neovascularization from normal retinal vessels. Fig. 3.10b shows the CDFs for the two types of structures using the M+L+VL frequency bands.

In Figs 3.11a and 3.11b, IA and |IF| are presented to illustrate that it is IA that gives the greatest contribution to the Mahalanobis distance between these two types of structures.

D. Hemorrhages

Large structures like hemorrhages have their stronger AM-FM components in the lower frequencies. For this reason, combinations of scales with low frequencies are necessary to detect this kind of structure. Fig. 3.8a shows the comparison of the CDFs of the hemorrhages vs. the microaneurysms. It can be appreciated in the figure that the difference between both structures is large. On the other hand, when we use scales with that incorporate higher frequencies, the content of the hemorrhages cannot be detected

completely. Fig 3.11a shows the comparison of the hemorrhage vs. neovascularization for CoS 1. From this figure, it is clear that the instantaneous amplitude for the hemorrhage is concentrated near zero, implying weaker components for the hemorrhages, as opposed to neovascularization that has stronger components in the medium and higher frequencies.

E. Vessels

This structure can be differentiated using relative-angle estimates because it presents a well defined geometrical orientation. Fig 3.8b is a clear example of the expected shape for the vessels in which the CDF rises sharply at the center, as explained earlier.

As it can be seen in these plots of the CDF's, strong differences can be seen between different structures. To assess the significance of these features for the classification, the Kolmogorov-Smirnov (K-S) test was applied for each pair of structures. In this analysis each bin of the CDF of the structures is extracted. Since there are 20 regions per structure, each bin has a distribution with 20 elements. In this way, a meticulous analysis is performed to assess the relevance of the bins in our feature vector. Table 3.6 shows the combination of scales that produced a significant difference between the structures pairs when using the K-S test. It can be observed that most of the CoS of the three estimates, specially the IA, contributed relevant information in the characterization of the DR lesions.

In addition to the previous analysis, the statistics for the distribution of the most relevant features for the classification are presented in Tables 3.6 and 3.7. These statistics were calculated with the pixel information for each of the 120 regions in our analysis. Table 3.6 and Table 3.7 present the median and the 25 and 75 percentiles are presented

for each of the 6 structures described before. These three quartiles are used to compare the population of all the CDFs for each structure.

3.1.8 Conclusions

The previous analysis show by the first time that AM-FM has been used with a multiscale decomposition of retinal structures for the purposes of classifying them into pathological and normal structures. The results demonstrate a significant capability to differentiate between retinal features, such as normal anatomy (retinal background and retinal vessels), from pathological structures (neovascularization, microaneurysms, hemorrhages, and exudates). The histograms for regions of interest containing these structures yield a signature through the CDF that can be used to successfully differentiate these structures as summarized in Table 3.6.

3.2 Clasification of Diabetic Retinopathy and Macular Edema using AM-FM

In previous publications [200], [201], [202],the feasibility of AM-FM to capture pathologies in retinal images has been demonstrated. In an attempt to further improve the algorithm described in [184], some modifications have been implemented on it in order to be able to capture more pathologies thus more eye diseases. In a previous publication [203], an available online database were used to test the algorithm, obtaining as a result an average AUC of 0.80 for 1200 images. The current algorithm, which is described in this section, can be found in [204].

3.2.1 Data Description

The retrospective images used to test our algorithm were obtained from the Retina Institute of South Texas (RIST, San Antonio, TX) and the University of Texas Health Science Center in San Antonio (UTHSCSA). Fundus images from 822 patients (378 and 444 patients from RIST and UTHSCSA, respectively) were collected retrospectively for this study. The images were taken using a Topcon camera at RIST and a Canon CF-60uv at UTHSCSA. Both centers captured 45-degree mydriatic images with no compression. The size of the RIST images is 1888x2224 pixels and the size of the UTHSCSA images is 2048x2392 pixels. Both databases were collected in the South Texas area. For the database provided by the UTHSCSA, no information about age or sex of the patients was provided. In the case of the RIST database, the distribution of patients is 50.8% females and 49.2% males. Age information is also provided and it is detailed as follows: 1.1% [0 to 24 years], 6.6% [25 to 44 years], 26% [45 to 64 years] and 66.3% being aged 65 years or older. . All the images that presented with cataracts at their early stage, retinal sheen, or lighting artifacts were considered for this study. We excluded retinal images presenting advanced stages of cataracts, corneal and vitreous opacities, asteroid hyalosis, and significant eye lashes or eye lids artifacts. The number of images excluded in this study corresponds to 67 images or 5.8% of the RIST database and 57 images or 5.2% of the UTHSCSA database.

Fig. 3.12 shows examples of images from the three FOV found in both databases. Fig. 3.12a is centered in the optic disc (FOV1). Fig. 3.12b is centered in the fovea (FOV2), and Fig. 3.12c is focused on the superior temporal region of the retina (FOV3). Each image was graded independently by a certified ophthalmic medical technologist in the

following categories: Normal, Non-Proliferative DR (NPDR), Sight Threatening DR (STDR), and Maculopathy. Table 3.8 shows the distribution of each subject's eye in these categories. In addition, ten retinal pathologies were specified by the technologist according to Tables 3.9 and 3.10. Seven pathologies are related to DR: Microaneurysms, hemorrhages, exudates less than one disc diameter away from the fovea, exudates elsewhere, intra-retinal microvascular abnormalities (IRMA), neovascularization on the disc (NVD), and neovascularization elsewhere (NVE). The three pathologies related to AMD were: Drusen, abnormal pigmentation, and geographic atrophy.
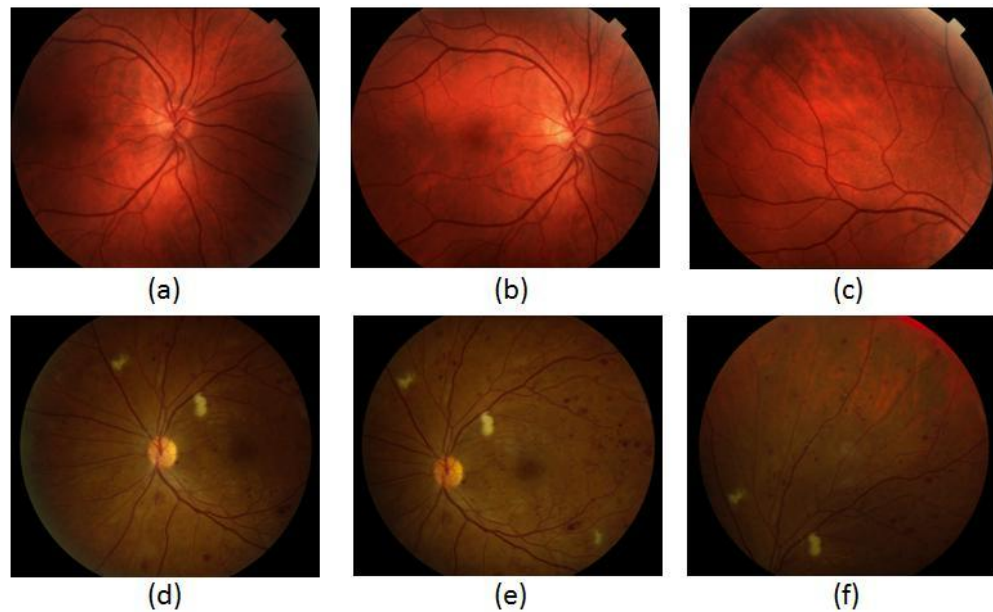
Figure 3.12 (a-c) FOVs 1, 2 and 3 of a normal retina from the RIST database; (d-f) FOVs 1, 2 and 3 of an abnormal retina from the UTHSCSA database.

Table 3.8 Distribution of the RIST and the UTHSCSA databases

Database	Number of Patients	Normal eyes	Non-Proliferative DR eyes	Sight Threatening DR eyes	Maculopathy
RIST	378	64	486	158	174
UTHSCSA	444	116	418	292	207

Table 3.9 Distribution of DR pathologies for the RIST and the UTHSCSA databases

Presence of Lesion	Micro-aneurysms	Hemorrhages	Exudates Fovea	Exudates elsewhere	IRMA	NVE	NVD
Number of images in RIST	378	511	174	248	80	30	58
Number of images in UTHSCSA	274	316	207	284	70	59	118

Table 3.10 Distribution of AMD pathologies for the RIST and the UTHSCSA databases

Presence of Lesion	Drusen	Pigmentation	Geographic Atrophy
Number of images in the RIST database	343	345	154
Number of images in the UTHSCSA database	188	86	54

The criteria followed by the grader to evaluate the quality of the image are specified in Table 3.11 as other published articles [44]. In our approach, only the images with high and medium quality were used by the algorithm. Following the criteria, we removed 193 images, or 16.7% of the RIST database, and 111 images or 10.2% of the UTHSCSA database. Fig. 3.14 shows examples of images not considered for this study due to their low quality.

Table 3.11 Criteria for image quality

Quality	Definition
High	Vessels clearly visible within 1DD of center of fovea and/or smaller vessels visible over 90% of image
Medium	Vessels clearly visible within 1 DD of enter of fovea and/or smaller vessels visible over 2/3 image
Low	Vessels not clearly visible within 1 DD of center of fovea and/or smaller vessels not visible over 1/3 image
Reject	Vessels not clearly visible within 1 DD of center of fovea and/or smaller vessels not visible over 100% of image
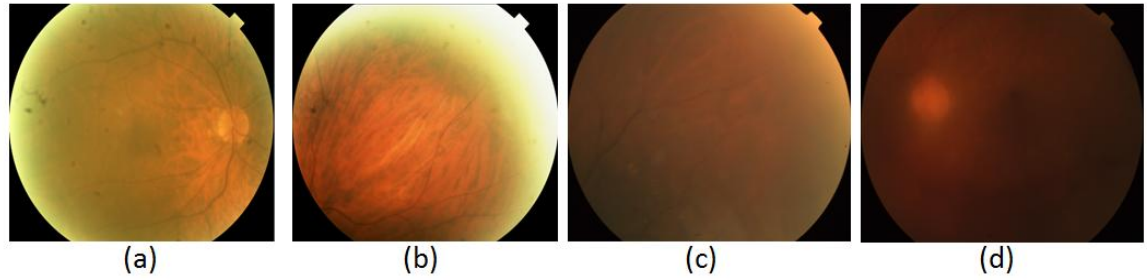
Figure 3.13 Examples of the type of images that were not used by our algorithm. (a) Low quality due to advance stage of cataract, (b) Low Quality due to the reflection of the iris, (c) Rejected image, (d) Rejected image.

3.2.2 Image processing system
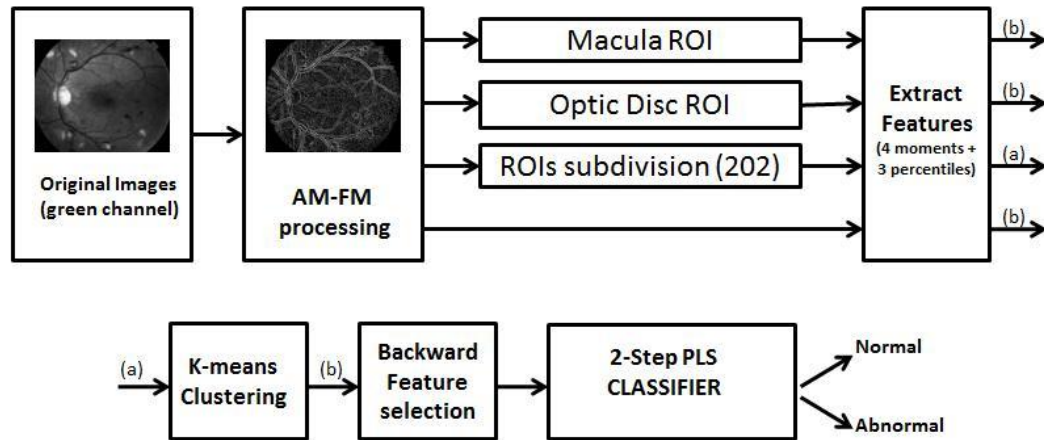
Figure 3.14 Procedure to classify the retinal images.

The detection process starts with the extraction of features from the retinal images (see Fig. 3.14 for the complete procedure). Our algorithm uses a technique called Amplitude Modulation - Frequency Modulation (AM-FM) [199] to define the features and to characterize normal and pathological structures based on their pixel intensity, size, and geometry at different spatial and spectral scales. We refer to the Appendix for a more detailed explanation of the AM-FM approach.

Since the result of AM-FM processing produces features that may not be consequential to the accurate classification of images, we used informative outputs of a sequential backward elimination process in which the contributions of each feature is measured and the ones that do not improve the classification performance are eliminated from our set. This process is applied independently for each of the pathologies of interest in order to obtain a better characterization of the pathologies.

In order to extract more information from an image, AM-FM decomposes the images into different representations which reflect the intensity, geometry, and texture of the structures in the image. In addition to obtaining this information per image, filters were applied to obtain image representations in different bands of frequencies. For example, if a medium or high pass filter is applied to an image, the smaller retinal structures (e.g. MAs, dot-blot hemorrhages, exudates etc.) will be enhanced. This can be observed in Fig. 3.15(b) and 3.15(c), where the different type of red lesions, exudates and thinner vessels present in the retinal region are captured. On the other hand, if a low pass filter is applied then larger structures are captured such as wider vessels as shown in Fig. 3.15(e). By taking the difference of the two lowest scale representations, smaller vessels can also be captured, as seen in Fig. 3.15(f). Using these two ways of processing (AM-FM image representations and output of the filters), more robust signatures of the different pathologies can be characterized.
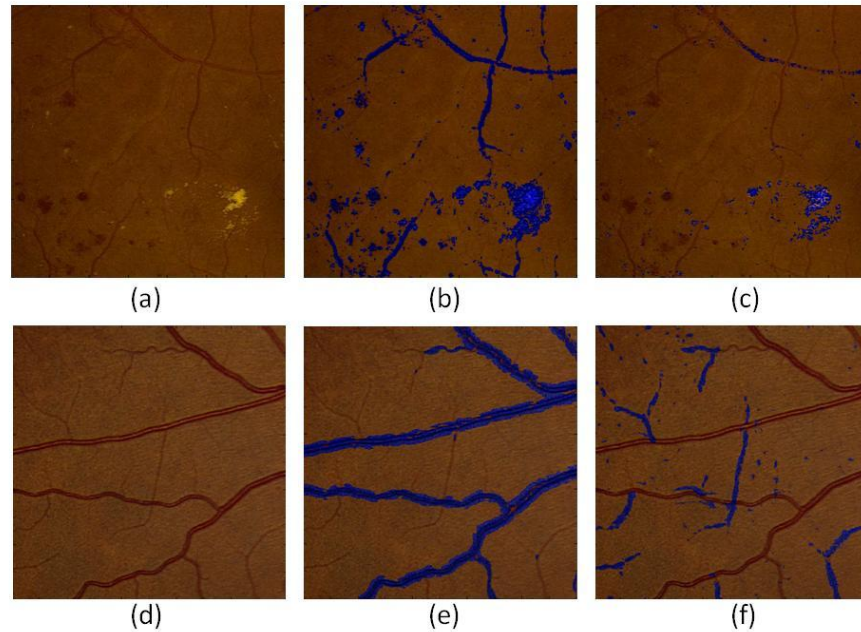
Figure 3.15 Structures in the retina captured by the AM-FM estimates using high values of the Instantaneous Amplitude (IA, in blue). (a) Region of a retinal image with pathologies; (b) Image representation using medium frequencies, which captures dark and bright lesions as well as vasculature; (c) Image representation using high frequencies, notice that this image captures most of the bright lesions; (d) Region of a retinal image with normal vessel structure; (e) Image representation using a very low frequency filter; (f) Image representation of (d) obtained by taking the difference between the very low and the ultra-low frequency scales, in this image the thinner vessels are better represented.

In order to facilitate the characterization of early cases of retinopathy in which only a few, small abnormalities are found our process divides the images into regions of interest or ROIs. A sensitivity analysis on the size of the ROIs found that square regions of 140 by 140 pixels were adequate to represent features of small structures that can appear in the retina such as MAs or exudates. A total of 202 ROIs were necessary to cover the entire image. For classification, a feature vector was created using a concatenation of the following seven features from each region: a) the first four statistical moments (mean, standard deviation, skewness and kurtosis) and b) the histogram percentiles (25th, 50th and 75th).

A *k*-means clustering approach is performed to group the ROIs with similar features using the Euclidean distance between features. In this way, we avoid the necessity of time consuming process of grading each region using an unsupervised algorithm. The resulting clusters become the representative features of the image, producing in turn a representative feature vector per image. Once the feature vectors are extracted, we use them in the classification module (last block in Fig. 3.14). This module used a Partial Least Squares (PLS) regression classifier in order to find the relevant features that classify images as normal or abnormal according to ground truth.

3.2.3 Experimental Design

The following paragraphs describe the experiments performed to assess the accuracy of the system in detecting the retinal pathologies listed in Tables 3.9 and 3.10. These pathologies are characteristic of either DR or AMD diseases. In this section we describe in detail the approaches taken for assessing the presence of these diseases in the retinal photographs.

3.2.3.1 DR classification

For DR-related pathologies, the performance of the algorithm was measured in its ability to discriminate DR cases from normal cases. To do this, we created a mathematical model of the images by training the system using a subset of the data. This training set produces a model to which the testing images are compared with. If the result of this comparison is greater than a pre-defined threshold, the image is considered abnormal (or suspect for DR). Images that fall below the threshold are labeled as normal.

Additionally, the algorithm was tested on sight threatening DR (STDR) cases, where STDR is defined as an image presenting with NVE, CSME, or NVD. In the following sub-sections we detail the special properties that make the AM-FM representations ideally suited for the detection of CSME and NVD.

Clinical Significant Macular Edema (CSME): Previously, investigators have found an association between hard exudates near the fovea and CSME [205], [206]. Although the presence of hard exudates is one of the most common findings in macular edema, the presence of hard exudates is not always indicative of edema. Previous research has demonstrated that the sensitivity of exudates in predicting macular edema is 93.9% [207]. In a screening environment, we do not unequivocally determine its presence or absence. Our goal is simply to identify those patients at-risk based on the presence of hard exudates. For screening purposes, the presence of exudates within 1 disc diameter (DD) of the fovea was considered to be a surrogate for CSME [208]. The Fig. 3.16 shows an example of how AM-FM highlights the presence of exudates while minimizing interference from blood vessels. In this figure we see a normal retina (Fig. 3.16a) and one containing exudates within 1 DD of the fovea (Fig. 3.16b). Fig 3.16c shows the AM-FM decomposition of the normal retina for the high frequencies. It can be noticed that the representation eliminates all the vessels from the image and only shows a dark background. In contrast, using the same high frequencies, the AM-FM decomposition for the abnormal retina clearly highlights the exudates while eliminating the vessels.
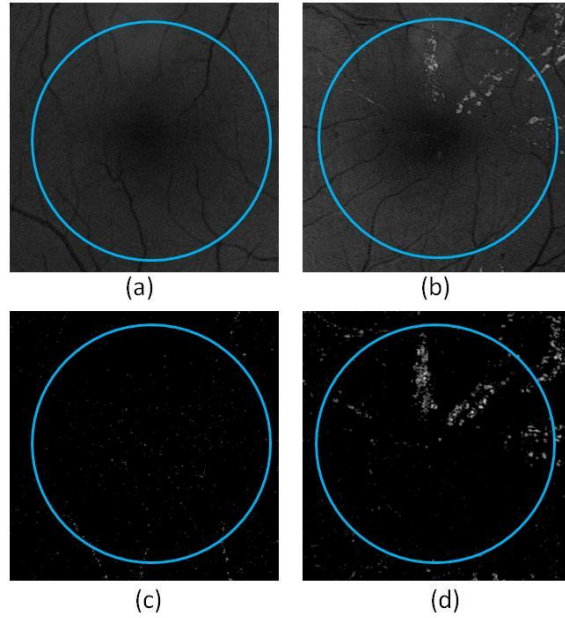
Figure 3.16 Examples of structures captured by the AM-FM estimates using high values of the Instantaneous Amplitude in macular regions (the circle circumvents an area equal to one disc diameter from the fovea). (a)Normal macula, (b) Macula with hard exudates, (c) Instantaneous amplitude of the normal retina in the high frequencies scale (d) Instantaneous amplitude of retina with exudates in the high frequencies scale.

Neovascularization on the Optic Disc (NVD): This pathology is defined as the growth of new vessels within 1 DD of the center of the optic disc. In Fig. 3.17, we show how NVD is represented by AM-FM. Notice for example that by using medium frequencies (Fig. 3.17(b), 3.17(e)), the vessels in the optic disc and NVD are detected, while by using high frequencies most NVD is detected with high intensity, as it shown in Fig. 3.17(f). The combinations of these AM-FM representations into our classifier facilitate the robust and accurate determination of the abnormality. The small amount of noise present in Fig. 3.17c and 3.17f are due to a bright nerve fiber layer, but its representation has less intensity than the abnormal vessels.
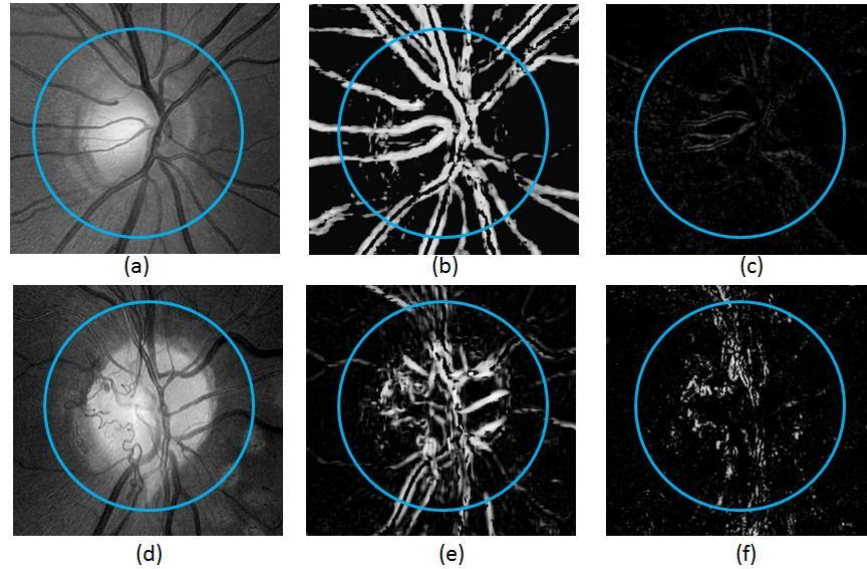
Figure 3.17 Examples of structures captured by the AM-FM estimates using high values of the Instantaneous Amplitude for two different optic discs. (a) Normal optic disc, (d) NVD, (b) and (e) Instantaneous Amplitude of (a),(d) using medium frequencies, (c) and (f) Instantaneous Amplitude of (a),(d) using high frequencies

3.2.3.2 AMD classification

In addition to testing the images for the presence of DR, three different pathologies related to AMD were analyzed: drusen, abnormal pigmentation, and geographic atrophy (GA). Fig. 3.18 shows an example of a retinal image with drusen and one of its corresponding AM-FM image representations. As seen in this example, drusen are noticeably highlighted by AM-FM. We then tested the system in the following scenarios: Normal vs. drusen, normal vs. abnormal pigmentation, Normal vs. GA, and normal vs. all AMD pathologies. For the drusen experiment, all stages of presence of drusen where categorized in the same group without distinction of severity, e.g. a few isolated druse versus large, confluent drusen.

(a)   (b)
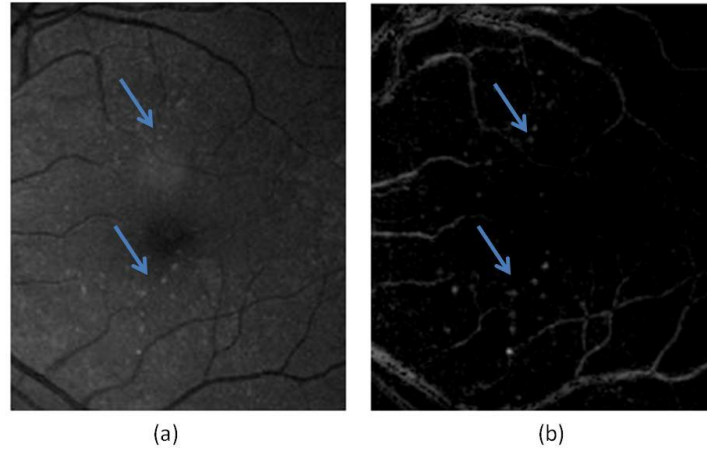
Figure 3.18 Structures capture by the AM-FM estimates using high values of the Instantaneous Amplitude in low frequencies of a retinal region with drusen.

3.2.4 Results

3.2.4.1 Ground Truth

In order to analyze the consistency of the grading criteria, a randomly selected subset of 10% of the data from RIST and UTHSC was given to a second grader. We have to emphasize that the grading developed by the first grader is taken as the ground truth against which our algorithm is compared. The random selection was constrained in order to obtain a minimum set of 25 samples using the Tukey's 5^k Rule [209] for estimating the variance in the distribution from each of the main categories: CSME, IRMA+NVE, NVD, Normal retinas and NPDR. This new subset of our database was graded by a second reader using the categories described in Tables 3.9 and 3.10. The agreement between graders was calculated using the kappa value. First, we calculate the kappa for 3 classes: Normal retinas, Abnormal retinas and Sight threatening eye diseases; and then we calculate the kappa value for the three sight-threatening categories related to advanced DR: CSME, IRMA+NVE, and NVD. The following table shows the results for the kappa value, the standard error and the 95% confidence interval [210].

Since the RIST database was also graded by an ophthalmologist (third grader), a third experiment (See Table 3.13) was performed in order to compare the results of the first two graders against the one provided by the third one.

Table 3.12 Measurement of agreement between readers using the Cohen's kappa value.

Category	Kappa class	Kappa value	SE	95% CI
Normal vs. Abnormal vs. Sight Threatening	Unweighted	0.61	0.042	[0.52 0.69]
	Linear Weighted	0.69	0.034	[0.62 0.76]
CSME	Unweighted	0.71	0.053	[0.60 0.81]
NVD	Unweighted	0.60	0.068	[0.46 0.73]
NVE+IRMA	Unweighted	0.55	0.063	[0.42 0.67]

Table 3.13 Measurement of agreement of 3 readers using the Cohen's kappa value for the RIST database.

Comparison	Kappa class	Kappa value	SE	95% CI
Grader 1 vs. Grader 2	Unweighted	0.62	0.058	[0.50 0.73]
	Linear Weighted	0.70	0.048	[0.60 0.79]
Grader 1 vs. Grader 3	Unweighted	0.74	0.056	[0.67 0.85]
	Linear Weighted	0.79	0.047	[0.70 0.88]
Grader 2 vs. Grader 3	Unweighted	0.62	0.068	[0.49 0.76]
	Linear Weighted	0.69	0.059	[0.57 0.80]

3.2.4.2 Automatic Algorithm Results

Cross validation was used to assess the performance of the algorithm. The ratio between training and testing data was selected so that 70% of the data was used for training and 30% was used for testing. To get a more robust classification estimate, the images in the training and the testing sets were randomly selected and the average of 20 runs is presented. This procedure minimizes the possible bias incurred if the training and testing sets were fixed [211]. In order to compare our results with recently published algorithms the specificity was fixed to 2 values: 0.50 and 0.60. These values of specificity have been previously used to report sensitivity in two large studies [5], [183].

Fig. 3.19 shows six ROC curves, three for each database for the following experiments:
Normal vs. NPDR, Normal vs. STDR and Normal vs. DR.

Table 3.14 Results of performance evaluation for DR experiments and for each database.

PATHOLOGIES	RIST DATABASE				UTHSCSA DATABASE			
	Number of Images*	AUC	Sens for Spec=0.60	Sens for Spec=0.50	Number of Images*	AUC	Sens for Spec=0.60	Sens for Spec = 0.50
DR	[419 144]	0.81	0.92	0.92	[437 136]	0.89	0.94	0.97
NPDR only	[226 144]	0.77	0.83	0.88	[124 136]	0.85	0.90	0.95
STDR only	[193 144]	0.92	0.95	0.98	[313 136]	0.92	0.96	0.96
CSME	[68 44]	0.98	1	1	[147 93]	0.97	0.98	0.99
IRMA + NVE	[95 144]	0.85	0.92	0.93	[137 136]	0.92	0.97	0.98
NVD	[28 50]	0.88	0.90	0.92	[74 94]	0.91	0.95	0.95

* The first term in the brackets refers to the abnormal cases while the second term in brackets refers to the number of normal cases used in each experiment.

Table 3.15 Results of performance evaluation for AMD experiments and for each database.

PATHOLOGIES	RIST DATABASE				UTHSCSA DATABASE			
	Number of Images*	AUC	Sens for Spec=0.60	Sens for Spec=0.50	Number of Images*	AUC	Sens for Spec=0.60	Sens for Spec=0.50
AMD only	[248 44]	0.84	0.90	0.94	[259 36]	0.77	0.90	0.90
Drusen	[91 98]	0.77	0.88	0.95	[143 36]	0.73	0.80	0.85
Pigmentation	[55 98]	0.80	0.90	0.90	[61 136]	0.81	0.87	0.90
Geographic Atrophy	[100 98]	0.92	0.97	1	[76 136]	0.92	0.90	1

* The first term in the brackets refers to the abnormal cases while the second term in brackets refers to the number of normal cases used in each experiment.
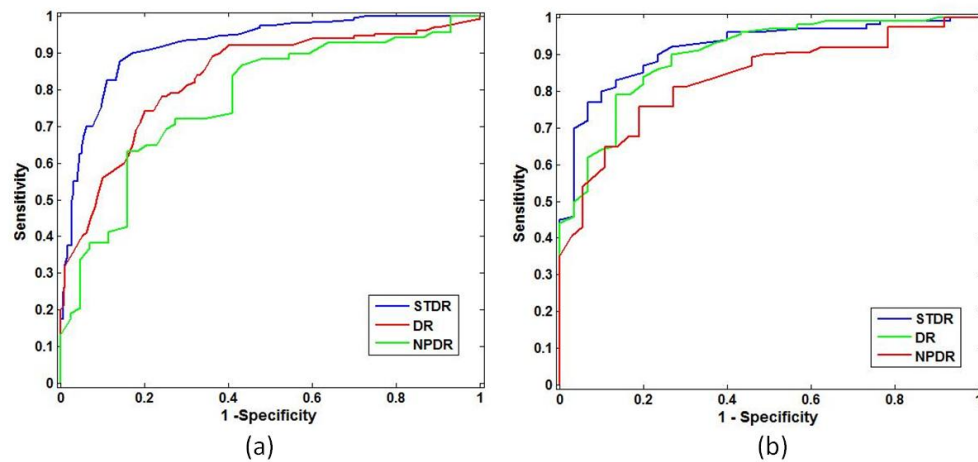
Figure 3.19 ROC curves for the classification of DR, STDR and NPDR. (a) Curves for RIST database, (b)Curves for UTHSCSA database.

3.2.5 Discussion

3.2.5.1 Ground Truth

Tables 3.12 and 3.13 show the inter-reader variability values calculated using the Landis and Koch interpretation of kappa values. Results show substantial agreement between graders, except for the NVE+IRMA cases in which the kappa value is 0.55 (moderate agreement). In analyzing the differences between graders, we noted that the detection of IRMA produced most of the disagreements. An example of this is shown in Fig. 3.20. The two images shown in Figs. 3.20a and 3.20b were presented to the graders again after applying local contrast enhancement and they agreed that the pathology was present. Lower image quality and blurring on some images are some of the factors that contributed to the disagreement between graders. In addition, we found that the presence of other pathologies mask the presence of IRMA as it is shown in Fig. 3.20a.

Figure 3.20 Retinal images with IRMA. (a) Presence of IRMA in the image was not detected by the first grader, (b) Presence of IRMA in the image was not detected by the second grader, (c) and (d) Images a and b with enhancement.

Since the images from RIST were graded previously by the third grader, an ophthalmologist, the kappa value was calculated again for this set. The values shown in

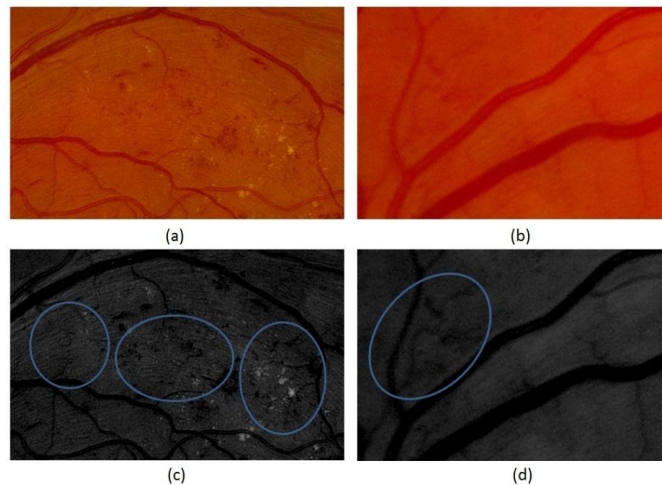table 3.8 indicate substantial agreement (kappa values higher than 0.6) between the ophthalmologist and the first grader (ground truth for our algorithm) at the 95% confidence interval. The comparisons between graders (1,2) and (2,3) also show substantial agreement. Furthermore, the kappa values also suggest that since a ground truth is required to train the classifier, different graders can lead to different classification models even though the same set of images is used.

3.2.5.2 Automatic Algorithm Results

The results presented here are the first test of a novel DR detection algorithm in a realistic clinical setting. Although different databases were used, the results for both databases are consistent, in particular in patients with STDR. For both databases the best results are obtained for CSME detection (hard exudates less than one disc-diameter away from the fovea) and the worse are obtained for the detection of images with drusen. It can be seen from the table above that the majority of the experiments, especially in the case of DR, the results of the UTHSCSA database (AUC = 0.89) are slightly better compared to the RIST results (AUC = 0.81). One of the main factors contributing to this difference is the higher quality images found in the UTHSCSA database, as assessed by the expert graders.

We also noted that the number of cases with STDR is larger in the UTHSCSA database. This results in a larger number of images with multiple abnormal features, and thus a more accurate classification by the system. For comparison, almost two thirds of the UTHSCSA database is composed of STDR cases, while only half of the cases in the RIST database present signs of STDR.

The detection of the non-proliferative state of DR composed of images with MAs, hemorrhages, or hard exudates away from the fovea proved the hardest to detect. Still, the sensitivity values obtained for a specificity of 50% are comparable or better than the ones presented by the larger studies in the field. Detection of exudates was particularly good, as evidenced by the CSME results of Table 3.14.

For detection of NVD, the algorithm achieved AUCs of 0.88 and 0.91. This result highlights one of the advantages of our approach, as abnormal vessels can be discriminated from normal ones through analysis of the different image representations generated by AM-FM without the need for explicit segmentation of the vasculature. To the best of our knowledge, this is the first published result on automatic detection of NVD. Detection of NVE and IRMA is another area in which results have not been reported extensively. When obtaining ground truth, there was moderate agreement between the graders as to which category the images belonged to, and thus both diseases were treated in the same category when reporting the results of the algorithm. Our system achieved very high accuracy of detection of this category, in particular for the UTHSCSA database.

One of the problems encountered was the relative low proportion of cases with early stages of DR. This is due to the nature of the centers where the data were collected, which tended to bias the samples to patients with advanced stages of retinal disease. In the future, we will train the system using a database that will contain a more proportionate number of DR stages, ranging from normal to NPDR, PDR, and maculopathy. In our experiments we have found that a robust training set is the most important aspect when improving the performance of the system. In fact, as the number

of cases analyzed by the algorithm increased, so did its accuracy. This is evidenced by the improvements found over the results presented in our previous publications on the topic [184], [204]

An advantage of our top-down approach is clearly shown in the detection of abnormalities related to AMD. Although the system was not originally intended for those abnormalities, by adding AMD cases to the training database we were able to screen for these lesions with relatively high accuracy (sens/spec = 0.94/0.50 and 0.90/0.50 for the RIST and UTHSCSA databases respectively).

The results presented in this chapter are comparable with the ones presented by other investigators previously described in chapter 2.

By observing the ROC curves (Fig. 3.19), the performance of the algorithm in both databases for the detection of STDR cases is very high, with sensitivities of 96% and 98% for a fixed specificity of 50%. If we fix the specificity to 80%, the algorithm achieved sensitivities of 92% and 85% for the RIST and UTHSCSA databases, respectively. For the other two experiments, NPDR and DR, we achieved sensitivities in the range of [88% 97%] for 50% specificity.

In conclusion, this work presents a viable and efficient means to characterize different retinal abnormalities and build binary classifiers for detection purposes. Although automatic detection of DR has been studied by different groups in the last decade, to our knowledge, automatic detection of STDR as well as neovascularization, pigmentation and GA has not been concurrently addressed at the levels of performance presented in this work.

Chapter 4: Detection of Hard Exudates and Red Lesions in the Macula Using a Multiscale Approach

Abstract

In this chapter, we present an automatic system to detect pathologies on the macula such as hard exudates microaneurysms, and hemorrhages. Our approach is a bottom-up implementation, which tries to capture each abnormal structure in the macula in order to detect DR lesions. This technique starts by eliminating the non-uniform illumination thereby enhancing the contrast of red lesions in the images. Possible DR lesion (hard exudates and red lesions) candidates on the macula are extracted by using amplitude-modulation frequency-modulation (AM-FM) features. AM-FM features extract texture information from different frequency scales, providing for an effective method for the detection of hard exudates and red lesions. For each lesion candidate, we also extract shape, color and other texture features that are then combined with AM-FM features. Pathologies in the macula are detected from the candidate lesions using supervised classification with Partial Least Squares (PLS).

4.1 Introduction

Located at the center of the macula, the fovea contains the highest density of photoreceptors in the retina and is responsible for the central vision. Many pathologies occurring on or near the fovea, such as clinically significant macular edema (CSME), represent a high risk for vision loss. For example, there is an association between hard

exudates near the fovea and CSME [208]. However, not all the types of lesions in the macula represent a comparable risk to patients. For example, drusen, which look similar in shape and color to exudates are not immediately sight threatening; thus, must be differentiated from hard exudates, which are high risk for sight threatening disease and demand an alternate clinical pathway of patient management.

Many approaches have been proposed as a means for automatic DR screening. Most of them utilize "bottom-up" techniques in which segmentation of the lesions is required in order to detect DR. Other approaches [183], [184] are "top down" where segmentation and grading of specific lesions is not necessary to classify the image as normal or abnormal. Much of the reported work has focused either on the detection of red lesions such as microaneurysms and hemorrhages on the fundus images [92], [190], [212] or on the detection of bright lesions such as exudates and cotton wool spots [80], [177] , [178].

The extraction of features on the retinal images is commonly the basis for most automatic classification systems. Morphological methods [176], Gabor filters [178], and Wavelet transforms are the most popular methods for feature extraction. A number of different classifiers have been used to process the extracted features. Sopharak et al. [177] used an unsupervised method called Fuzzy C-means. The authors in [178] used Neural Networks in which each pixel is associated with a soft label indicating the probability of a pixel being bright. In a different approach to detect red lesions, Niemeijer et al. [92], used k-nearest neighbors classifier with Neural Networks.

Our approach uses an optimization approach to select the most promising Amplitude-Modulation Frequency-Modulation (AM-FM) features. Contrary to other methods, the same system is applied to detect red lesions and hard exudates.

4.2 Data Description

The images were acquired at the University of Texas Health Science Center, San Antonio (UTHSCSA). 153 macula-centered digital fundus photographs were used to train/test our algorithm. The images were acquired using 2392x2048 pixels and 60 degrees field of view. Pixel footprint is about 9 μm. A region of 1 disc diameter (DD) centered in the fovea (1DD = 400pixels) was extracted for each image. Lesions such as hard exudates and red lesions (microaneurysms and hemorrhages) were marked by a certified ophthalmic medical technologist. N=35 images were graded as normal, and the remaining images presented two types of lesions. N=79 images presented hard exudates in the macula, and N=81 images presented red lesions. N= 42 present with both types of lesions. The normal cases also contained images with non-pathological features such as retinal sheen, foveal reflex, and low contrast. Other images presented drusen which are pathologies related to age-related macular degeneration (AMD).

4.3 Methodology

Fig. 4.1 shows the methodology used to detect the bright and dark lesions on the macula. The pre-processing block is applied only to detect red lesions. In the following subsections, we explain the optimization procedure used to obtain the best performance of our algorithm.
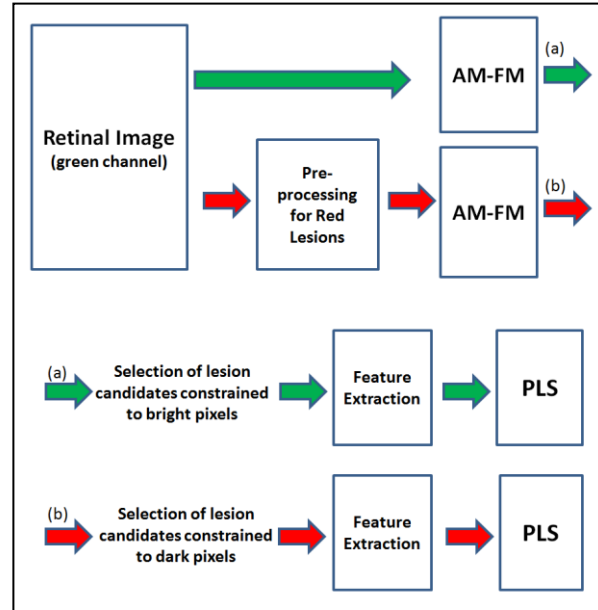
Figure 4.1 Block diagram of our approach to detect hard exudates and red lesions in the macula.
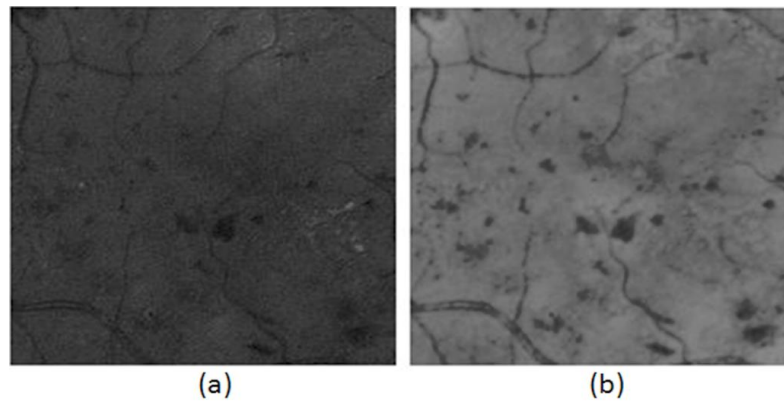
Figure 4.2 Pre-processing for detecting red lesions in the macula. (a) Macula from the original green channel, (b) Macula of the retinal image after apply the pre-processing block explained in section 4.3.1.

4.3.1 Pre-processing for red lesion detection

For the detection of red lesions, the images are pre-processed following a three-step approach. First, we apply illumination correction using a shade correction technique [213]. Second, non-overlapping windows of 30x30 pixels are selected from the image, the bright pixels are detected and then they are replaced by the mean average value of the remaining

pixels in that window. To find the optimal threshold for selecting the brightest intensity pixels, the second derivative of the histogram of the intensity pixel values is calculated. After doing so, the image is smoothed with a 9x9 average filter. Finally, the contrast is enhanced using contrast limited adaptive histogram equalization (CLAHE) [214], as shown in Fig. 4.2.

4.3.2 Amplitude-Modulation Frequency-Modulation (AM-FM)

See section 3.1.2 for more detail on AM-FM and its estimates. These AM-FM estimates were calculated at 5 different frequency scales which correspond to the following bands of frequencies: High (H), Medium (M), Low (L), Very Low (VL) and Ultra Low (U).Then we merged them with the low pass filter (LPF) in 13 different combinations: U-H, LPF, VL, L, M, LPF-H, U-VL, VL-L, L-M, M+H, H, U.

4.3.3 Parameter Optimization

Estimates of the IA, IF magnitude, and IF angle are calculated for the 13 different combinations of scales. A total of 39 different AM-FM feature images are obtained for each image. From them, binary maps are created by thresholding the generated AM-FM feature images. In order to find the optimal threshold value to create the binary maps, an optimization technique was used based on a subset of 53 images. Thirty different percentiles were used to test for the optimal threshold value. Here, note that lesions are characterized by low or high values of the AM-FM features images.

By using the reader-based ground-truth for hard exudates and red lesions on the macula, sensitivity and specificity were obtained and the distance to the ideal point

(100%/100%) is calculated for each of the 1170 points (39 AM-FM feature images times 30 percentile values) for each image and the two types of lesions. The binary AM-FM feature images with a threshold that has the minimum distance to the ideal point (set to be less than 0.3 heuristically on training data) will be selected as an input for our system. Fig. 4.3 shows some examples of distances for different thresholds and different types of lesions. It can be noticed that in Fig. 4.3a for percentiles near 67th, the distance to the ideal point is lower than the acceptable minimum distance = 0.3 (dark blue) for most of the AM-FM feature images so many of them are useful to detect hard exudates. On the other hand, Fig 4.3b shows fewer cases with distances lower than 0.3 meaning that only few of them are going to be used to detect red lesions.
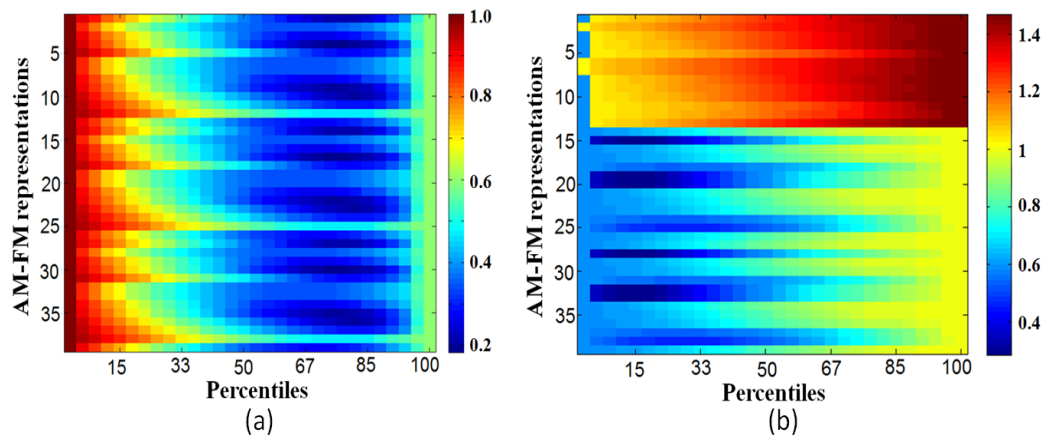
Figure 4.3 Map of distance values for the different thresholds. The y-axis represents the AM-FM representation for the 13 different combinations in the order specified in section A for IA(1-13), IFm (14-26), and IFangle (27-39).). (a) Results of distances after applying the threshold to find lower thresholds to detect hard exudates. (b) Results of distances after applying the threshold to find upper thresholds to detect red lesions.

4.4 Color constraint

Color constraints are applied to the AM-FM binary output using a sliding window of 100x100 pixels. The bright pixels that are higher than the 95th percentile of the content of this window are maintained for the bright lesion detection. For red lesions detection, the

threshold was set to the 7th percentile. The intensity pixels below this threshold are used to mask the AM-FM binary maps. Since there is a great amount of dark pixels in the fovea and lesions are the darkest among them, a special mask of approximately the size of the fovea is used to reduce the false positives rate detection. The pixels with intensity smaller than the 3rd percentile of the content within this window are kept to generate the dark lesions mask. Similarly, pixels that are higher than 99th percentile in the fovea are kept for the bright pixels mask. This modification was implemented after noticing that the foveal reflex, an imaging artifact, is darker than exudates when they are close to each other.

After these masks are generated, they are multiplied by the AM-FM binary maps, as it is shown in Fig 4.4(c). Afterwards, morphological operations to remove small objects that are considered to be noise or vessel lines are applied, as shown in Fig. 4.4(d).
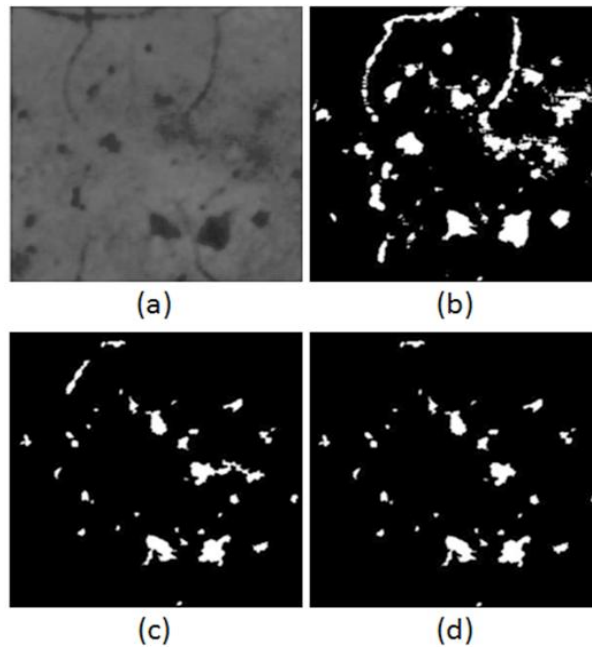

Figure 4.4 Extraction of lesion candidates to detect red lesions. (a) Original image, (b) Binary map obtained with the relevant scales and optimal parameters of AM-FM representation, (c) Constrained binary maps to dark pixels, (d) Candidates of red lesions.

4.4.1 Extraction of features

Sixty-four features are used to characterize each of the possible candidate objects in order to determine its type (non-lesion, hard exudate, red lesion). By using the pixel information of each candidate, we extracted 3 types of features: 1) Color information within the candidate and a neighborhood of pixels outside the candidate, 2) Shape (area, position, eccentricity, major and minor axis length, solidity, perimeter), and 3) Texture information using gray level concurrence matrix (contrast, energy, homogeneity, correlation). The features are normalized to have zero mean and standard deviation 1.

4.4.2 Classification

The features obtained in Section E are the inputs of a linear regression classifier based on partial least squares (PLS) [215]. The classifier is trained for each type of lesion (red lesions and hard exudates) by using the 53 images selected for training purposes.

4.5 Results

The optimal parameters obtained with the optimization process for the detection of hard exudates and red lesions are applied to our testing set consisting of 100 images. After the candidates for each type of lesion are extracted, the model created with the training images is applied to the images. We present results for all the candidates that we extracted for each type of lesion in Fig. 4.5. However, since we are interested in the detection of abnormalities in the macula per retinal image, a point of the ROC curve that has very high specificity is used to reduce the amount of false positives in the classification per image.

A. Hard Exudates

Fig. 4.5 shows the ROC curve for the detection of lesion candidates for red lesions and hard exudates. An area under the ROC curve (AUC) of 0.95 is obtained in the candidate classification. By setting the threshold to obtain a sens/spec = 66%/98%, the classifier trained to detect maculas with exudates in a testing set of 100 images (51 with exudates, 49 without exudates) achieved 100% sensitivity, with specificity of 58%.

B. Red lesions

An AUC of 0.90 is obtained in the candidate classification. By setting the threshold to obtain a sens/spec = 74%/90%, the detection of maculas with red lesions in the testing set (60 with red lesions, 49 with non-red lesions) is 92%/55%.
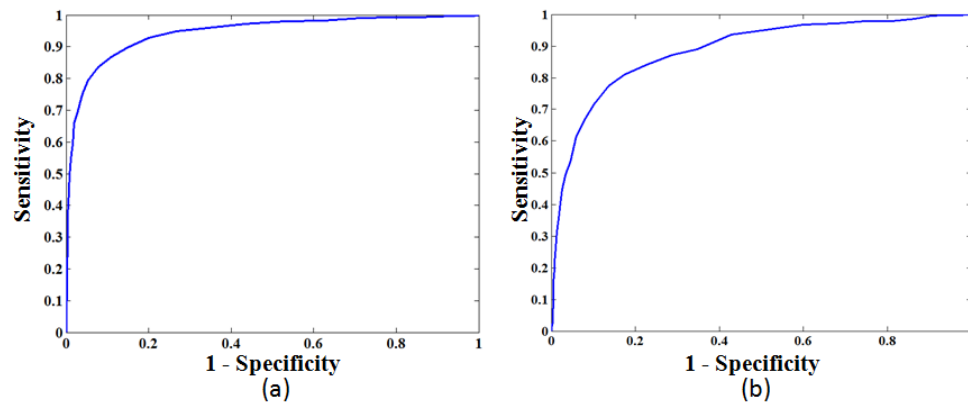
Figure 4.5 ROC curve of the detection of lesions of the extracted candidates. (a) Detection of exudates, (b) Detection of red lesions.
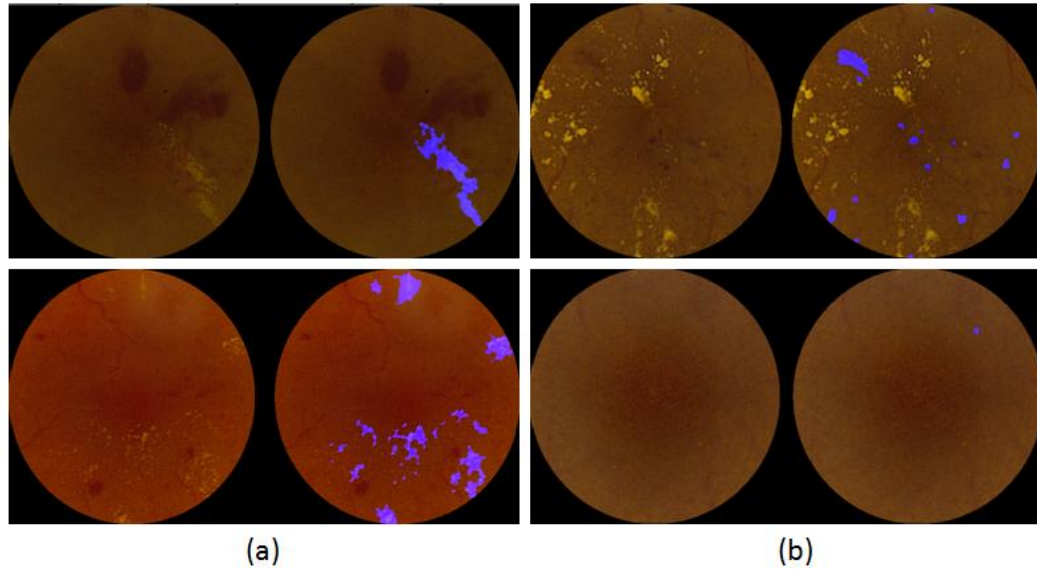
Figure 4.6 Results of lesion detection. (a) Final result of two images after the threshold is set for the macula classification with exudates, (b) Final result of two images after the threshold is set for the macula classification with red lesions.

4.6 Discussion

Structures captured with AM-FM features offer rich information of the analyzed lesions: hard exudates and red lesions. In addition to this, the optimization process helps us obtain high sensitivity in the detection of these lesions even in the candidate selection process prior to the classification.

Fine drusen, also a bright lesion, is a problem for the algorithm, so a post-processing to focus on the shape of these small lesions may improve its performance. As it is known, the shape of the drusen is more similar to a circle than exudates. Image enhancement may also help identify drusen first and help avoid false exudates detection.

The problem of detecting red lesions is very challenging since they present very irregular shapes and have variable texture characteristics. However, the results obtained with this optimized method are encouraging.

Vessels with branches or portions of vessels are another cause of misclassification. A more detailed analysis is going to be performed in order to eliminate those from the candidates.

4.7 Conclusions

A computer-aided detection algorithm based on generalized optimization scheme of image decompositions is presented. Given the optimization process and the flexibility of the implementation, this methodology could be extended to the detection of different types of lesions. In addition, the system only requires image enhancement for red lesions since the exudates are well captured with AM-FM features. The system achieves 100% sensitivity in detecting maculas with hard exudates and 92% sensitivity in detecting maculas with red lesions. In future implementations, post-processing is going to be added in order to increase the specificity of the system.

Chapter 5: Detection of Exudates in the Macula using a Multiscale Optimization Approach

Abstract

Pathologies that occur on or near the fovea, such as clinically significant macular edema (CSME), represent high risk for vision loss. The presence of exudates, lipid residues of serous leakage from damaged capillaries, has been associated with CSME, in particular if they are located one optic disc-diameter away from the fovea. In this paper, we present an automatic system to detect exudates in the macula.

Our approach uses optimal thresholding of instantaneous amplitude (IA) components that are extracted from multiple frequency scales to generate candidate exudate regions. For each candidate region, we extract color, shape and texture features that are used for classification. Classification is performed using Partial least squares (PLS).

We tested the performance of the system on two different databases of 652 and 400 images. The system achieved an area under the receiver operator characteristic curve (AUC) of 0.96 for the combination of both databases and an AUC of 0.97 for each of them when they were evaluated independently.

5.1 Introduction

A recent study from the Johns Hopkins University found an increase of 89% of people over 40 with diabetic retinopathy (DR) since 2000 [216]. The statistics suggest that DR is

the leading cause of new blindness in the US, affecting 25.8 million people [216]. Clinically significant macular edema (CSME) is one of the main contributors of vision loss in diabetics, accounting for 75% of sight-threatening cases [217]. This condition, which can appear at any stage of DR, affects the macula, the region that contains most of the photoreceptors in the retina. In CSME, an incremental thickening of the macular area in the retina occurs due to the accumulation of fluid. Diagnosing CSME requires stereo imaging or optical coherence tomography (OCT) imaging. However, it has been demonstrated that hard exudates located within a 1 disc diameter (DD) area centered in the fovea are surrogates for CSME [208]. By detecting cases with exudates in the macula and providing proper treatment, the risk of moderate vision loss decreases to 50%, according to the Early Treatment Diabetic Retinopathy Study (ETDRS) [218]. Thus, it is important to develop accurate methods for detecting the presence of exudates in the macula.

The detection of exudates in the retina has been an active area of research, with increased interest since 2000 [70], [80], [176]. One of the first published papers on exudate detection [174] relied on the use of global and local thresholding in green channel images. In [175], the authors used an image intensity threshold based on estimates of the background image intensity levels. In [82], the authors proposed the use of adaptive intensity thresholding combined with recursive region growing segmentation (RRGS). Other approaches are based on the application of morphological operations to detect contours of exudates [176], fuzzy c-means clustering candidates [80], [177] and combination of classifiers [178] to detect exudate pixels. A recently published approach presented a top-down approach [189]. In [189], the author asses the severity of the

disease by examing the symmetry of the macular region.

Overall, most of the methods used to detect exudates are based on thresholding techniques and a combination of classifiers. However, the direct application of thresholding on color spaces can be problematic due to significant illumination variations. Thus, most techniques require contrast enhancement or illumination correction on the images prior to the application of thresholding. On the other hand, methods based on combinations of classifiers need to apply different classifier methods sequentially, which could potentially preclude their generalization capacity on databases different from the ones used on their studies. In addition, some of the approaches that apply combinations of classifiers also require the application of contrast enhancement to achieve better results.

More recent approaches also include the use of multiscale approaches for lesion detection [178], [163], [167]. Multiscale approaches for detecting microaneurysms are discussed in [163], [167]. Some of these methods are also used to detect exudates.

The proposed algorithm is based on multi-scale amplitude-modulation frequency-modulation (AM-FM) representations which have been shown to be robust and capable of detecting several DR lesions with high accuracy [184], [196]. This algorithm does not require the application of contrast enhancement nor illumination correction. Our AM-FM approach represents the DR images using AM-FM components that are extracted at multiple scales. Within each scale, an optimal threshold is computed based on the detection performance over a training set.

We will demonstrate that our method obtains a good generalization capacity that does not require to be trained with data from multiple databases. The significance of our

approach here is that we train on one database while testing on a completely different database that does not originate from the same source. This is significantly different than most other approaches. Furthermore, it is important to note that AM-FM based approaches have also achieved high classification accuracy rates on large databases that contain several different DR lesions [196].

The organization of this chapter is as follows. Section 5.2 describes the data used to test the proposed approach. The methodology is explained in Section 5.3. Results and discussion are presented in section 5.4. Concluding remarks are given in Section 5.5.

5.2 Data Description

Two databases were used to test our system. The first set of images was acquired at the University of Texas Health Science Center in San Antonio (UTHSC SA). The images were taken using a Canon CF-60uv retinal camera with a 60 degree field of view (FOV). The size of the UTHSC SA images is 2048x2392 pixels. The second set of images was obtained from the publicly available MESSIDOR dataset [19]. These images were acquired at the Service d'Ophtalmologie, Hôpital Lariboisiere, Paris. Images were acquired using a 3CCD camera on a Topcon TRC NW6 retinograph with a FOV of 45. The size of the MESSIDOR images is 1488x2240 pixels. Our dataset consists of 652 images from UTHSC SA, and 400 images from MESSIDOR. From the dataset of UTHSC SA, we selected 52 images to train the algorithm. Thus, we did not perform any training on the MESSIDOR database. Fig. 5.1 shows sample images in our datasets. Table 5.1 summarizes the number of CSME cases for each testing dataset. In order to apply the same classification model to the MESSIDOR images, the images from this

dataset were resized to UTHSC SA dimensions.

Table 5.1 Distribution of Cases in the Testing Datasets.

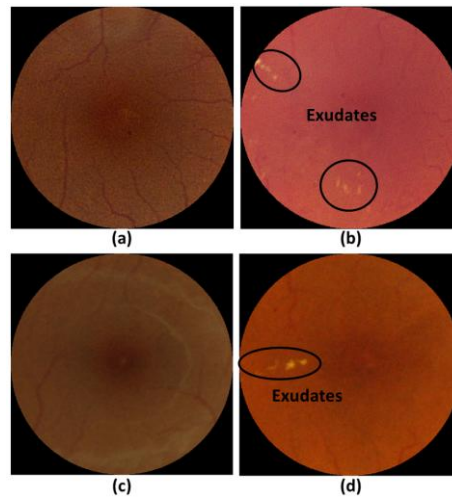| Testing Sets	CSME cases	Normal	Total
UTHSC SA	166	434	600
MESSIDOR	84	316	400

Figure 5.1 Sample images. Maculae without exudates from UTHSC SA (a) and MESSIDOR(c), and maculae with exudates from UTHSC SA (b) and MESSIDOR (d).
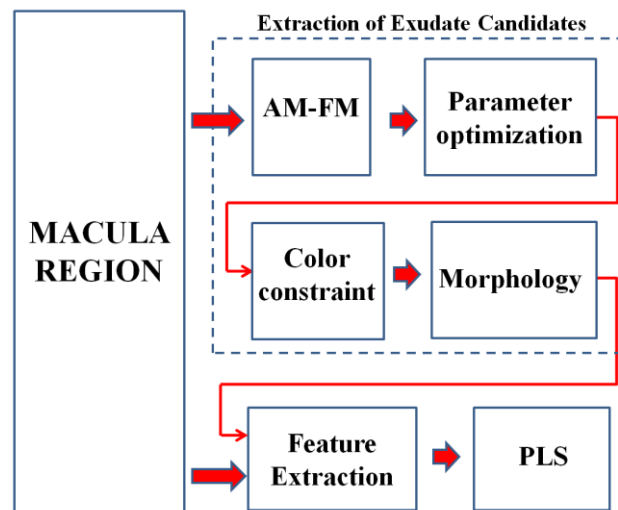
5.3 Methodology

Figure 5.2 Block diagram of the methodology used to detect exudates in the macula.

The methodology is summarized in Fig. 5.2. First, we select a circular region of interest (ROI) of radius of 200 pixels, which is approximately equivalent to 1 disc diameter (DD). AM-FM analysis is applied to the green channel of this ROI. Then, the extracted instantaneous amplitudes (IA) are used for detecting lesion candidates. Lesion candidates are detected by applying an optimal threshold to the IA as described in the following section. Lesion candidates are also constrained to bright pixels, with noise removed using morphological operations. Features such as color from the RGB space, shape, and texture are obtained for each candidate (see subsection 5.3.6 for details). Finally, candidate regions are classified as having exudates or as being exudate-free using partial least squares (PLS). In the following subsections, we provide details on each processing block.

5.3.1 Pre-processing

The mean intensity value of each of the RGB channels was shifted so that all input images shared the same mean value [20]. This procedure standardizes the histograms of all the color channels, as their information will be used as features for the final classification of exudate candidates.

Fig. 5.3 shows our sample images as in Fig. 5.2 after the application of mean normalization. The differences in pigmentation in the normalized images (Figs. 5.3d, 5.3e, and 5.3f) are less noticeable than the ones observed in the original images (Figs. 5.3a, 5.3b, and 5.3c).
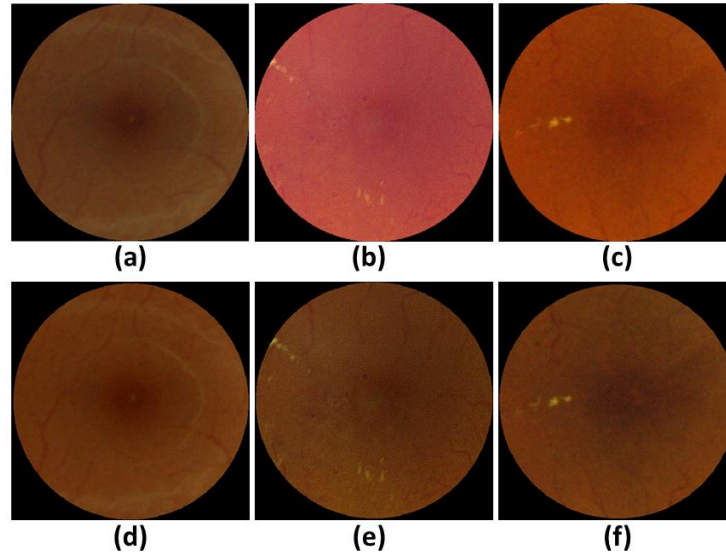
Figure 5.3 Images after applying the normalization by shifting the mean value. Original images in (a), (b), and (c); and after normalization in (d), (e), and (f), respectively.

5.3.2 Amplitude-Modulation Frequency-Modulation (AM-FM)

See section 3.1.2 for more detail on AM-FM and its estimates. The AM-FM estimates are obtained in $M = 4$ different frequency scales [1] which correspond to the following bands of frequencies: High (H), Medium (M), Low (L), and Very Low (VL). The size of exudates ranges between 0.015mm and 0.055mm. However, those smaller than 0.025mm are invisible to fundus photography [219].

The IA estimates provide us with slow-varying (non-texture) intensity information of the structures presented in the image. This information is constrained by the bands of the frequency scale that is used. Thus, different frequency scales will capture structures with different characteristics.

In terms of the AM-FM component functions, we also note that we restrict our attention to the use of the IA for exudate detection. In other words, we have not found that exudate detection can benefit from the use of instantaneous frequency (IF) features.

Table 5.2 Frequency Scales for the Multiscale AM-FM analysis.

Frequency Bands	Instantaneous Period Range in mm
VL	0.064 to 0.176
L	0.032 to 0.088
M	0.016 to 0.044
H	0.008 to 0.022

.
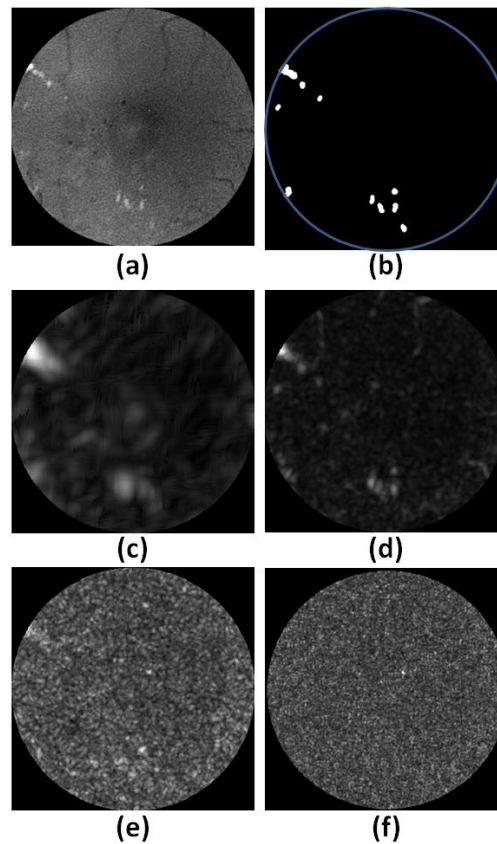
Figure 5.4 Exudate representations in terms of the instantaneous amplitude components. Green channel of the original image (a) and its Instantaneous Amplitude using very low (b), low (c), medium (d) and high (e) frequencies.

Fig. 5.4 shows an example of the extracted IAs for the 4 different scales. It can be observed from the figure that exudates appear with high IA intensity in the VL, L and M frequency scales. In contrast, there are no noticeable differences in intensity between the background and the exudates in the IA for the high-frequency scale (see Fig. 5.4(f)).

Furthermore, we have found this behavior to be typical for the images in our training set. As a result, in what follows, we do not consider the use of the IA from the high-frequency scales for exudate detection. We restrict our attention to the IA extracted from the VL, L and M frequency scales since the lesions present components in those ranges.

5.3.3 Parameter Optimization

Exudates candidates are extracted by thresholding IA outputs on different frequency scales (VL, L, and M). To do so, we need to find the optimal threshold range, which is composed of lower and upper bound percentiles that are found by means of a decision tree. The metric that we used to find the optimal threshold range to extract exudate candidates is

$$dist = \sqrt{(1 - sensitivity)^2 + (1 - specificity)^2}, \qquad (5.1)$$

where *dist* is the Euclidean distance from the operating point to the optimal point of sensitivity/specificity (sens/spec) equal to 100%/100%.

The procedure to obtain the optimal threshold range is explained as follows. The threshold range is initially set to [0th 100th] percentiles in the decision tree. Thus, initially, no pixels are excluded from being considered as exudate candidates. Then, the tree follows two branches: one increases the lower bound threshold by 1 percentile, while the other one decreases the upper bound by 1 percentile, yielding two binary maps in the following threshold ranges: [1st 100th] and [0th 99th], and the procedure is repeated until the optimal threshold range has been determined.

The aforementioned procedure is applied to all 52 images in our training set. Each of these binary maps is compared to the reader-based ground truth for hard exudates,

producing an operating point with values of sens/spec for each image. With this operating point, we calculate *dist* for each training image and its average value is computed.

In Fig. 5.5, the average *dist* values for the first two branches of the tree are 0.95 and 0.98. Since a low *dist* value indicates that the binary maps provide a better detection of the exudates, and brings us closer to the optimal point, the branch with *dist* = 0.95 is chosen.

In general, this procedure would be repeated until we reached the last branch at which *dist* achieved its lower value. In other words, the tree would be pruned once *dist* starts increasing. However, we do not want to do a candidate extraction that overfits the training data. To avoid doing so, we define *thresh_dist*, and the procedure is repeated only until we find the branch that achieves a minimum performance of *dist* = *thresh_dist*. The value of this parameter will determine the number of exudates candidates that the algorithm will extract. If the specified value for *thresh_dist* is high, more candidates, which are not necessarily exudates, will be extracted from each image. If the value for *thresh_dist* is low, the number of false positives among the candidates will be reduced, but the same could happen to the number of true positives. In other words, *thresh_dist* provides a method generalization tradeoff between the inclusion of all exudates and non-exudate structures.

To evaluate the performance of the algorithm, different values for *thresh_dist* were analyzed (Table 5.3). This procedure is applied independently to the three different frequency bands (VL, L, and M) to determine the optimal AM-FM threshold range. By performing the logical disjunction of the optimal binary maps in the three scales, the AM-FM candidates are obtained. If the decision tree of a specific frequency band does not

achieve *dist = thresh_dist*, this band is not used for the extraction of candidates. It is also

clear from the results of Table 5.3 that the optimization approach resulted in the selection

of a single, low-value cutoff. In other words, high IA values resulted in the best exudate
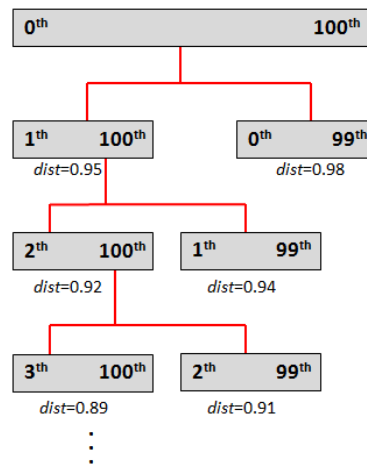
candidates.

Figure 5.5 Decision tree of the optimization procedure for the extraction of exudate candidates.
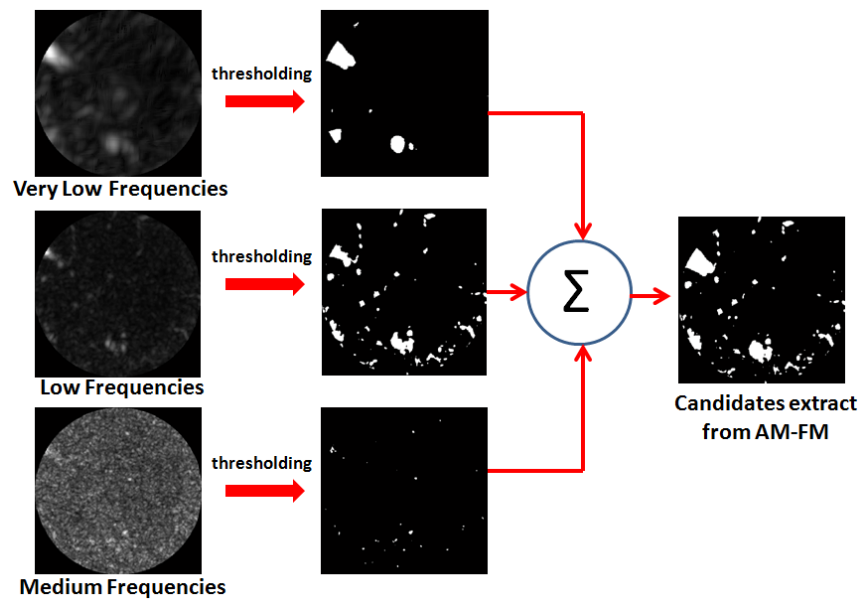

Figure 5.6 Extraction of exudate candidates using AM-FM (See original image and its ground truth in Fig. 5.4a and 5.4b).

In Fig. 6 we show the IA outputs of the reference image of Fig. 4, its thresholded images, and the AM-FM candidates obtained by following this approach. Note that the final image is generated as the union from the 3 scales.

5.3.4 Intensity Constraint

The methodology specified up to section C already extracts candidates that could be provided to the classifier to detect actual exudates. However, other structures such as vessels are also characterized by large IA values.

To reject the possibility of having unwanted structures from being considered as possible exudates, we constrain the candidate exudates to those pixels with large intensity values in the green channel. The additional constraint of requiring candidates to be composed of bright pixels allows us to reject dark regions that may generate high IA values.

To select exudate candidates with bright pixels, we cannot apply global thresholding since an exudate's intensity varies depending on its location in the image. Hence, local thresholding is applied to the green channel by using a sliding window of 100x100 pixels, hereafter referred to as intensity thresholding. The pixels whose intensity is higher than a certain percentile of the content of this window will be preserved as bright pixels. The optimal intensity threshold is the one that achieves the minimum value of *dist* as outlined in the optimization example of Fig. 5.5.

In addition, we empirically set an intensity threshold in the foveal area to the 99th percentile of the macula content. This modification was implemented after noticing that exudates rarely appear in the center of the macula and that foveal reflex, a bright imaging

artifact commonly present in retinal images, is darker than exudates. After this mask is generated, it is multiplied by the binary maps of exudate candidates, as shown in Fig. 5.7.
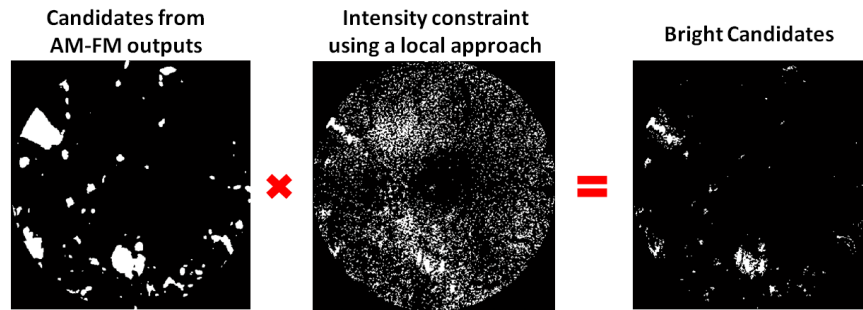
Figure 5.7 Candidates after green channel intensity constraint (See original image and its ground truth in Fig. 5.4a and 5.4b).

5.3.5 Morphology

In the final stage of the extraction of candidates, morphological dilation and erosion are applied with a circular structural element of radius 5 and 4 pixels respectively in order to group small candidates that are close to each other. In addition, we applied morphological close to remove noise by discarding candidates composed of less than N pixels (1 pixel has an area of $81\mu m^2$). We empirically set N=12, which corresponds to an area smaller than the average size of a microaneurysm, which is the smallest pathology in DR. Fig. 5.8 shows the results after applying morphology.
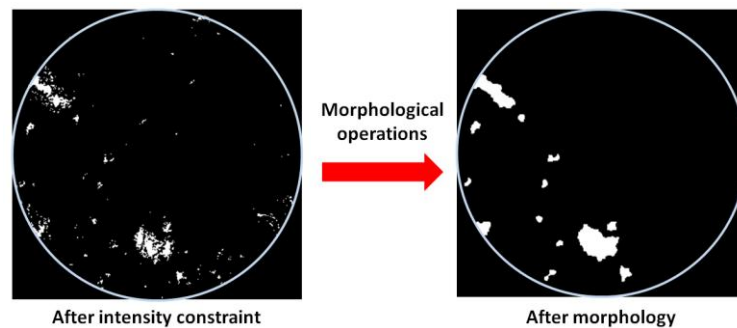
Figure 5.8 Final step of the extraction of candidates using morphological operations.

5.3.6 Extraction of Features

Three types of features (color, shape, texture) are extracted from each candidate to help differentiate the exudates from non-exudates structures.

Color image intensity features from the green and blue channels are extracted for each candidate and from their neighborhood pixels in normalized histograms of 16 bins each. We did not consider color information from the red channel. The red wavelengths penetrate deeper into the retina, reflecting mostly the choroidal depth, where exudates are not present. Additionally, the red channel intensity can be saturated. Therefore, we did not consider color features from the red channel, a common practice in both computer- and human-based retinal image analysis [220], [221].

Texture information for each candidate (contrast, energy, homogeneity, correlation) is obtained by using a gray level co-ocurrence matrix [222] in the green channel. Shape properties (area, perimeter, eccentricity, minor and major axis length and solidity) are obtained from the binary information of each candidate.

The features in the training set are normalized to have zero mean and standard deviation 1. To do so, the mean and the standard deviation values are obtained for each of the features. These two estimates are stored and later used to normalize the features in the two testing sets.

5.3.7 Classification

The features obtained in Section F are the inputs for a linear regression classifier based on partial least squares (PLS) [215]. The classifier is trained by using the features of the candidates that are extracted from the 52 images selected for training purposes from the UTHSC SA dataset.

5.4 Results & Discussion

5.4.1 Parameter Optimization

As discussed earlier, Table 5.3 provides the range of optimal percentile AM-FM thresholds for each *thresh_dist* in each scale of IA. Note that when the value of *thresh_dist* decreases, the range of percentile thresholds is increased, since less information is removed. In subsection 5.4.3, we analyze how these values affect the classification accuracy.

Table 5.3 Results of Optimal range for percentile thresholding for IA Scales.

thresh_dist	IA-VL	IA-L	IA-MF
0.15	-	-	-
0.20	-	[80 100]	[86 100]
0.25	[83 100]	[74 100]	[81 100]
0.30	[72 100]	[69 100]	[73 100]
0.35	[66 100]	[64 100]	[66 100]
0.40	[61 100]	[59 100]	[61 100]
0.45	[55 100]	[54 100]	[55 100]
0.50	[50 100]	[49 100]	[50 100]
0.55	[45 100]	[44 100]	[45 100]
0.60	[40 100]	[40 100]	[40 100]
0.65	[35 100]	[35 100]	[35 100]
0.70	[30 100]	[30 100]	[30 100]

5.4.2 Intensity constraint

The optimal intensity threshold is the one that achieves the minimum value of *dist*. Fig. 5.9 shows the curve of *dist* vs. *percentile threshold*. In this graph, the minimum distance is found for the 94.5[th] percentile. This value was then used for thresholding all the images in the dataset.
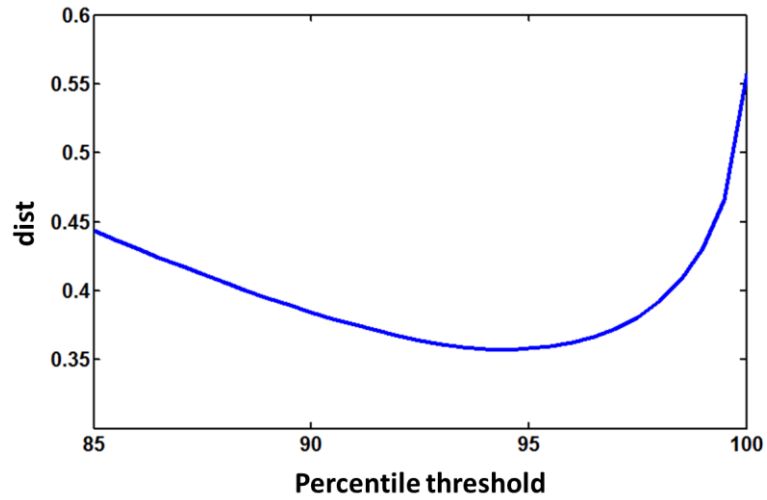
Figure 5.9 Curve of dist vs. percentile threshold to obtain the optimal value for intensity constraint.

5.4.3 Classification

Table 5.4 shows the number of candidates used to train our algorithm for each *thresh_dist* value. It can be observed from this table that, initially, the number of candidates increases along with the value of *thresh_dist*, indicating that more candidates that actually include exudates are detected. The number starts to decrease as candidates that are close to each other combine when the percentile range is increased (see Fig. 5.10).

Table 5.4 Details of candidates in the training stage composed of 52 images.

thresh_dist	Exudates Candidates	Non-exudates Candidates
0.20	378	1406
0.25	399	2082
0.30	399	2375
0.35	393	2548
0.40	387	2614
0.45	387	2671
0.50	383	2661
0.55	380	2617
0.60	378	2576
0.65	377	2525
0.70	375	2496
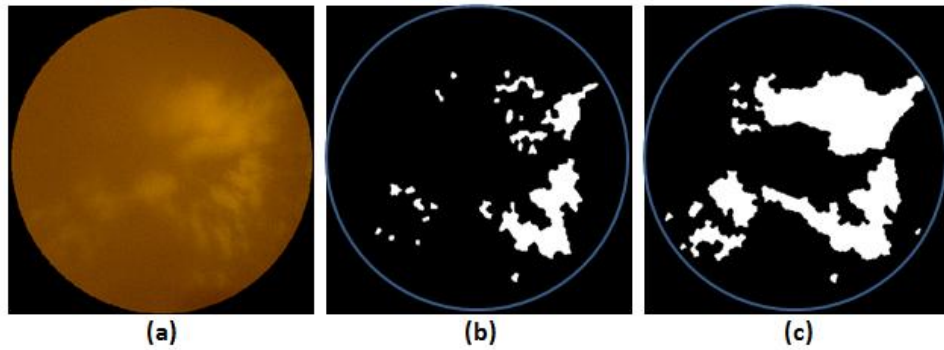
Figure 5.10 Examples of the extraction of candidates for two values of *thresh_dist*: 0.20 and 0.70. (a) Original image. (b) Candidates obtain for *thresh_dist*=0.20, (c) Candidates obtain for *thresh_dist*=0.70.

Here, our focus is to detect the presence of exudates located within one disc diameter of the fovea. To evaluate the performance of our algorithm in the detection of those lesions, we generate a sensitivity/specificity ROC curve per image. To do so, the operating points of the ROC curve obtained for lesion detection in the training set is used to set the operating points for exudate detection on the testing set.

An image is considered to have exudates if at least one candidate is classified as an exudate. Table 5.5 shows the AUC of the two datasets evaluated as two independent test sets and jointly as a single test set. We notice that the results are similar among the

different *thresh_dist* values. For the UTHSC SA cases, we have a small difference across these values, which may be due to our training set being composed exclusively by images from this database; a higher variation can be seen in the AUC values obtained by MESSIDOR for different *thresh_dist* values. Nonetheless, these AUC values are consistently high.

When the testing dataset is composed of the 400 images from MESSIDOR and 600 images from UTHSC SA, the AUC decreases by 1% but the best result is still high with AUC = 0.96 (See red ROC curve in Fig. 5.11).

Table 5.5 AUC for the classification of the testing sets

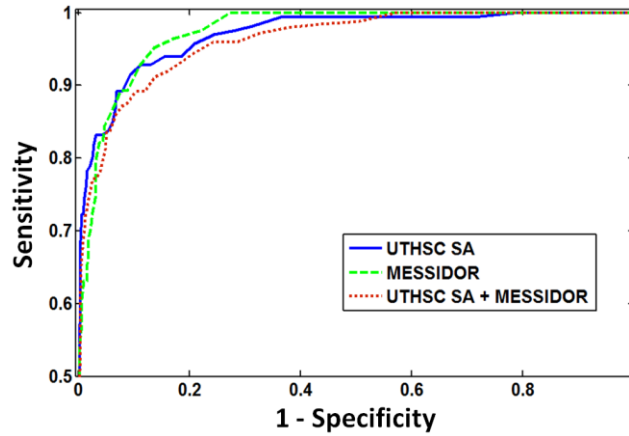| *thresh_dist*	Only UTHSC SA (600 images)	Only MESSIDOR (400 images)	UTHSC SA + MESSIDOR (1000 images)
0.20	0.969	0.960	0.957
0.25	**0.970**	**0.973**	**0.962**
0.30	0.969	0.972	0.959
0.35	0.966	0.970	0.955
0.40	0.966	0.973	0.958
0.45	0.967	0.966	0.956
0.50	0.967	0.964	0.955
0.55	0.968	0.963	0.957
0.60	0.967	0.964	0.957
0.65	0.968	0.963	0.957
0.70	0.968	0.964	0.957

Figure 5.11 ROC curves of the classification of CSME using *thresh_dist* = 0.25 for the two testing datasets evaluated both independently and jointly.

A more detailed analysis for the best result obtained with *thresh_dist* = 0.25 is described in Table 5.6. This table summarizes the results of three operating points in the ROC curves were high sensitivity, high specificity and high accuracy are obtained.

Table 5.6 Sensitivity/Specificity-Accuracy for *THRESH_DIST* = 0.25

Category	Only UTHSC SA (600 images)	Only MESSIDOR (400 images)	UTHSC SA + MESSIDOR (1000 images)
High Sensitivity	0.99/0.64 - 0.74	1.00/0.73 - 0.79	0.98/0.62 – 0.71
High Specificity	0.76/0.99 - 0.92	0.70/0.98 - 0.92	0.73/0.99 – 0.92
Highest Accuracy	0.83/0.97 - 0.93	0.82/0.96 - 0.93	0.77/0.97 – 0.92

By selecting the operating point for high sensitivity in the UTHSC SA database, one image with exudates was not detected. This false negative case is shown in Fig. 5.12a. It is clear in the zoomed area shown in Fig. 5.12b that the exudates were subtle and difficult to visually distinguish. Although the algorithm missed these exudates, due to their focal. minimal presence, they are not considered clinically significant. Fig 5.12 also shows cases incorrectly classified as CSME (false positives). The most common case is the one presented in Fig. 5.12c, where bright drusen are present in the macula. Another

misclassified image is presented in Fig. 5.12d, where retinal depigmentation caused the system to fail. Retinal depigmentation can be similar in tone to paler exudates.

Fig. 5.13 shows cases where exudates are clinically significant and the algorithm classifies them correctly. Similarly, Fig. 5.14 shows cases with exudates that are very challenging to detect. Here, the proposed algorithm is able to detect some of the present exudates and classify the image as abnormal.
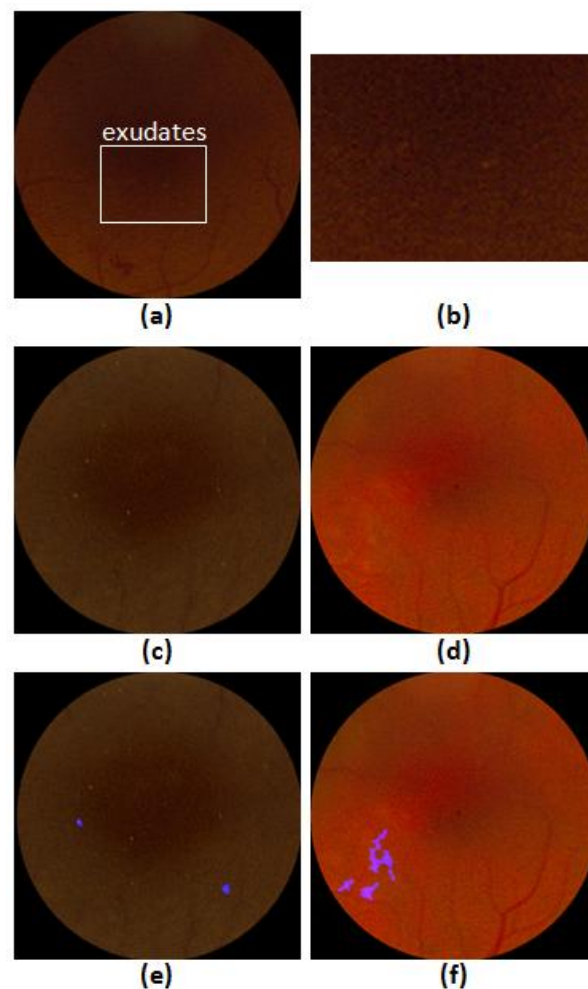
Figure 5.12 Incorrectly classified maculae images. a) CSME case and its zoomed region in (b), Normal maculae in (c) and (d) and their classification results in (e) and (f) respectively.

Figure 5.13 Correctly classified CSME cases in the UTHSC SA database. Original images in (a), (b), and (c) and their classification results in (d), (e) and (f).
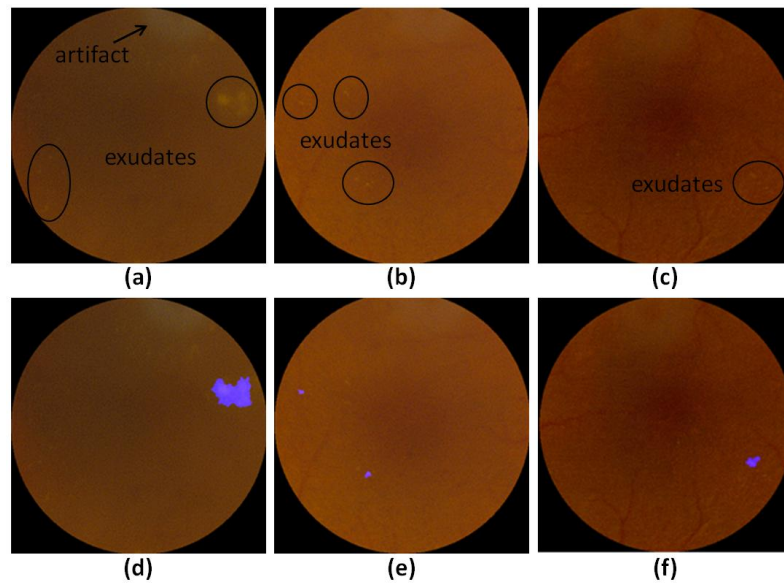
Figure 5.14 Subtle cases of CSME in the UTHSC SA database that were correctly classified by the algorithm. Original images in (a), (b), and (c) and their classification results in (d), (e) and (f).
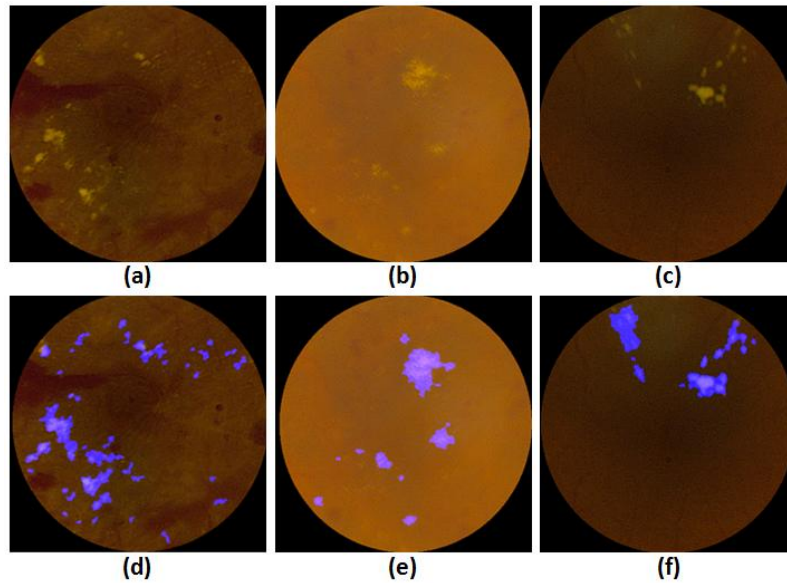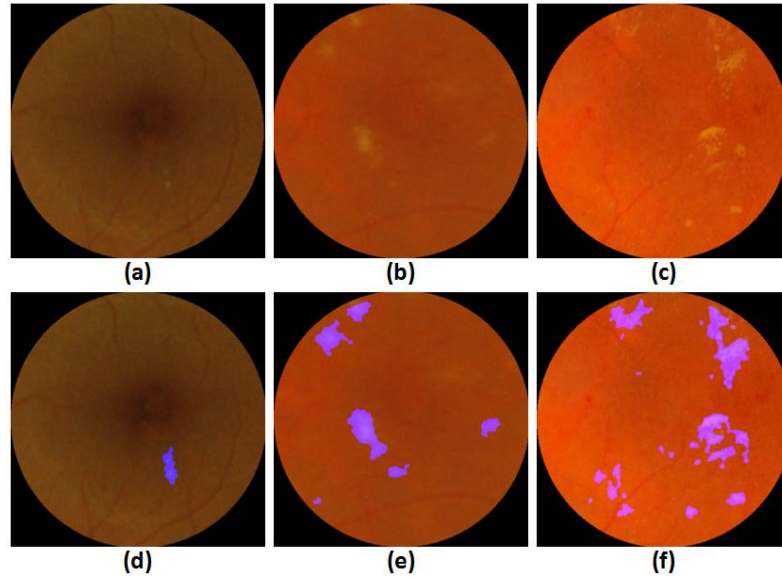
Figure 5.15 Correctly classified CSME cases in the MESSIDOR database. Original images in (a), (b), and (c) and their classification result in (d), (e) and (f).

As mentioned in the introduction section, the method proposed in [189] presented a top-down approach to detect exudates in a retinal image. This method was evaluated in the same MESSIDOR database. In their method, a large ROI area of 2DD is selected, obtaining AUC=0.96 for all the 400 images. It also detects cases with CSME in a reduced set of the 400 images of MESSIDOR obtaining AUC of 0.99. However, they used the same ROI size, which usually contains larger clusters of exudates and are not in the area of definition of CSME. Although a direct comparison with this approach cannot be performed since we used all the 400 images, our result of AUC = 0.97 for CSME cases in MESSIDOR is high.

In the same paper, the MESSIDOR images are combined with other datasets, which reduced their overall performance to AUC = 0.92. In contrast, our results obtained by combining MESSIDOR with UTHSC SA data are only reduced to AUC = 0.96. In addition, our method does not require training in different datasets as they do, making our

method potentially more robust and more likely to be applied in clinical practice. Fig. 5.15 shows three CSME cases correctly classified in MESSIDOR by our algorithm.

5.5 Conclusions

This chapter presents a novel method for detecting exudates in the macula. The algorithm shows robustness, since it did not require retraining when it was tested with a second dataset, the MESSIDOR dataset, obtaining an AUC with high sensitivity/specificity of 100%/73%.

Although the feature extraction and the classifier are important parts of the system, the extraction of candidates is the most important innovation. This system provides a reliable method for extraction of candidates without the need for applying contrast enhancement methods [80], [177] that may enhance the low intensity noise of the images or extracting multiple features for classifiers to be able to detect candidates [80], [178].

In addition, we notice that the fewer candidates obtained with low values of *thresh_dist* give us slightly better results in AUC per image classification than high values of *thresh_dist*. These results agree with previously published papers in DR screening systems [92], [160] in the sense that it is not necessary to detect every pixel of a DR lesion in order to detect with high sensitivity the presence of lesions in a retinal image.

This system can be used as a part of an automatic DR screening algorithm to ensure that no sight-threatening conditions due to the presence of exudates in the macula are missed.

Chapter 6: Detection of Neovascularization in the Optic Disc

Abstract

New vessels that form on the retina and optic disc in response to ischemia from advanced capillary closure are a result of proliferative diabetic retinopathy (PDR) called neovascularization on the disc (NVD). These fragile vessels lead to complications such as vitreous hemorrhages. Accurately detecting NVD is vital to preventing vision loss due to diabetic retinopathy (DR). This paper presents a multiscale method to detect the presence of NVD in digital fundus images. Our method is applied to a manually selected region of interest (ROI) containing the optic disc. All the vessels in the ROI are segmented by adaptively combining contrast enhancement methods with a vessel segmentation technique. Textural features extracted using multiscale amplitude-modulation frequency-modulation (AM-FM) techniques, morphological granulometry, and fractal dimension are used to differentiate NVD from a normal optic disc. A linear support vector machine (SVM) is used to perform the classification, which is tested by means of 10-fold cross-validation. We evaluated the performance of the system using 100 images with NVD and 200 normal images. The system achieved an area under the receiver operator characteristic (ROC) curve of 0.93 with maximum accuracy of 88%.

6.1 Introduction

Diabetic retinopathy (DR) is one of the leading causes of blindness in the world [223]. The disease is asymptomatic in its early stages and can be best managed by the patient by maintaining tight blood sugar and blood pressure control. However, as the disease

progresses, it can become sight threatening. Studies [224], [225] have demonstrated that 50% of type I diabetics and 20% of patients with type II diabetes will progress to advanced stages of DR sometime in their lives. One of these advanced stages is proliferative diabetic retinopathy (PDR). PDR is characterized by the appearance of new, abnormal vessels in the retina. Depending on the location of these new vessels, they can be classified as neovascularization on the optic disc (NVD), where new vessels grow on or within 1 disc diameter (DD) of the optic disc, or neovascularization elsewhere (NVE), where the new vessels are present anywhere outside this NVD region. This paper focuses on the detection of NVD. In early stages, NVD appears as loops or networks of fine vessels [26]. As the disease progresses, the vessels extend outside the optic disc margin and their caliber increases. These new vessels are fragile and can grow into the vitreous gel. Vitreous traction with normal eye movement may lead to the rupture of the new vessels, causing hemorrhages and significant vision loss. Timely treatment with laser photocoagulation can slow progression of the disease. Therefore, detection of these new vessels is of critical clinical importance.

Most of the methodologies used to detect DR have been focused on finding other pathologies such as microaneurysms, hemorrhages, and hard exudates, as summarized in [53], while a few have looked for vascular abnormalities [180], [107]. An approach to detect NVD has been presented by Goatman et al. [104]. In their paper, vessel segments were separated into two abnormal and normal classes. Vessel-like candidate segments on the optic papilla are detected by using watershed lines and ridge strength measurements. Fifteen features, including shape, position, brightness, contrast, and density, were extracted from each candidate. Gaussian-kernel support vector machines (SVM) was

used to classify data represented by those features. The results were validated using leave-one-out cross-validation. Based on 38 NVD and 71 normal cases, the method achieved an area under the ROC curve (AUC) of 0.79 for the detection of segments with NVD and an AUC of 0.91 for the detection of optic discs with neovascularization.

In this chapter, we focus on the development of multiscale image processing approach to better capture NVD vessel properties such as narrow vessel caliber and tortuosity levels. In particular, we extract multiscale textural features from the spatial-frequency domain (AM-FM), multiscale morphology (granulometry), and fractal dimension. The approach is then tested on a larger database, where it is shown to perform better than current techniques for NVD segmentation and detection.

The organization of this chapter is as follows. Section 6.2 describes the database used to test the proposed approach. The methodology is described in section 6.3. Results and discussion based on 300 images are presented in section 6.4. Conclusions are presented in section 6.5.

6.2 Data Description

The images used to test this approach were acquired at the Retina Institute of South Texas (RIST, San Antonio, TX) and the University of Texas Health Science Center in San Antonio (UTHSC SA). The images were acquired at RIST with a TRC 50EX camera with 50 and 35 degrees of field of view (FOV) and at UTHSC SA with a Canon CF-60uv with 60 and 40 degrees of FOV. The size of the RIST images is 1888x2224 pixels and the size of the UTHSC SA images is 2048x2392 pixels. Although images centered on the optic disc were preferred for this study, images centered on the macula

that included the optic disc were allowed.

The dataset consists of 19 NVD and 45 normal cases from RIST and 81 NVD and 155 normal cases from UTHSC SA. Because of the differences in FOV and the variation of disc size diameter between individuals, which is in the range of 0.96 to 2.91 mm for the vertical axis and 0.91 to 2.61 mm for the horizontal axis [9], the images were resized so each had an optic disc with a DD = 400 pixels. Fig. 6.1 shows four examples of normal and NVD cases from the images used in this chapter.
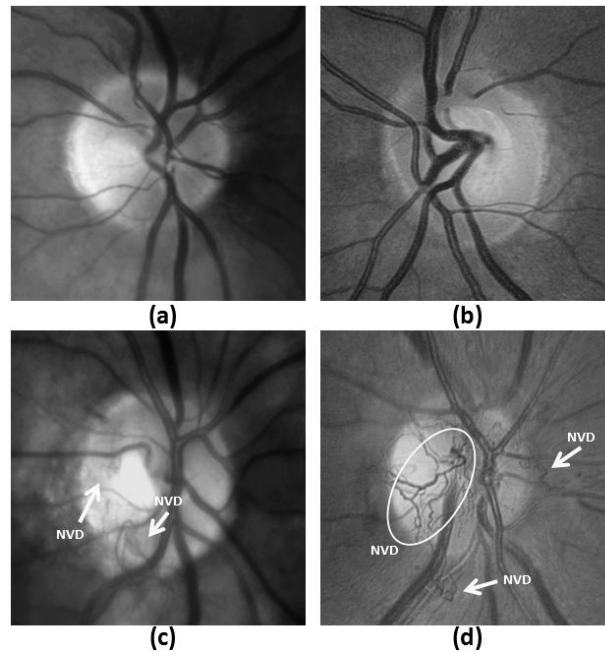
Figure 6.1 Sample images for this approach. a) Field 2 normal optic disc in RIST, b) Field 2 normal optic disc in UTHSC SA, c) Field 1 optic disc with neovascularization in RIST, d) Field 1 optic disc with neovascularization in UTHSC SA.

6.3 Methodology

Since the green channel provides excellent contrast for vessel segmentation [73], [118] [119], we restrict our approach to working with the green image. To avoid possible boundary artifacts, a margin of 60 pixels was added to our region of interest (ROI) of 800x800 pixels. However, features were extracted from the ROI only.

The method is summarized in Fig. 6.2. First, the vessels are segmented using an adaptive vessel segmentation approach. Amplitude-modulation frequency-modulation (AM-FM) features are then extracted from the segmented vessels areas. Next, we compute the fractal dimension and morphological granulometry from the segmented vessels. The extracted features are classified using an SVM with a linear kernel. We provide further details on the approach in the remaining subsections.

Figure 6.2 Block diagram of the methodology used to detect neovascularization in the optic disc.

6.3.1 Adaptive Vessel Segmentation

In Fig. 6.3, we present a block diagram that shows the components of the adaptive vessel segmentation.

Our vessel segmentation technique is based on the methodology presented in [51]. In that paper, the retinal vasculature was segmented after applying a multiscale

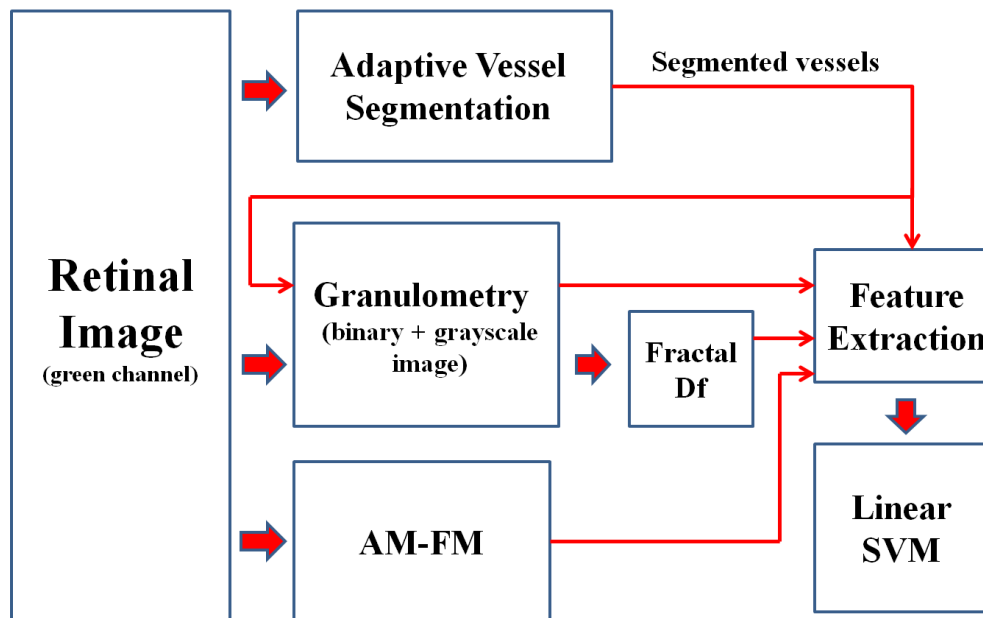enhancement with Frangi filters [130] and second order local entropy for thresholding [226]. The same global procedure presented in [51] cannot be used to detect the very fine vessels characteristic of NVD. Over-segmenting the retinal vasculature can help to detect small vessels, but it also introduces noise. In addition, images taken at different alignment positions, such as those in our dataset, vary in contrast. The optic disc is directly illuminated by the light of the camera in disc-centered images; in macula-centered images, the nasal area receives less light intensity. For these images, different parts of the retina require different levels of enhancement. Therefore, an adaptive image enhancement method, aimed at enhancing vessel boundaries for segmentation, has been introduced to our vessel segmentation procedure.
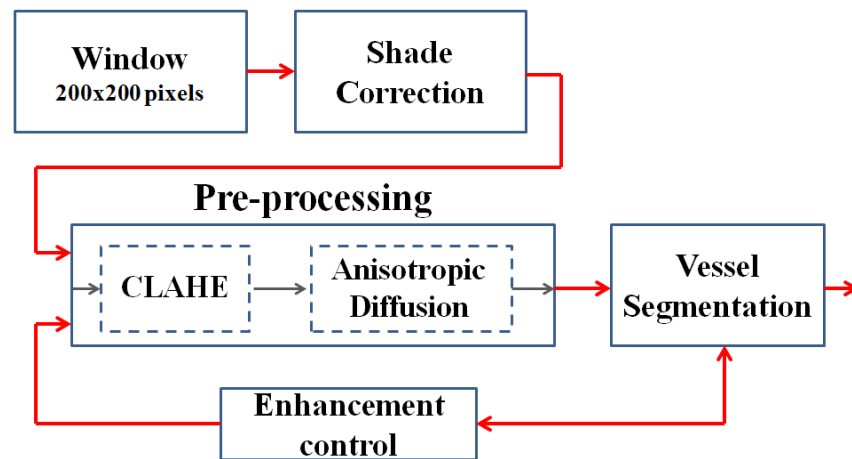
Figure 6.3 Block diagram of the adaptive vessel segmentation procedure. See text for more details.

The first step is to analyze windows of 200x200 pixels that constitute the entire optic disc image (920x920 pixels). The remaining steps of the procedure are applied to these windows to generate our final segmentation.

We reduce non-uniform illumination using shade correction, as described in [51], [64] in order to minimize its effects on the segmentation. The background is estimated by

creating an over-smoothed version of the image using an average filter. The size of the window is usually set to the width of the largest structure in the retina. In these images, the largest vessel's width is 60 pixels. The original image is divided by the filtered image. By using this technique, the non-uniformities in the fundus images are significantly reduced.

Following non-uniform illumination correction, we use our adaptive image enhancement method. The adaptive approach is iterative as depicted in Fig. 6.3. It consists of contrast limited adaptive histogram equalization (CLAHE, with clip limit of 0.01, [214]) followed by anisotropic diffusion [227] (12 iterations), and a feedback loop that is used to decide the number of times that we need to repeat the operation. In what follows, we describe all the components of the approach and then use an example to demonstrate how it works.

Let $I_S(x, y)$ be the subimage of $I(x, y)$ located in region S. Let T be the pre-processing operator. A region S being pre-processed i consecutive times is said to have undergone an i-th level of enhancement and is represented as $T^{(i)}[I_S(x, y)]$. The correct level of enhancement for each region is based on the comparison of the segmentation of two consecutive levels of enhancement, as represented by the enhancement control block in Fig. 6.3.

The comparison of the segmentation of two consecutive levels of enhancement is estimated as follows. Let U be the segmentation operator and $|\cdot|$ denote the cardinality operator, that is, the function that counts the number of nonzero values of the input argument. Then the difference of the segmentation of two consecutive levels of enhancement of $I_S(x, y)$ is given by

$$g(x, y) = U\left[T^{(i+1)}[I_S(x, y)]\right] - U\left[T^{(i)}[I_S(x, y)]\right], \tag{6.1}$$

and the number of nonzero pixels on region S is defined by $|g(x, y)|$.

Two assumptions were made in order to estimate the best enhancement level based on $g(x, y)$. If the number of new pixels obtained by the segmentation of the last level $(i+1)$ is high and these pixels are spatially distributed in the window, then we assume that the enhancement achieved on this last level has only added non-vessel pixels. On the other hand, if few new pixels are detected by the segmentation of the last level, it can be concluded that this level has not provided new significant information. By taking into account these two assumptions, three parameters that quantitatively define the aforementioned concepts were empirically set for the adaptive vessel segmentation algorithm as follows.

Let N be the number of pixels on a window. If $|g(x, y)|$ is in the range $[N \times frac_{lo}, N \times frac_{up}]$ and it has at least one connected component composed of $frac_{min} \times N$ pixels, level $i+1$ is preserved and the window undergoes another enhancement level. Otherwise, level i is selected as the optimal enhancement level for the analyzed region.

The parameters $frac_{lo}$ and $frac_{up}$ represent fractions of the total number of pixels that define the lower and upper bounds of the number of pixels that should be added by the segmentation of level $i+1$ for it not to be discarded, while $frac_{min}$ quantifies the spread criterion by establishing a lower bound to the number of pixels needed for a connected component to be considered significant. If one or more connected components are found, then the pixels added by the segmentation of level $i+1$ are not considered to be

too spread. In our study, we set $frac_{lo} = 0.05$, $frac_{up} = 0.10$ and $frac_{min} = 0.01$. Since we use 200x200-pixel windows, $N = 40000$.

The adaptive approach is demonstrated with segmentation corresponding to three different levels of enhancement of a given region shown in Fig. 6.4. The first enhancement level does not produce complete segmentation of vessels. By applying the second enhancement level, an adequate segmentation with less noise is achieved. The third level introduces more noise than relevant vessel segmentation.

The procedure is repeated for all the windows that cover the image. These regions are overlapped by shifting 50 pixels on both the vertical and horizontal axes.
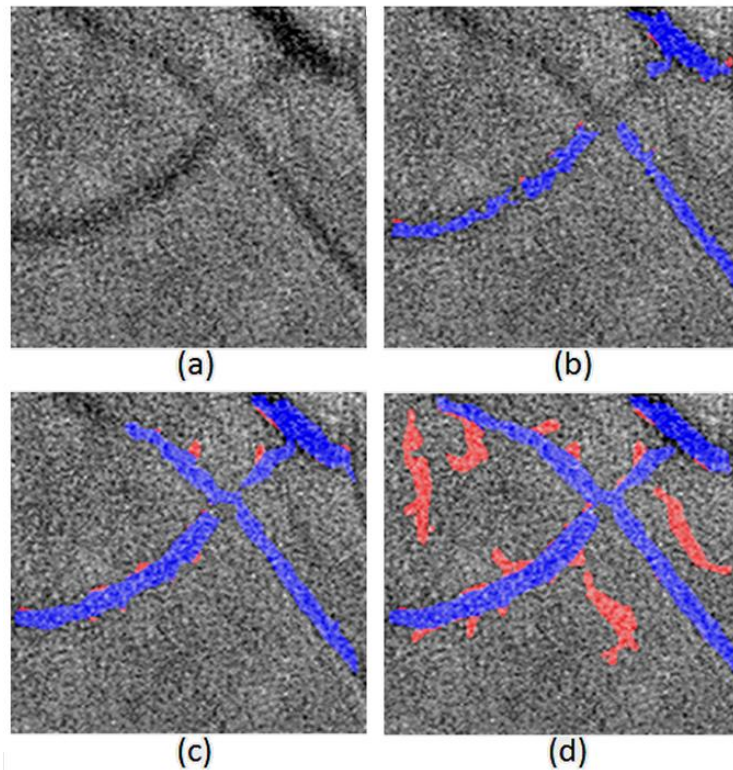

Figure 6.4 Segmentation of vessels for the ROI in (a) at 3 consecutive levels of enhancement: b) level 1 c) level 2, and d) level 3. Color code: correctly segmented vessels in blue, incorrect segmentation in red.

6.3.2 Amplitude-Modulation Frequency-Modulation (AM-FM)

See section 3.1.2 for more detail of AM-FM and its estimates. In terms of extracting textural features from each component, we are interested in using the instantaneous amplitude (IA) and the magnitude and angle of instantaneous frequency (IF). The IF angle is defined using:

$$IFangle = arctan\left(\frac{IF_y}{IF_x}\right) \tag{6.2}$$

The IA measures local image smooth variations, while the IF measures local frequency content. The magnitude of IF is rotation invariant and also measures the geometry of the texture. For example, the most appropriate scale to detect a pattern of vessels is the one that captures frequencies with a period that is proportional to their width.

In what follows, we will show that the IF angle can be associated with the level of tortuosity of the segmented vessels. Given the ambiguity in the estimation of the phase, $\cos \varphi_n(x, y) = \cos(-\varphi_n(x, y))$, our estimation is restricted to angles from 0 to 180. Fig. 6.5a shows synthetic curves with different levels of tortuosity. In this synthetic experiment, we use the AM-FM features from a frequency scale that captures the information of the three curves shown in Fig. 6.5b. The cumulative distribution function (CDF) of the masked IF angle content of the three curves (Fig. 6.5d) is shown in Fig. 6.6. Theoretically, most of the pixels of the straight curve will have angles near 0 and 180; this can be seen in the abrupt slope of the CDF for angles close to zero. A higher level of tortuosity implies more variability in the pixels' angle values. In Fig. 6.6, it can be seen that the CDF of the Level 1 tortuous curve rises more slowly than the CDF of the straight curve. Even slower is the rise of the CDF of the Level 2 tortuous curve due to the

presence of more angle values in its IF angle pixels. These observations support the use of the IF angle in tortuosity detection.

AM-FM components are extracted from different frequency scales. We consider the use of 31 bandpass channel filters associated with five frequency scales. These correspond to the following bands of frequencies: High (H), Medium (M), Low (L), Very Low (VL), Ultra Low (U), and the Lowpass Filter (LPF). We merged the frequency bands into 12 different Combinations of Scales (CoS), as shown in Table 6.1. We estimate a single AM-FM component for each CoS using Dominant Component Analysis [1]. A total of 36 different AM-FM representations (3 estimates x 12 CoS) are obtained for each image.
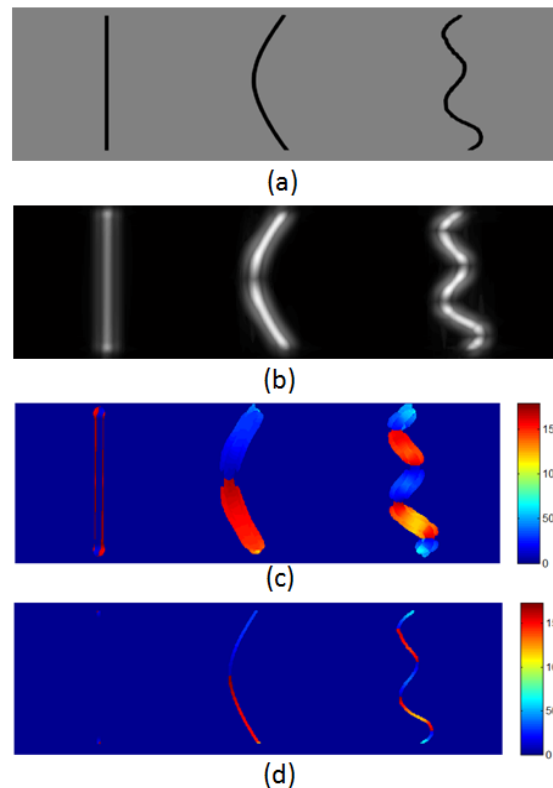
Figure 6.5 a) Synthetic vessels: (left) straight curve, (middle) Level 1 tortuous curve, (right) Level 2 tortuous curve. b) IA response of (a). c) IFangle of (a) constrained to high IA values for better visualization. d) Masked response of the IF angle in the synthetic vessels.
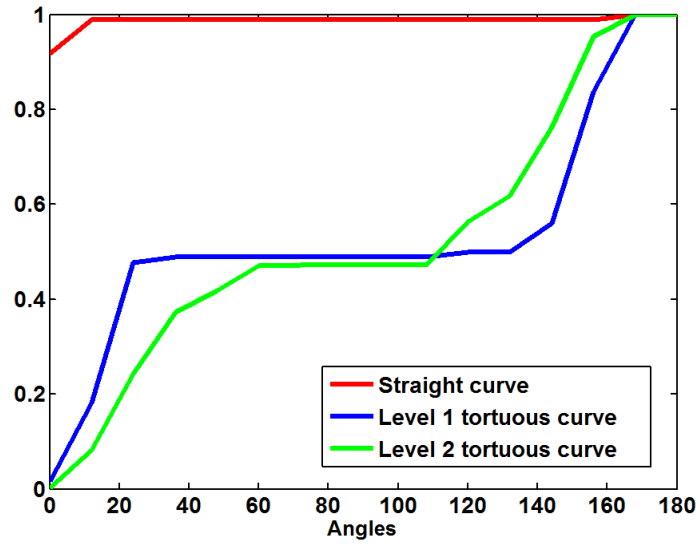
Figure 6.6 CDF distribution of the IFangle in the segmented curves for the three different types of curves shown in Fig. 6.5a.

Table 6.1 Combinations Of Scales for the Multiscale AM-FM analysis.

Combination Number	Frequency Bands	Range in mm
1	All – LPF	0.008 to 0.022
2	LPF	0.256 to inf.
3	VL	0.064 to 0.176
4	L	0.032 to 0.088
5	M	0.016 to 0.044
6	All	0.008 to inf.
7	LPF + U	0.128 to inf.
8	VL + U	0.064 to 0.352
9	L + VL	0.032 to 0.176
10	M + L	0.016 to 0.088
11	H + M	0.008 to 0.044
12	H	0.008 to 0.022

Once the 36 AM-FM representations are estimated, these are masked by the map of segmented vessels. For each masked image, a normalized histogram of 32 bins is

calculated. The values associated with these bins represent the features extracted from AM-FM.

6.3.3 Granulometry

The size distribution of the segmented vessels and NVD can be described using a morphological granulometry [79], which provides a multiscale approach that can be used to describe vessels of different sizes.

Granulometry is computed using a series of morphological opening operations (γ) with a structuring element (B) of different sizes (controlled by r). An opening is defined in terms of an erosion (ε) followed by dilation (δ) as given by:

$$\gamma(X) = \delta^{rB}\lfloor \varepsilon^{rB}(x) \rfloor \qquad (6.3)$$

When the size of the structural element is increased, objects of corresponding size and smaller in the binary image are eliminated. By subtracting the result of the opening from the original image, we can obtain only the objects that were removed by the opening. In this way, we can construct a distribution G by changing the r as specified below.

$$G(r) = \frac{Area(X) - Area(\gamma^{rB}(X))}{Area(X)}. \qquad (6.4)$$

Using this approach, we can compute the granulometry for the segmented vasculature. To provide for anisotropic measurements, we use a disk-shaped structural element of radii ranging consecutively from 1 to 32 pixels.
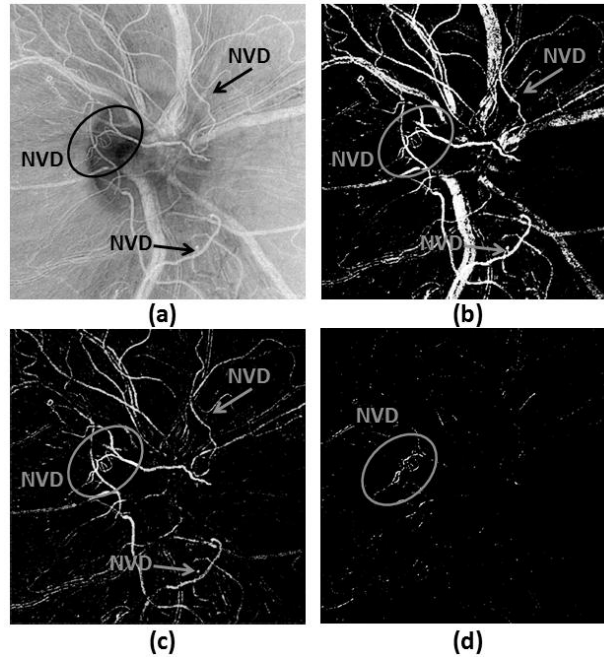
Figure 6.7 Examples of the difference between the inverse green channel image in (a) and its openings with r = 20 in (b), r=5 in (c), and r=2 in (d). These images show how vessels of different calibers are extracted by changing the radius. This provides information that is independent from the vasculature binary map.

Different openings were applied to the negative of the green channel (as shown in Fig. 6.7a), providing pixels with different intensities. Instead of counting the number of pixels, the mean value in the segmented vessels area is calculated. By using openings, objects of high intensity values are removed according to the size of structural elements. Fig. 6.7 shows three examples of the different outputs extracted from one image after using different sizes of structural elements. The example demonstrates the multiscale properties of the morphological granulometry.

6.3.4 Fractal Dimension

Fractal dimensions are computed to measure vascular changes associated with the multiscale, granulometric decomposition. For this approach, we generate 32 binary

images from the outputs of the difference in openings of consecutive radii, as explained in the previous section. Each binary image is skeletonized and used in computing the fractal dimension.

Our approach is motivated by the earlier use of fractal analysis in [228]. To determine the fractal dimension, we use box counting on the skeletonized vessels as described in [229]. Box counting covers the skeleton image with boxes of increasing size (2^n) where the maximum-sized box covers the whole analyzed area, which in this case is composed of 1024 pixels. For each box size, the number of boxes (N) that contains at least one pixel of the skeleton images is counted. To obtain the fractal dimension (D_f), we calculate the slope of the best fit line to the plot of $\ln(N)$ $vs.$ $n * \ln(2)$

6.3.5 Classification

A total of 39 features were obtained with the methods described in the previous sections. Thirty-six features come from the histograms of the AM-FM features constrained to the segmented vessels. The size distribution of the segmented vessels obtained with the granulometry computation provided one more set of features. Another set of features was calculated by estimating the mean value in the segmented vessels area after obtaining the difference between openings in the negative of the green channel of the fundus image. The last feature was calculated using the fractal dimension of the 32 images obtained from the granulometry process (Section C). As it was explained in the Section C, each feature is composed of 32 elements. Therefore, each ROI is represented by a feature vector of 1248 elements. Features are standardized prior to being input to the classifier to have zero mean and a standard deviation of one ($\bar{x} = 0, \text{SD} = 1$).

The classifier used to predict the presence of NVD in the optic disc is a support vector machine (SVM) with a linear kernel and a soft margin parameter $C = 1$ [230].

In order to validate our results, we used stratified *k*-fold cross-validation by maintaining the same ratio of NVD and normal cases on each fold. The choice of *k* depends upon the amount of available data. If the number of cases is small, then leave-one-out cross-validation, where the number of folds equals the number of cases, is the method of choice. This allows the classifier to be trained on as much data as possible. However, the classification accuracy estimate, although nearly unbiased, has high variance, since the training sets are very similar to each other. When a relatively large number of cases are available (which is the case in this study), the bias of the cross-validation estimate is reduced, making it safe to reduce the number of folds. Generally, it is advised to use 10-fold cross-validation in these scenarios [231].

6.4 Results & Discussion

6.4.1 Adaptive Vessel Segmentation

In order to confirm that our adaptive vessel segmentation was able to capture most of the neovascularization, a certified retinal reader marked all the new vessels in 25% of our cases with NVD (25 images). The results of our segmentation cover 80% of all the new vessels. Fig. 6.8 shows a comparison with the global approach in an optic disc with neovascularization.
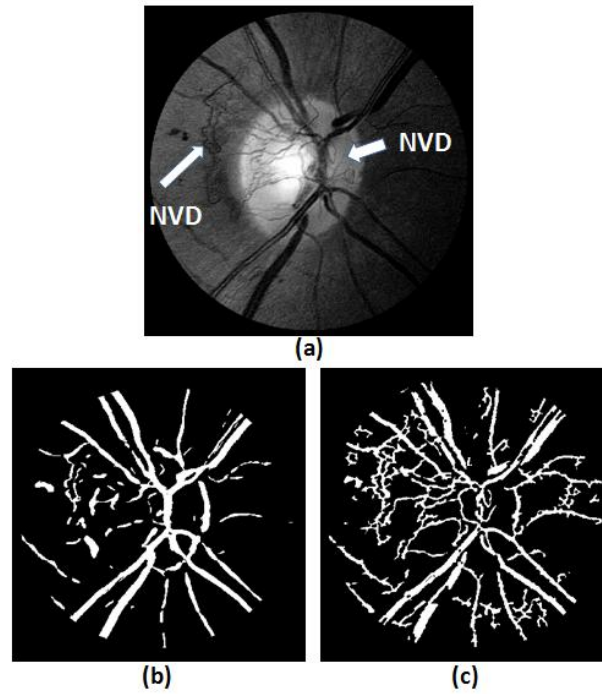
Figure 6.8 Comparison of the segmentation of vessels in (a) using the global approach (b) and the adaptive approach (c). It can be seen that the NVD is captured more accurately with the proposed segmentation approach.

6.4.2 Amplitude-Modulation Frequency-Modulation (AM-FM)

In Fig. 6.9, we show the response of the IA using CoS 11 (see Table 6.1) for an image with NVD. In Fig 6.9c we can observe how the vessels with small caliber (most of them being neovascularization) are characterized by high intensity. In order to analyze the IA reponse for different structures, we masked the content of three groups, background, normal vessels, and neovascularization, by using the annotated image in Fig 6.9b. In the histograms presented in Fig 6.9d, the difference between the number of pixels of NVD and normal vessels increases for high values of IA. Even though the background presents more pixels than normal vessels in that range, there is a significant difference with respect to the NVD histogram. And since we only analyzed the segmented vessel regions

by using the adaptive vessel segmentation, the contribution of the background is significantly reduced.
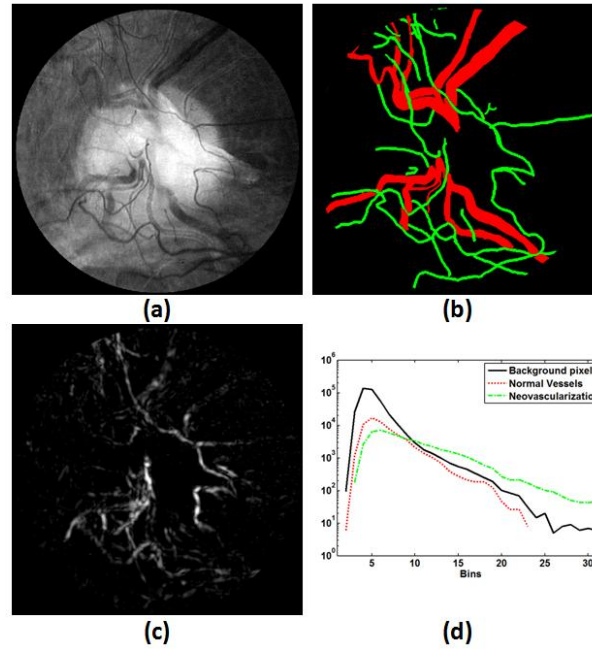
Figure 6.9 AM-FM representation of an image with NVD. a) Original image. b) Manually segmented vessel map (NVD in green). c) IA of (a) using high+medium frequencies. d) Normalized histogram of the content of (c) for background, normal vessels, and NVD. These histograms show that a larger amount of pixels with NVD compared to normal vessels will be located at high values of IA.
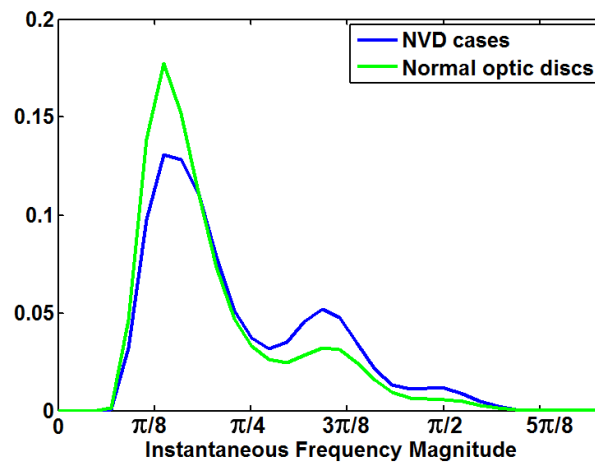
Figure 6.10 Comparison of the mean of normalized histograms of the IFm of CoS 11 for 100 NVD and 100 normal cases. The instantaneous frequency magnitude is displayed in radians (see Table I for correspondence to the physical dimensions).

Fig. 6.10 shows the average of the normalized histograms of one AM-FM representation (the magnitude of the IF – CoS 11) for NVD and normal cases in our dataset. It can be seen that NVD cases have more pixels at higher frequencies than the normal cases. This indicates that the magnitude of IF is also an informative feature that can help differentiate between normal and NVD cases.

6.4.3 Granulometry

Fig. 6.11 shows the differences between the distributions of the two groups for the first eight different radii (r=1 to 8). A two-sample *t*-test was computed for each, and the largest *p*-value was 0.0092 for radius = 6, which indicates that the means of the distributions for each radius of NVD and normal cases are statistically different. This suggests that there are more small objects (thin vessels) in NVD cases than on normal optic discs.
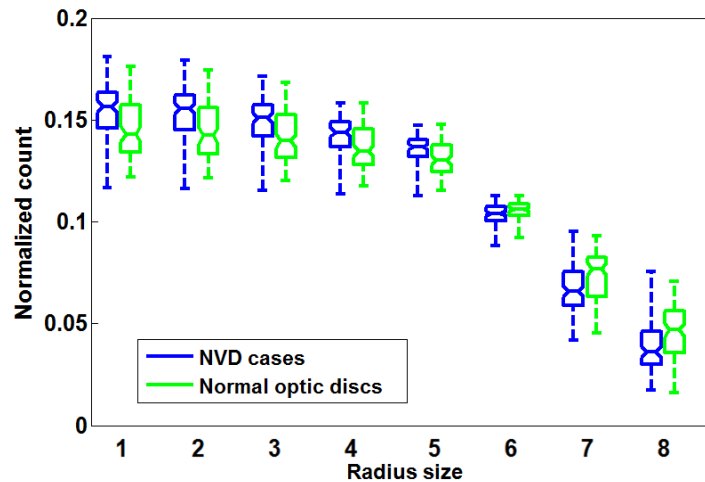
Figure 6.11 Size distribution of granulometry in the segmented vessels using a disk-shaped structural element with a radius from 1 to 8 pixels.

6.4.4 Fractal Dimension

In theory, as the retinal structure increases in complexity, the value of the fractal dimension is higher. It has already been noted that NVD adds more complexity to the vasculature, due to the convoluted spatial distribution and tortuosity of the new vessels. For this reason, NVD should have a higher fractal dimension than normal vasculature. This statement is supported by the results shown in the boxplots in Fig. 6.12, where the first eight extracted features for fractal dimension for NVD and normal cases are shown. We also performed the two sample t-test for the distributions in each radius, as was done for granulometry. The maximum obtained p-value was 1.791×10^{-5}. This suggests that there is a significant difference between the means of the distributions of the two groups.
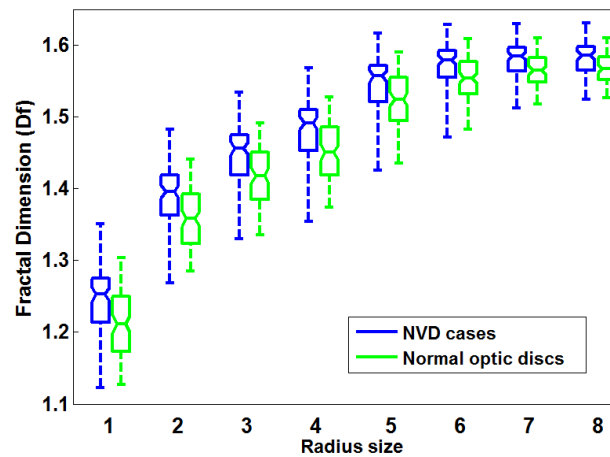
Figure 6.12 Boxplot of the values of fractal dimension for each class (NVD, normal) for eight different levels of granulometry.

6.4.5 Classification

We tested our system using 300 images (100 NVD, 200 normal) and 10-fold cross-validation. An AUC of 0.93 was obtained for the classification of NVD vs. normal cases. The classifier achieved a maximum accuracy of 88%. This point corresponds to

sensitivity equal to 78% and specificity of 94%. Other points in the ROC curve (see Fig. 6.13) gave us sens/spec = 92%/73%, and 95%/68%.
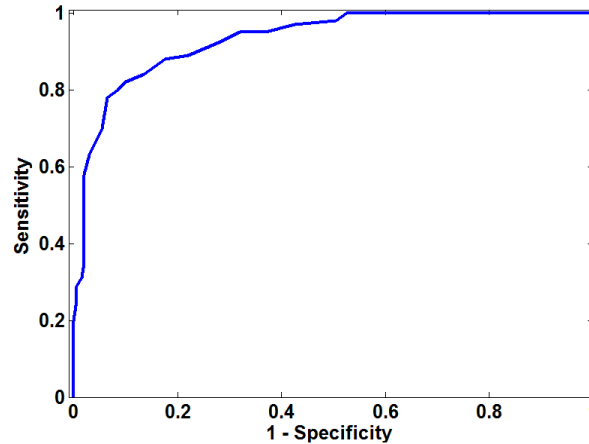
Figure 6.13 ROC curve of the classification of NVD cases.

In Figs. 6.14 and 6.15 we analyze two misclassified cases, one false positive (FP) and one false negative (FN). In Fig. 6.16 we present a challenging NVD case that was correctly detected. The FP case in Fig. 6.14a presents thin vessels with some degree of tortuosity, which are usually characteristic of NVD. By analyzing the results of the adaptive vessel segmentation shown in Fig. 6.14b, we confirm that we are extracting features from these vessels. However, these are just normal vessels that follow a pattern similar to NVD.

Fig. 6.15 shows the FN case. The highlighted regions of Fig. 6.15a show NVD present on this image. It can be seen that the spatial extent of these vessels is very small. In fact, only one of them is captured by our segmentation procedure (Fig. 6.15b). This case demonstrates very subtle NVD which would take a robust ophthalmic evaluation to detect. On the other hand, Fig. 6.16 presents a case with subtle NVD that was correctly classified. The main difference with respect to the FN case is that there are more regions

with NVD. Therefore, the adaptive vessel segmentation approach has a greater chance of capturing them.
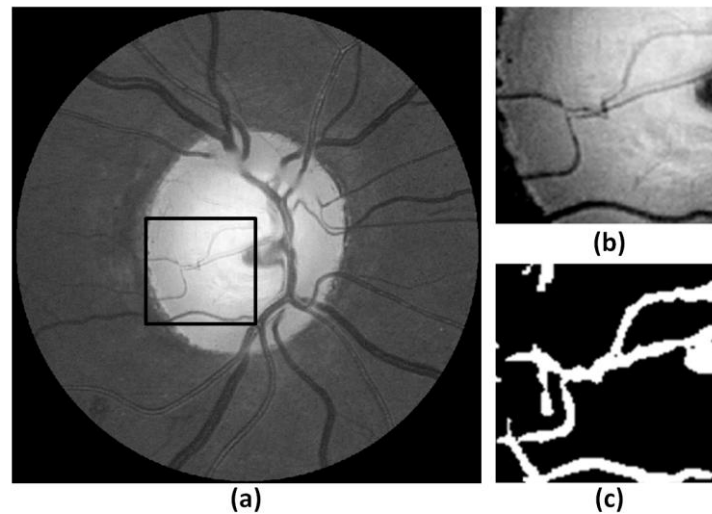
Figure 6.14 Example of a false positive. a) Original image. b) Zoom-in of the black box in the optic disc image. b) Segmentation of (a) obtained with the adaptive vessels segmentation algorithm.
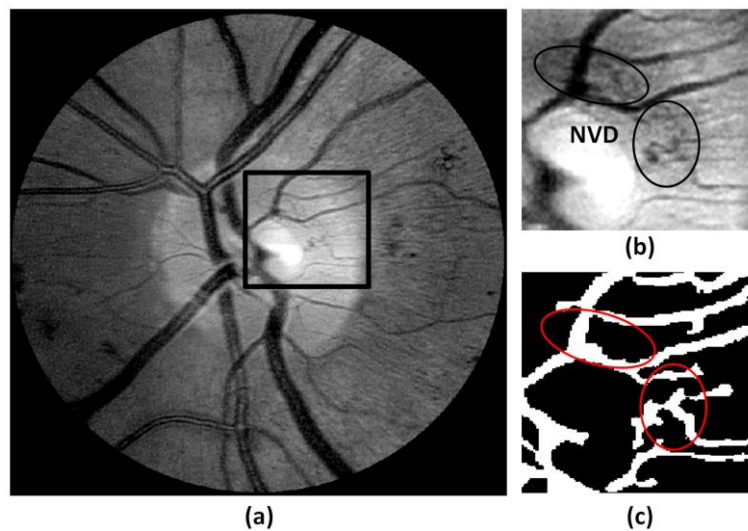
Figure 6.15 Example of a false negative. a) Original image. b) Zoom-in of the black box in the optic disc image. b) Segmentation of (a) obtained with the adaptive vessels segmentation algorithm.
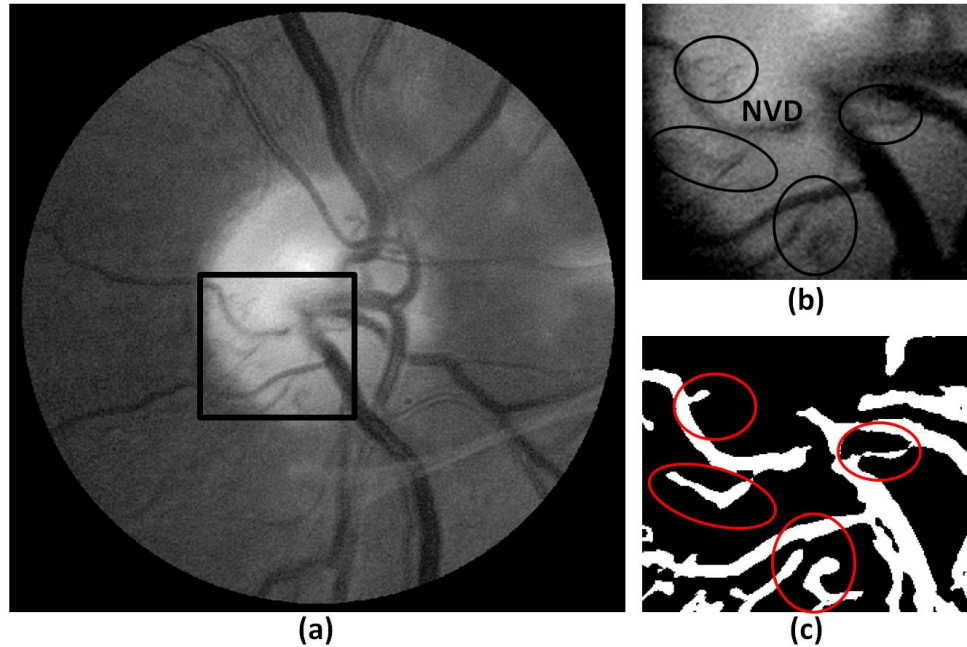
Figure 6.16 Example of a true positive. a) Original image. b) Zoom-in of the black box in the optic disc image. b) Segmentation of (a) obtained with the adaptive vessels segmentation algorithm.

6.5 Conclusions

This chapter presents a novel methodology for the detection of neovascularization in the optic disc. The focus of this method is not to characterize segments of the vasculature as performed by Goatman et al. in [104]. Instead, we characterize the vasculature as normal or abnormal. The proposed adaptive vessel segmentation method adequately detects neovascularization, allowing us to correctly extract features of these structures, thus minimizing the inclusion of spurious information from other structures in the retina.

By combining an adaptive vessel segmentation approach with the features extracted using AM-FM, granulometry, and spatial information with fractal dimensionality, we have improved upon previous results presented in the automatic classification of NVD [104]. The significance of these results is supported by the fact that we used a medium-scale database composed of 300 images, achieving a high generalization capacity.

This method can be further improved by optimizing empirically set parameters, the adaptive vessel segmentation iteration, and feature selection.

This system can be used in conjunction with an automatic DR screening algorithm to ensure that no sight-threatening conditions due to neovascularization are missed.

Chapter 7: Concluding Remarks, Future Work, and Recommendations

7.1 Concluding remarks

The DR screening system presented in this dissertation was one of the first published top-down approaches. In the recent literature, we observe that there is a new trend to implement top-down approaches. This most-likely motivated by our approach and the flexibility of top-down approaches to capture different abnormalities using the same method.

The main algorithm to detect DR, which was described in chapter 3, detects non-proliferative state of DR (presence of microaneurysms, hemorrhages, or hard exudates away from the fovea) with a performance comparable to or better than the ones presented by the larger studies in the field described in chapter 2.

An advantage of our top-down approach is clearly shown in the detection of abnormalities related to AMD. Although the system was not originally intended to detect those abnormalities, by adding AMD cases to the training database we were able to screen for these lesions with relatively high accuracy.

A computer-aided detection algorithm based on a generalized optimization scheme of image decompositions was presented in Chapter 4 for the detection of exudates and red lesions in the macula. Given its optimization process and its flexibility, this methodology could be extended to the detection of different types of lesions.

Chapter 5 presents an improved version of the algorithm developed in chapter 4. This was devised due to the high significance of detecting exudates in the macula. The

algorithm showed robustness, since it did not require retraining when it was tested with a second dataset. Instead of using contrast enhancement methods that may increase the noise level in the images or using classification to perform candidates' extraction, this system provides a reliable method for extraction of candidates using only the normalized output of the RGB color space.

A methodology for the detection of neovascularization in the optic disc is presented in chapter 6. The main contribution of this paper is the analysis of the entire vasculature in the optic disc to determine the presence of neovascularization, without the need to analyze each vessel segment independently, as other approaches do. The automatic detection of this pathology is novel, being our results better than the ones obtained by the only published paper that performs this task (2011).

This dissertation work presents viable and efficient means to characterize different retinal abnormalities and build binary classifiers for detection purposes. Although automatic detection of DR has been studied by different groups in the last decade, the classification accuracy results obtained with our proposed algorithms are very high, being considered the state-of art in DR screening systems. In addition, the combined classification performance results for STDR, neovascularization, pigmentation and geographic atrophy had not been previously achieved at the levels of performance presented in this dissertation work.

7.2 Future Work and Recommendations

In the research presented in chapters 3 to 6, the emphasis was in the detection of sight threatening pathologies. These algorithms gave good performance on limited data sets.

However, the number of people to be screened is very high, in the order of millions. Therefore, to establish the clinical relevance of the proposed algorithms, we would need to validate performance on a very large dataset. This is because the prevalence of sight threatening conditions is low. For example, a larger study presented in [192] used 33,535 patients to validate the DR screening algorithm. In the near future, given the increasing number of clinical screening research centers, an evaluation of this type will be possible.

Computer aided diagnosis systems are evaluated in terms of accuracy, sensitivity and specificity. In terms of clinical value, it will be interesting to consider the use of the predictive value to evaluate performance. The predictive value is a better clinical metric in the sense that it also considers the prevalence of the disease.

Appendix A

Related publications

This section lists published work related with the dissertation:

[1]   **Agurto C**, Murillo S, and Murray V et al. "Detection and Phenotyping of Retinal Disease using AM-FM Processing for Feature Extraction". *42nd IEEE Asilomar Conference on Signals, Systems and Computers*. 2008.

[2]   **Agurto C**, Pattichis MS, Murillo S et. al., "Detection of Structures in the Retina Using AM-FM for Diabetic Retinopathy Classification", ARVO. 2009.

[3]   Barriga ES, Murray V, **Agurto C** et al. "Multi-scale AM-FM for lesion phenotyping on age-related macular degeneration". *IEEE International Symposium on Computer-Based Medical Systems*. 2009.

[4]   **Agurto C**, Murray V, Barriga E, Murillo S, Pattichis MS, Davis H, Russell S, Abramoff MD and Soliz P, Multiscale AM-FM Methods for Diabetic Retinopathy Lesion Detection, *IEEE Transactions on Medical Imaging*. 2010; 29(2): 502-512.

[5]   **Agurto C**, Barriga S, Murray V, Pattichis M, Davis B, Soliz P. "Effects of Image Compression and Degradation on an Automated Diabetic Retinopathy Screening Algorithm". *SPIE Medical Imaging*. 2010.

[6]   Barriga ES, Murray V, **Agurto C** et al. "Automatic System for Diabetic Retinopathy Screening Based on AM-FM, Partial Least Squares, and Support Vector Machines". *IEEE International Symposium on Biomedical Imaging*. 2010.

[7]   **Agurto C**, Barriga S, Murray V, Pattichis M, Zamora G, and Soliz P, "Toward comprehensive detection of sight threatening retinal disease using a multiscale AM-FM methodology". *SPIE Medical Imaging*. 2011.

[8]   Yu H, Barriga S, **Agurto C**, et al., "Fast localization of optic disc and fovea in retinal images for eye disease screening", *SPIE Medical Imaging*. 2011.

[9]   **Agurto C**, Barriga S, Zamora G et al., "Automatic Screening of Eye diseases using 3-Field Fundus Photographs", *ARVO.* 2011.

[10]   Yu H, **Agurto C**, Barriga S, Bauman W, Soliz P and Zamora G, "Computer-Aided Screening of Cardiovascular Disease based on retinal imaging: Results using Retinal Vasculature Features", *ARVO.* 2011.

[11]   **C Agurto,** ES Barriga, V Murray, S Nemeth, R Crammer, W Bauman, G Zamora, MS Pattichis, and P Soliz, "Automatic detection of diabetic retinopathy and age-related macular degeneration in digital fundus images," Investigative Ophthalmology & Visual Science, 2011, vol. 52, no. 8, pp. 5862– 5871.

[12]   H Yu, S Barriga, **C Agurto,** G Zamora, W Bauman and P Soliz, "Fast Vessel Segmentation in Retinal Images Using Multiscale Enhancement and Second-order Local Entropy", Proc. SPIE 8315, 83151B (2012)

[13]   **C Agurto**, H Yu, ES Barriga, V Murray, MS Pattichis, S Nemeth, and P Soliz, "Detection of Hard Exudates in the Macula using a Generalized Optimization Scheme", ARVO, 2012

[14]   S Barriga, V Murray, **C Agurto**, G Zamora, H Yu, J C. Wigdahl, S C. Nemeth, W. C. Bauman, P Soliz," Statistical Validation Of An Automatic Algorithm For Diabetic Retinopathy Screening", ARVO, 2012

[15]   **C Agurto**, H Yu, V Murray, M Pattichis, S Barriga, P Soliz, "Detection of Hard Exudates and Red Lesions in the Macula Using a Multiscale Approach", accepted to IEEE Southwest Symposium on Image Analysis and Interpretation, 1043, 2012.

[16]   H Yu, **C Agurto,** S Barriga, SC Nemeth, P Soliz, and G Zamora, " Automated image quality evaluation of retinal fundus photographs in diabetic retinopathy screening", accepted to IEEE Southwest Symposium on Image Analysis and Interpretation, 1037, 2012.

[17]   H. Yu, E. S. Barriga, **C. Agurto**, S. Echegaray, M. S. Pattichis, W. Bauman and P. Soliz, "Fast Localization and Segmentation of Optic Disk in Retinal Images Using Directional Matched Filtering and Level Sets," *IEEE Transactions on Information Technology in Biomedicine,* vol. 16, no. 4, pp. 644-657, 2012.

[18]   **C Agurto**, H Yu, V Murray, MS Pattichis, W Bauman, S Barriga, and P Soliz, " Detection of Neovascularization in the Optic Disc Using An AM-FM Representation, Granulometry, and Vessel Segmentation", accepted to *34th Annual International IEEE EMBS Conference*, 2012.

[19]   V Murray, C Agurto, S Barriga, MS Pattichis, and P Soliz, "Real-time Diabetic Retinopathy Patient Screening using Multiscale AM-FM Methods," accepted to *IEEE International Conference on Image Processing* (ICIP), 2012.

References

[1]   J. D. Cavallerano, L. P. Aiello, A. A. Cavallerano and et al., "Nonmydriatic digital imaging alternative for annual retinal examination in persons with previously documented no or mild diabetic retinopathy," *Am J Ophthalmol,* vol. 140, no. 4, pp. 667-673, 2005.

[2]   V. Murray, P. Rodriguez and M. Pattichis, "Multi-scale AM-FM Demodulation and Reconstruction Methods with Improved Accuracy," *IEEE Transactions on Image Processing,* vol. 19, no. 5, pp. 1138-1152, 2010.

[3]   United Health Center for Health Reform and Modernization, Minnetonka, MN, "The United States of Diabetes: Challenges and Oportunities in the decade ahead," 2010.   [Online].   Available: http://www.unitedhealthgroup.com/main/HealthReform.aspx.

[4]   X. Zhang, J. B. Saaddine, C. F. Chou and et al., " Prevalence of Diabetic Retinopathy in the United States 2005-2008," *JAMA,* vol. 304, no. 6, pp. 649-656, 2010.

[5]   J. H. Kempen, B. J. O'Colmain, M. Leske and et al., "The prevalence of diabetic retinopathy among adults in the United States," *Arch. Ophthalmol,* vol. 122, pp. 552-563, 2004.

[6]   G. S. Scotland, P. McNamee and A. D. Fleming, "Cost and consequences of automated algorithms versus manual grading or the detection of referable diabetic retinopathy," *Br. J. Ophthalmol. ,* vol. 94, pp. 712-719, 2010.

[7]   A. Hutchinson, A. McIntosh, J. Peters and et al., "Effectiveness of screening and monitorig test for diabetic retinopathy-a systematic review," *Diabet. Med.,* vol. 17, pp. 495-506, 2000.

[8]   C. S. Arun, A. Bermani, K. Stannard and et al., "Long-term impact of retinal screening on significant diabetes-related visual impairment in the working age population," *Diabet. Med.,* vol. 26, pp. 489-492, 2009.

[9]   G. M. Zoega, T. Gunnarsdottir, S. Bjornsdottir and et al., "screening compliance

and visual outcome in diabetes," *Acta Ophthalmol,* vol. 83, pp. 687-690, 2005.

[10] L. Garvican, J. Clowes and T. Gillow, "Preservation of sight in diabetes: developing a national risk reduction programme," *Diabet. Med.,* vol. 17, pp. 627-634, 2000.

[11] J. T. Gillow and J. A. Gray, "The National Screening Committee Review of Diabetc Retinopathy Screening," *Eye,* vol. 15, pp. 1-2, 2001.

[12] "The Eye and Vision," [Online]. Available: http://www.virtualmedicalcentre.com/anatomy/the-eye-and-vision/28.

[13] T. A. I. Furness and et al., "A Virtual Retinal Display (for Virtual World Generation)," *a proposal submitted to National Institute of Standards and Technology Advanced Technology Program,* 1990.

[14] R. G. Michels, C. P. Wilkinson and T. A. Rice, "Retinal detachment. p 17. The C.V. Mosby Company," 1990.

[15] N. M. Sing, S. F. Anderson and J. C. Townsend, "The normal optic nerve head," *Optom. Vis. Sci.,* vol. 77, pp. 293-301, 2000.

[16] American Diabetes Association, "Standards of Medical Care in Diabetes-2012," *Diabetes Care,* vol. 35, no. 1, pp. S11-S63, 2012.

[17] "International Diabetes Federation Diabetes Atlas. Fifth Ed.," 2009. [Online]. Available: http://www.diabetesatlas.org/content/regional-data.

[18] R. Klein, "Hyperglycemia and Microvascular and Macrovascular Diseases in Diabetes," *Diabetes Care,* vol. 18, pp. 258-268, 1995.

[19] v. J. Spalton, R. A. Hitchings and P. A. Hunter, Atlas of Clinical Ophthalmology, Philadelphia: Elsevier Mosby, 2005.

[20] "National Eye Institute," [Online]. Available: http://www.nei.nih.gov/health/examples/.

[21] R. Klein, B. E. Klein, S. E. Moss, N. A., N. A., N. A. and N. A, "'The wisconsin epidemiologic study of diabetic retinopathy: III. Prevalence and risk of diabetic retinopathy when age diagnosis is 30 or more years," *Arch Ophthalmol.,* vol. 67, 1984.

[22] L. Yanko, U. Golbourt, I. Michaelson and et al., "Prevalence and 15 year incidence of retinopathy and associated characteristics in middle age and eldery diabetic men," *BRr Opthalmol.,* vol. 67, 1984.

[23] "The diabetes control and complications trial research group, the effect of intensive treatment of diabetes on the development and progression of long term complications in insulin-dependent diabetes mellitus," *N Engl J Med, 329,977,* 1993.

[24] "UK prospective diabetes study (UKPDS) Group, Intensive blood-glucose control with sulphonylureas or insulin compared with conventional treatments and risk of complications in patients with type 2 diabetes (UKPDS 33), Lancet, 352, 837.," 1998.

[25] C. Hasslacher, A. Bosted–Kiesel and H. P. Kempe, "Effect of metabolic factors and blood pressure on kidney function in proteinuric type II (non-insulin- dependent) diabetic patients," *Diabetologia, 36,1051,* 1993.

[26] F. H. Jelinek and M. J. Cree., Automated image detection of retinal pathology, Boca Raton: CRC Press, 2010.

[27] T. Teng, M. Lefley and D. Claremont, "Progress towards automated diabetic ocular screening: a review of image analysis and intelligent systems for diabetic retinopathy," *Med. & Biological Engineering & Computing,* vol. 40, pp. 2-13, 2002.

[28] M. Tidwell, *Master of Science in Electrical Engineering University of Washington 1995: A Virtual Retinal Display For Augmenting Ambient Visual Environments.,* 1995.

[29] B. M. M. C. &. C. M. B. M. a. M. Alastair Atkinson, "Imaged Area of the Retina".

[30] "Modified 7-standard field color fundus photography (7M-F) and film fluorescein angiography (FA-F)," Madison, WI: University of Wisconsin-Madison Fundus Photograph Reading Center, 2009. [Online]. Available: http://eyephoto.ophth.wisc.edu/Photography/Protocols/Mod7.

[31] S. Vujosevic, E. Benetti, F. Massignan and et al., "Screening for diabetic

retinopathy: 1 and 3 nonmydriatic 45-degree digital fundusphotographs vs. 7 standard early treatment diabetic ertinopathy study fields," *Am. J. Opthalmol.,* vol. 148, 2009.

[32] R. Klein, S. Moss, B. Klein, M. Davis and D. Demets, "The wisconsin epidemiologic study of diabetic retinopathy: xi the incidence of macular edema," *Ophthalmology,* no. 96, p. 1501–1510, 1989.

[33] B. Liesenfeld, E. Kohner, W. Piehlmeier and et al., "A telemedical approach to the screening of diabetic retinopathy: digital fundus photography," *Diabetes Care,* no. 23, pp. 345-348, 2000.

[34] P. H. Scanlon, R. Malhotra, R. H. Greenwood and et al., "Comparison of two reference standards in validating two field mydriatic digital photography as a method of screening for diabetic retinopathy," *Br J Ophthalmol. ,* vol. 87, p. 1258–1263, 2003.

[35] S. Philip, L. Cowie and J. A. Olson, "The impact of the Health Technology Board for Scotland's grading model on referrals to ophthalmology," *Br J Ophthalmol. ,* vol. 89, p. 891–896., 2005.

[36] I. Zimmer-Galler and R. Zeimer, "Results of Implementation of the DigiScope for Diabetic Retinopathy Assessment in The Primary Care Environment," *Telemedicine and e -Health,* vol. 12, no. 2, pp. 89-98, 2006.

[37] K. A. Goatman, A. D. Whitwam, A. Manivannan, J. A. Olson and P. F. Sharp, "Colour normalisation of retinal images," *Proceedings of Medical Image Understanding and Analysis,* 2003.

[38] T. T. Berendschot, P. J. Delint and D. v. Norren, "Fundus reflectance-historical and present ideas," *Prog. Retin Eye Res ,* vol. 22, pp. 171-200, 2003.

[39] J. Conrath, A. Erginay, R. Giorgi, A. Lecleire-Collet, E. Vicaut, J. C. Klein, A. Gaudric and P. Massin, "Evaluation of the effect of JPEG and JPEG2000 image compression on the detection of diabetic retinopathy," *Eye ,* vol. 21, p. 487–493, 2007.

[40] S. C. Lee and Y. Wang, "Automatic retinal image quality assessment and

enhancement," *Proceedings of SPIE Medical Imaging Processing,* vol. 3661, pp. 1581-1590, 1999.

[41]   M. Lalonde, L. Gagon and M. C. Boucher, "Automatic visual quality assessment in optical fundus images," *Proceedings of Vision Interface 2001, Ottawa,* pp. 259-264, June 2001.

[42]   H. Davis, S. R. Russell, E. S. Barriga, M. D. Abramoff and P. Soliz, "Vision-based, real-time retinal image quality assessment," *CBMS 2009,* pp. 1-6, 2009.

[43]   D. B. Usher, M. Himaga, M. J. Dumskyj and et al., "Automated assessment of digital fundus image quality using detected vessel area," *Proceedings of Medical Image Understanding and Analysis. British Machine Vision Association (BMVA) Sheffield, UK:,* pp. 81-84, 2003.

[44]   A. D. Fleming, S. Philip, K. Goatman, J. Olson and P. Sharp, "Automated assessment of diabetic retinal Image quality based on clarity and field definition," *Invest. Ophthalmol. Vis. Sci. ,* vol. 47, pp. 1120-1125, 2006.

[45]   A. D. Fleming, S. Philip, K. A. Goatman, J. A. Olson and P. F. Sharp, "Automated assessment of retinal image field of view," *Proceedings of Medical Image Understanding and Analysis, London, UK: British Machine Vision Association (BMVA),* pp. 129-132, 2004.

[46]   M. Niemeijer, M. D. Abràmoff and B. v. Ginneken, "Image structure clustering for image quality verification of color retina images in diabetic retinopathy screening," *Med Image Anal. ,* vol. 10, no. 6, pp. 888-898, 2006.

[47]   "TECHNO-VISION Project, MESSIDOR: methods to evaluate segmentation and indexing techniques in the field of retinal ophthalmology," [Online]. Available: http://messidor.crihan.fr/.

[48]   L. Giancardo, M. D. Abràmoff, E. Chaum, T. P. Karnowski, F. Meriaudeau and K. W. Tobin, "Elliptical local vessel density: a fast and robust quality metric for retinal images," *Engineering in Medicine and Biology Society,* 2008.

[49]   J. Paulus, J. Meier, R. Bock, J. Hornegger and G. Michelson, "Automated quality assessment of retinal fundus photos," *International Journal of Computer Assisted*

Radiology and Surgery., vol. 5, no. 6, pp. 557-564, 2010.

[50] H. Yu, C. Agurto, S. Barriga, S. Nemeth, P. Soliz and G. Zamora, ""Automated image quality evaluation of retinal fundus photographs in diabetic retinopathy screening," *IEEE Southwest Symposium on Image Analysis and Interpretation (SSIAI), ,* pp. 125-128, 2012.

[51] H. Yu, S. Barriga, C. Agurto, G. Zamora, W. Bauman and P. Soliz, "Fast Vessel Segmentation in Retinal Images Using Multiscale Enhancement and Second-order Local Entropy," *SPIE medical imaging,* 2012.

[52] N. D. Narvekar and L. J. Karam, "A No-Reference Image Blur Metric Based on the Cumulative Probability of Blur Detection (CPBD)," *IEEE Transactions on Image Processing,* vol. 20, no. 9, pp. 2678-2683, 2011.

[53] R. J. Winder, P. J. Morrow, I. N. McRitchie, J. R. Baile and P. M. Hart, "Algorithms for digital image processing in diabetic retinopathy," *Computerized Medical Imaging and Graphics,* vol. 33, pp. 608-622, 2009.

[54] A. Hoover and M. Goldbaum, "Locating the optic nerve in the retinal image using the fuzzy convergence of the blood vessels," *IEEE Transactions on Medical Imaging,* vol. 22, pp. 951-958, 2003.

[55] F. t. Haar, *Automatic localization of the optic disc in digital colour images of the human retina. M.S. thesis, Utrecht University, Utrecht, The Netherlands.,* 2005.

[56] "STARE ProjectWebsite Clemson Univ., Clemson, SC," [Online]. Available: http://www.ces.clemson.edu~ahoover/stare.

[57] D. Tomazevic, B. Likar and F. Pernus, "A comparison of retrospective shading correction techniques," *in International Conference on Pattern Recognition,* vol. 3, pp. 564-567, 2000.

[58] H. Wang, W. Hsu, K. G. Goh and M. L. Lee., "An Effective approach to detect lesions in color retinal images," *IEEE conference on computer vision and patter recognition,* 2000.

[59] G. Yang, L. Gagnon, S. Wang and M. C. Boucher, "Algorithm for detecting micro-aneurysms in low-resolution color retinal images," *Proc. Vision Interface 2001,*

Ottawa, pp. 265-271, 2001.

[60] T. Spencer, J. A. Olson, K. C. McHardy, P. F. Sharp and J. V. Forrester, "An image-processing strategy for the segmentation and quantification of microaneurysms in fluorescein angiograms of the ocular fundus," *Computers and Biomedical Research ,* vol. 29, pp. 284-302, 1996.

[61] R. Jagoe, J. Arnold, C. Blauth, P. Smith, K.M.Taylor and R. Wootton, "Measurement of capillary dropout in retinal angiograms by computerised image analysis," *Pattern Recognition Letters,* vol. 13, pp. 143-151, 1992.

[62] N. P. Ward, S. Tomlinson and C. J. Taylor, "Image analysis of fundus photographs. The detection and measurement of exudates associated with diabetic retinopathy," *Ophthalmology,* vol. 96, pp. 80-86, 1989.

[63] G. E. Oien and P. Osnes, "Diabetic retinopathy: Automatic detection of early symptoms from retinal images," *in Proc. Norwegian Signal Process. Symp. ,* pp. 135-140, 1995.

[64] A. M. Mendoza and A. Campilho, "Segmentation of Retinal Blood vessels by combining the detecion of centerlines and Morphological Reconstruction," *IEEE Transaction on Medical Imaging,* vol. 25, no. 9.

[65] W. Vijay, K. Madisetti and B. Douglas, The Digital Signal Processing Handbook, CRC Press, ISBN 0-8493-8572-5, 1997.

[66] H. Narasimha, A. Can, B. Roysam, C. Stewart, H. Tanenbaum, A. Majerovics and H. Singh, "Automated Analysis of Longitudinal Changes in Color Retinal Fundus Images for Monitoring Diabetic Retinopathy," *IEEE Trans. on Biomedical Engineering,* vol. 52, pp. 1-33, 2005.

[67] K. Skifstad and R. Jain, "Illumination independent change detection from real world image sequences," *Comput. Vis. Graph. Image Process.,* vol. 46, pp. 387-399, 1989.

[68] M. Foracchia, E. Grisan and A. Ruggeri, "Luminosity and contrast normalization in retinal images," *Med Image Anal.,* vol. 3, pp. 179-190, 2005.

[69] M. Goldbaum, N. Katz and et al., "The Discrimination of Similar Colored Objects

in Computer Images of the Ocular Fundus," *Investigative Opthalmology & Visual Science,* vol. 31, no. 4, 1990.

[70] A. Sopharak, K. T. New, Y. A. Moe and et al., "Automatic Exudates Detection with a Naive Bayes Classifier," *In Proceedings of the 2008 International Conference on Embedded Systems and Intelligent Technology,* pp. 139-142, 2008.

[71] A. Osareh, M. Mirmehdi, B. Thomas and et al., "Classification and localisation of diabetic-related eye disease," *Proceedings of the European Conference on Computer Vision ,* pp. 502-516, 2002.

[72] D. S. Shin, N. B. Javornik and J. W. Berger, "Computer-assisted, interactive fundus image processing for macular drusen quantitation," *Ophthalmology - 1 June 1999 ,* vol. 106, no. 6, pp. 1119-1125, 1999.

[73] J. V. B. Soares, J. J. G. Leandro, R. M. Cesar-Jr., H. F. Jelinek and M. J. Cree, "Retinal vessel segmentation using the 2-d Gabor wavelet and supervised classification," *IEEE Transaction on Medical Imaging,* vol. 25, no. 9, pp. 1214-1222, 2006.

[74] K. Rapantzikos, M. Zervakis and K. Balas, "Detection and segmentation of drusen deposits on human retina: potential in the diagnosis of age-related Macular degeneration," *Med. Imaging Anal.,* vol. 7, pp. 95-108, 2003.

[75] T.Walter and J. C. Klein, "Segmentation of color fundus images of the human retina: Detection of the optic disc and the vascular tree using morphological techniques," *in Proc. 2nd Int. Symp. Med. Data Anal.,* pp. 282-287, 2001.

[76] A. Aquino, M. E. Gegundez-Arias and D. Marin, "Detecting the Optic Disc Boundary in Digital Fundus Images Using Morphological, Edge Detection, and Feature Extraction Techniques," *IEEE Transactions on Medical Imaging,* vol. 29, pp. 1860-1869, 2010.

[77] S. H. Hordley, G. D. Finlayson, G. Schaefer and et al., "Illuminant and device invariant colour using histogram equalisation," Technical Report SYS-C02-16, UEA 2002, 2002.

[78] A. Osareh, *Automated identification of diabetic retinal exudates and the optic disc.*

PhD thesis. University of Bristol., 2004.

[79] R. C. Gonzalez and R. E. Woods, Digital image processing, Prentice Hall, second edition, 2002.

[80] A. Osareh, B. Shadgar and R. Markham, "A Computational-Intelligence-Based Approach for Detection of Exudates in Diabetic Retinopathy Images," *IEEE Transactions on Information Technology in Biomedicine,* vol. 13, no. 4, pp. 535-545, 2009.

[81] M. J. Cree, E. Gamble and D. Cornforth, "Colour Normalisation to Reduce Inter-Patient and Intra-Patient Variability in Microaneurysm Detection in Colour Retinal Images," *WDIC2005 ARPS Workshop on Digital Image Computing, Brisbane, Australia,* pp. 163-168, 2005.

[82] D. Usher, M. Dumskyj, M. Himaga, T. H. Williamson, S. Nussey and J. Boyce, "Automated detection of diabetic retinopathy in digital retinal images: a tool for diabetic retinopathy screening," *Diabet. Med.,* vol. 21, pp. 84-90, 2004.

[83] C. Sinthanayothin, J. F. Boyce, H. L. Cook and T. Williamson, "Automated localisation of the optic disc, fovea,and retinal blood vessels from digital colour fundus images," *Br. J. Ophthalmol.,* vol. 83, pp. 231-238, 1999.

[84] A. Chaudhuri, S. Chatterjee, N. Katz, M. Nelson and M. Goldbaum, "Detection of blood vessels in retinal images using two-dimensional matched filters," *IEEE Transactions on Medical Imaging,* no. 3, pp. 263-269, 1989.

[85] C. Sinthanayothin, "Image Analysis for Automatic Diagnosis of Diabetic Retinopathy.," *PhD Thesis, King's College London ,* 1999.

[86] J. Park, N. T. Kien and G. Lee, "Optic Disc Detection in Retinal Images using Tensor Voting and Adaptive Mean-Shift," *IEEE International Conference on Intelligent Computer Communication and Processing,* pp. 237-241, 2007.

[87] Z. Xiaohui and O. Chutatape, "Top-down and bottom-up strategies in lesion detection of background diabetic retinopathy," *IEEE Computer Society Conf. on Computer Vision and Pattern Recognition (CVPR),* pp. 422-428, 2005.

[88] D. Wu, M. Zhang, J. C. Liu and W. Bauman, "On the adaptive detection of blood

vessels in retinal images," *IEEE Trans. Biomed. Eng.,* vol. 53, no. 2, pp. 341-343, 2006.

[89] A. Youssif, A. Z. Ghalwash and A. Ghoneim, "Optic disc detection from normalized digital fundus images by means of a vessels' direction matched filter," *IEEE Transactions on Medical Imaging,* vol. 27, pp. 11-18, 2008.

[90] K. Zuiderveld, "Contrast limited adaptive histogram equalization," *Graphics gems,* vol. 4, pp. 474-485, 1994.

[91] A. Frame, P. E. Undrill, M. J. Cree, J. A. Olson, P. F. S. K. C. Mchardy and et al., "A comparison of computer based classification methods applied to the detection of microaneurysms in ophthalmic fluorescein angiograms," *Computers in Biology and Medicine,* vol. 28, pp. 225-238, 1998.

[92] M. Niemeijer, B. v. Ginneken, J. Staal, M. S. A. Suttorp-Schulten and M. D. Abràmoff, "Automatic Detection of Red Lesions in Digital Color Fundus Photographs," *IEEE Transactions on Medical Imaging,* vol. 24, pp. 584-592, 2005.

[93] S. Lu, "Accurate and Efficient Optic Disc Detection and Segmentation by a Circular Transformation," *IEEE Transactions on Medical Imaging,* vol. 30, no. 12, pp. 2126-2133, 2011.

[94] A. D. Fleming, S. Philip, K. A. Goatman, G. J. Williams, J. A. Olson and P. F. Sharp, "Automated detection of exudates for diabetic retinopathy screening," *Phys. Med. Biol.,* vol. 52, pp. 7385-7396, 2007.

[95] H. Leung, E. R. J. J. Wang and et al., "Relationships between age, blood pressure, and retinal vessel diameters in an older population," *Invest. Ophthalmol. Vis. Sci.,* vol. 44, pp. 2900-2904, 2003.

[96] P. M. A. V. Stanton, F. Mee, E. T. O'Brien and K. O. K, "A method for quantifying retinal microvascular alterations associated with blood pressure and age," *J. Hypertens.,* vol. 13, pp. 41-48, 1995.

[97] M. Niemeijer, M. D. Abràmoff and B. v. Ginneken, "Segmentation of the optic disc, macula and vascular arch in fundus photographs.," *IEEE Trans Med Imaging,* vol. 26, pp. 116-127, 2007.

[98] M. L. Baker, P. J. Hand, J. J. Wang and T. Y. Wong, "Retinal Signs and Stroke: Revisiting the Link Between the Eye and Brain," *Stroke,* vol. 39, no. 47, pp. 1371-1379, 2008.

[99] F. N. Doubal, P. E. Hokke and J. M. Wardlaw, "Retinal microvascular abnormalities and stroke: a systematic review," *Journal of neurology, neurosurgery, and psychiatry,* vol. 80, no. 2, pp. 158-165, 2009.

[100] N. Patton, T. Aslam, T. MacGillivray, A. Pattie, I. Deary and B. Dhillon, "Retinal vascular image analysis as a screening tool for cerebrovascular disease: a rationale based on homology between retinal and cerebral microvasculatures," *J. Anat. 206,* pp. 319-348, 2005.

[101] P. Hardy, D. R. Varma and S. Chemtoc, "Control of cerebral and ocular blood flow autoregulation in neonates," *Pediatric Clinics North Am. 44,* vol. 44, pp. 137-152, 1997.

[102] C. Delaey and J. v. d. Voorde, "Regulatory mechanisms in the retinal and choroidal circulation," *Ophthalmic Res.,* vol. 32, pp. 249-256, 2000.

[103] F. Zana and J. C. Klein, "A Multi-Modal Registration Algorithm of Eye Fundus Images Using Vessels Detection and Hough Transform," *IEEE Transactions on Medical Imaging ,* vol. 18, no. 5, pp. 419-428, 1999.

[104] K. A. Goatman, A. D. Fleming, S. Philip, G. J. Williams, J. A. Olson and P. F. Sharp, "Detection of New Vessels on the Optic Disc Using Retinal Photographs," *IEEE Transactions on Medical Imaging,* vol. 30, no. 4, pp. 972-979, 2011.

[105] L. Zhou, M. Rzeszotarski, L. Singerman and J. Chokreff, "The detection and quantification of retinopathy using digital angiograms," *IEEE Trans. Med. Imag.,* vol. 13, pp. 619-626, 1994.

[106] A. Hoover, V. Kouznetsova and M. Goldbaum, "Locating blood vessels in retinal images by piece-wise threshold probing of a matched filter response," *IEEE Trans. Med. Imag.,* vol. 19, pp. 203-210, 2000.

[107] L. Gang, O. Chutatape and S. M. Krishnan, "Detection and measurement of retinal vessels in fundus images using amplitude modified second-order Gaussian filter,"

IEEE Transactions on Biomedical Engineering, vol. 49, no. 2, pp. 168-172, 2002.

[108] J. A. Lowell, A. Hunter, D. Steel, A. Basu, R. Ryder and R. L. Kennedy, "Measurement of retinal vessel widths from fundus images based on 2-d modeling," *IEEE transactions on medical imaging,* vol. 23, no. 10, pp. 1196-1204, 2004.

[109] F. Zana and J. C. Klein, "Segmentation of vessel-like patterns using mathematical morphology and curvature evaluation," *IEEE Transactions on Image Processing,* vol. 10, pp. 1010-1019, 2001.

[110] M. S. Miri and A. Mahloofijar, "Retinal Image Analysis using Curvelet Transform and Multistructure Elements Morphology by Reconstruction," *IEEE Transactions on Biomedical Engineering,* vol. 58, no. 5, pp. 1183-1192, 2011.

[111] E. Candes, L. Demanet, D. Donoho and L. Ying, "Fast discrete curvelet transforms," *Multiscale Model. Simul.,* vol. 5, no. 3, pp. 861-899, 2006.

[112] K. Akita and H. Kuga, "A Computer Method of Understanding Ocular Fundus Images," *in Pattern Recognition,* vol. 15, no. 6, pp. 431-443, 1982.

[113] G. G. Gardner, D. Keating, T. H. Williamson and A. T. Elliott, "Automatic detection of diabetic retinopathy using an artificial neural network: A screening tool," *Br. J. Ophthalmol.,* vol. 80, no. 11, pp. 940-944, 1996.

[114] "Digital retinal images for vessel extraction," 2007. [Online]. Available: http://www.isi.uu.nl/Research/Databases/DRIVE/.

[115] B. Al-Diri, A. Hunter, D. Steel, M. Habib, T. Hudaib and S. Berry, "Review-A reference data set for retinal vessel profiles," *in Proc. 30th Annu. Int. Conf. IEEE Eng. Med. Biol. Soc.,* pp. 2262-2265, 2008.

[116] J. J. Staal, M. D. Abràmoff, M. Niemeijer, M. A. Viergever and B. v. Ginneken, "Ridge based vessel segmentation in color images of the retina," *IEEE Trans. Med. Imaging,* vol. 23, pp. 501-509, 2004.

[117] H. F. Jelinek, M. J. Cree, J. J. G. Leandro, J. V. B. Soares, R. M. Cesar-Jr. and A. Luckie, "Automated segmentation of retinal blood vessels and identification of proliferative diabetic retinopathy," *J. Opt. Soc. Am. A.,* vol. 24, no. 5, pp. 1448-

1456, 2007.

[118] E. Ricci and R. Perfetti, "Retinal Blood Vessel Segmentation Using Line Operators and Support Vector Classification," *IEEE Trans. Med. Imaging,* vol. 26, no. 10, pp. 1357-1365, 2007.

[119] M. Niemeijer, J. Staal, B. v. Ginneken, M. Loog and M. Abramoff, "Comparative study of retinal vessel segmentation methods on a new publicly available database," *in: SPIE Medical Imaging, Editor(s): J. Michael Fitzpatrick, M. Sonka, SPIE,* vol. 537, 2004.

[120] X. Jiang and D. Mojon, "Adaptive local thresholding by verification-based multithreshold probing with application to vessel detection in retinal images," *IEEE Trans. Pattern Anal. Mach. Intell.,* vol. 25, pp. 131-137, 2003.

[121] M. E. Martinez-Perez, A. D. Hughes, A. V. Stanton, S. A. Thom, N. Chapman, A. A. Bharath and K. H. Parker, "Retinal vascular tree morphology: a semi-automatic quantification," *IEEE Trans. Biomed. Eng.,* vol. 49, pp. 912-917, 2002.

[122] I. Liu and Y. Sun, "Recursive tracking of vascular networks in angiograms based on the detection-deletion scheme," *IEEE Trans. Med. Imag.,* vol. 12, pp. 334-341, 1993.

[123] Y. A. Tolias and S. M. Panas, "A Fuzzy Vessel Tracking Algorithm for Retinal Images Based on Fuzzy Clustering," *IEEE Trans. Med. Imaging,* vol. 17, no. 2, pp. 263-273, 1998.

[124] O. Chutatape, Z. Liu and S. M. Krishnan, "Retinal Blood Vessel detection and tracking by matched gaussian and kalman filters," *Proceedings of the 20th Annual International Conference of the IEEE Engineering in Medicine and Biology Society,* vol. 20, no. 6, 1998.

[125] M. Vlachos and E. Dermatas, "Multi-scale retinal vessel segmentation using line tracking," *Comp. Med. Imag. and Graph. ,* vol. 34, no. 3, pp. 213-227, 2010.

[126] A. Frame, M. M. Cree, J. Olson, K. McHardy, P. Sharp and J. V. Forrester, "Structural analysis of retinal vessels," *In Proceedings of the Sixth International conference on Image Processing and its applications,* vol. 2, pp. 824-827, 1996.

[127] A. Gooya, H. Liao, K. Matsumiya, K. Masamune, Y. Masutani and T. Dohi, "A variational method for geometric regularization of vascular segmentation in medical images," *IEEE Transactions on Image Processing,* vol. 17, pp. 1298-1312, 2008.

[128] B. Al-Diri, A. Hunter and D. Steel, "An Active Contour Model for Segmenting and Measuring Retinal Vessels," *Ieee Transactions on Medical Imaging,* vol. 28, pp. 1488-1497, 2009.

[129] B. Al-Diri and A. Hunter, "A ribbon of twins for extracting vessel boundaries," *in IFMBE Proc. 3rd Eur. Med. Biol. Eng. Conf. EMBEC'05,* vol. 11, no. 1, 2005.

[130] A. F. Frangi, W. J. Niessen, K. L. Vincken and M. A. Viergever, "Multiscale vessel enhancement filtering," *Medical Image Computing and Computer-Assisted Intervention - Miccai'98,* vol. 1496, 1998.

[131] Y. Yuan, Y. Luo and A. Chung, "VE-LLI-VO: Vessel Enhancement Using Local Line Integrals and Variational Optimization," *IEEE Transactions on Image Processing,* vol. 20, no. 7, pp. 1912-1924, 2011.

[132] J. Lowell, A. Hunter, D. Steel, A. Basu, R. Ryder, E. Fletcher and L. Kennedy, "Optic nerve head segmentation," *IEEE Trans. Med. Imag.,* vol. 23, no. 2, pp. 256-264, 2004.

[133] B. Kochner, D. Schuhmann, M. Michaelis, G. Mann and K.-H. Englmeier, "Course tracking and contour extraction of retinal vessels from color fundus photographs: Most e_cient use of steerable filters for model based image analysis," *In Proc. SPIE Medical Imaging,* pp. 755-761, 1998.

[134] A. Pinz, P. Bernogger, P. Datlinger and A. Kruger, "Mapping the Human Retina," *IEEE Trans. On Medical Imaging,* vol. 17, no. 4, pp. 606-619, 1998.

[135] S. C. Lee, Y. Wang and E. T. Lee, "Computer algorithm for automated detection and quantification of microaneurysms and hemorrhages (HMAs) in color retinal images," *Proc. SPIE 3663, 61,* 1999.

[136] H. Li and O. Chutatape, "Automatic Location of Optic disc in Retinal Images," *IEEE ICIP,* pp. 837-840, 2001.

[137] M. Lalonde, M. Beaulieu and L. Gagnon, "Fast and Robust Optic Disc Detection Using Pyramidal Decomposition and Hausdorff-Based Template Matching," *IEEE Transactions on Medical Imaging,* vol. 20, no. 11, 2001.

[138] A. Hoover and M. Goldbaum, "Fuzzy Convergence," *In the proceedings of IEEE Conference on Computer Vision and Pattern Recognition,* pp. 716-721, 1998.

[139] A. Osareh, M. Mirmehdi, B. Thomas and R. Markham, "Comparison of color spaces for optic disc localization in retinal images.," *Proc. 16th IEEE Int. Conf. Pattern Recognition,* vol. 1, pp. 743-746, 2002.

[140] M. Foracchia, E. Grisan and A. Ruggeri, "Detection of optic disc in retinal images by means of a geometrical model of vessel structure," *IEEE Transactions on Medical Imaging,* vol. 23, pp. 1189-1195, 2004.

[141] M. Foracchia, E. Grisan and A. Ruggeri, "Detection of vessel caliber irregularities in color retinal fundus images by means of fine tracking," *in EMBEC'02—IFMBE Proc. Series, Wien,* vol. 3, pp. 1558-1559, 2002.

[142] K. W. Tobin, E. Chaum, V. P. Govindasamy and T. P. Karnowski, "Detection of anatomic structures in human retinal imagery," *IEEE Transactions on Medical Imaging,* vol. 26, pp. 1729-1739, 2007.

[143] N. Otsu, "A threshold selection method from gray level histograms," *IEEE Trans. Syst., Man, Cybern.,* Vols. SMC-9, no. 1, pp. 62-66, 1979.

[144] A. E. Mahfouz and A. S. Fahmy, "Fast Localization of the Optic Disc Using Projection of Image Features," *IEEE Transactions on Image Processing,* vol. 19, pp. 3285-3289, 2010.

[145] T. Kauppi, V. Kalesnykiene, J. K. Kamarainen and et al., "DIARETDB0: Evaluation Database and Methodology for Diabetic Retinopathy Algorithms, Technical report".

[146] T. Kauppi, V. Kalesnykiene, J. K. Kamarainen and et al., "DIARETDB1 diabetic retinopathy database and evaluation protocol, Technical report".

[147] S. Lu and J. H. Lim, "Automatic Optic Disc Detection From Retinal Images by a Line Operator," *IEEE Transactions on Biomedical Engineering,* vol. 58, no. 1, pp.

88-94, 2011.

[148] C. Tomasi and R. Manduchi, "Bilateral Filtering for Gray and Color Images," *in Proc. IEEE Int. Conf. Comp. Vis.,* pp. 839-846, 1998.

[149] H. Yu, E. S. Barriga, C. Agurto, S. Echegaray, M. S. Pattichis, W. Bauman and P. Soliz, "Fast Localization and Segmentation of Optic Disk in Retinal Images Using Directional Matched Filtering and Level Sets," *IEEE Transactions on Information Technology in Biomedicine,* vol. 16, no. 4, pp. 644-657, 2012.

[150] M. Kass, A. Witkin, D and Terzopoulos, "Snakes: Active Contour Models," *International Journal of Computer Vision,* pp. 321-331, 1988.

[151] F. Mendels, C. Heneghan and J. Thiran, "Identification of the Optic Disc Boundary in Retinal Images Using Active Contours," *Proc. IMVIP Conference,* pp. 103-115, 1999.

[152] T.Walter and J. C. Klein, "Segmentation of color fundus images of the human retina: Detection of the optic disc and the vascular tree using morphological techniques," *Proc. 2nd Int. Symp. Med. Data Anal.,* pp. 282-287, 2001.

[153] H. Yu, M. S. Pattichis, C. Agurto and M. B. Goens, "A 3D Freehand Ultrasound System for Multi-view Reconstructions from Sparse 2D Scanning Planes," *BioMedical Engineering OnLine,* vol. 10, 2011.

[154] R. Chrástek, M. Wolf, K. Donath, G. Michelson and H. Niemann, "Optic disc segmentation in retinal images," *Bildverarbeitung für die Medizin 2002,* pp. 263-266, 2002.

[155] "Expert system for early automated detection of DR by analysis of digital retinal images project website. Huelva, Spain, Univ. Huelva," [Online]. Available: http://www.uhu.es/retinopathy .

[156] B. Lay, C. Baudoin and J. C. Klein, "Auomatic Detection of microaneurysms in retinopathy fluoro-angiogram," *Proceedings of the SPIE, 432,* vol. 165, 1983.

[157] C. E. Baudoin, B. J. Lay and J. C. Klein, "Automatic detection of microaneurysms in diabetic fluorescein angiographies," *Revue D'E´pide´miologie et de Sante Publique,* vol. 32, pp. 254-261, 1984.

[158] T. Spencer, R. P. Phillips, P. F. Sharp and et al., "Automated detection and quantification of microaneurysms in fluorescein angiograms," *Graefes Arch. Clin. Exp. Ophthalmol.,* vol. 230, no. 1, 1992.

[159] M. J. Cree, J. A. Olson, K. C. Hardy and et al., "A fully automated comparative microaneurysm digital detection system," *Eye,* vol. 11, no. 622, 1997.

[160] J. H. Hipwell, F. Strachan, J. A. Olson and et al., "Automated detection of microaneuryms in digital red-free photographs: A diabetic retinopathy screening tool," *Diabetic Medicine,* vol. 17, no. 8, 2000.

[161] C. Sinthanayothin, J. F. Boyce, T. H. Williamson and et al., "Automatic detection of diabetic retinopathy on digital fundus images," *Diabet. Med.,* vol. 19, pp. 105-112, 2002.

[162] A. D. Fleming, S. Philip, K. A. Goatman, J. A. Olson and P. F. Sharp, "Automated microaneurysm detection using local contrast normalization and local vessel detection," *IEEE Trans. Med. Imag.,* vol. 25, no. 9, pp. 1223-1232, 2006.

[163] G. Quellec, M. Lamard, P. M. Josselin, G. Cazuguel, B. Cochener and C. Roux, "Optimal wavelet transform for the detection of microaneurysms in retina photographs," *IEEE Trans. Med. Imag.,* vol. 27, no. 9, pp. 1230-1241, 2008.

[164] M. Niemeijer, B. v. Ginneken, M. J. Cree and et al., "Retinopathy Online Challenge: Automatic Detection of Microaneurysms in Digital Color Fundus Photographs," *IEEE Transactions on Medical Imaging,* vol. 29, no. 1, pp. 185-195, 2010.

[165] "Retinopathy Online Challenge," [Online]. Available: http://roc.healthcare.uiowa.edu/.

[166] B. Antal and A. Hajdu, "An ensemble-based system for microaneurysm detection and diabetic retinopathy grading," *IEEE Transactions on Biomedical Engineering,* vol. 59, no. 6, pp. 1720-1726, 2012.

[167] B. Zhang, X. Wu, J. You, Q. Li and F. Karray, "Detection of microaneurysms using multi-scale correlation coefficients," *Pattern Recognition,* vol. 43, no. 6, pp. 2237-2248, 2010.

[168] T. Walter and J. Klein, "Automatic detection of microaneurysms in color fundus images of the human retina by means of the bounding box closing," *Lecture Notes in Computer Science,* vol. 2526, pp. 210-220, 2002.

[169] S. Ravishankar, A. Jain and A. Mittal, "Automated feature extraction for early detection of diabetic retinopathy in fundus images," *Computer Vision and Pattern Recognition,* pp. 210-217, 2009.

[170] T. Walter, P. Massin, A. Arginay, R. Ordonez, C. Jeulin and J. C. Klein, "Automatic detection of microaneurysms in color fundus images," *Medical Image Analysis,* vol. 11, pp. 555-566, 2007.

[171] S. Abdelazeem, "Microaneurysm detection using vessels removal and circular hough transform," *Proceedings of the Nineteenth National Radio Science Conference,* pp. 421-426, 2002.

[172] I. Lazar, A. Hajdu and R. J. Quareshi, "Retinal microaneurysm detection based on intensity profile analysis," *8th International Conference on Applied Informatics,* 2010.

[173] N. Sondberg-madsen, C. Thomsen and J. M. Pena, "Unsupervised feature subset selection," *In Proceedings of the Workshop on Probabilistic Graphical Models for Classification,* pp. 71-82, 2003.

[174] R. Phillips, J. Forrester and P. Sharp, "Automated detection and quantification of retinal exudates," *Graefe's Arch. Clin. Exp. Ophthalmol.,* vol. 231, pp. 90-94, 1993.

[175] B. Ege, O. Hejlesen, O. Larsen, K. Moller, D. K. B.Jennings and D. Cavan, "Screening for diabetic retinopathy using computer based image analysis and statistical classication," *Comput. Meth. Programs Biomed.,* vol. 62, pp. 165-175, 2000.

[176] T. Walter, J. C. Klein, P. Massin and A. Erginay, "A Contribution of Image Processing to the Diagnosis of Diabetic Retinopathy-Detection of Exudates in Colour Fundus Images of the Human Retina," *IEEE Transactions on Medical Imaging,* vol. 21, pp. 1236-1243, 2002.

[177] A. Sopharak and B. Uyyanonvara, "Automatic exudates detection from diabetic

retinopathy retinal image using fuzzy c-means and morphological methods," *Proceedings of the Third IASTED International Conference Advances in Computer Science and Technology, Phuket, Thailand,* pp. 359-364, 2007.

[178] M. Niemeijer, S. R. Russell, M. A. Suttorp, B. v. Ginneken and M. D. Abràmoff, "Automated Detection and Differentiation of Drusen, Exudates, and Cotton-wool Spots in Digital Color Fundus Photographs for Early Diagnosis of Diabetic Retinopathy," *Invest. Ophthalmol. Vis. Sci.,* vol. 48, no. 5, pp. 2260-2267, 2007.

[179] C. I. Sánchez, M. Niemeijer, M. S.-S. M. S. A., M. D. Abràmoff and B. B. van Ginneken, "Improving hard exudate detection in retinal images through a combination of local and contextual information," *IEEE International Symposium on Biomedical Imaging: From Nano to Macro, 2010,* pp. 5-8, 2010.

[180] P. H. Gregson, R. C. S. Z. Shen and V. Kozousek, "Automated grading of venous beading," *Computers and Biomedical Research,* vol. 28, pp. 291-304, 1995.

[181] C. W. Yang, D. J. Ma, S. C. Chao, C. M. Wang, C. H. Wen, C. S. Lo, P. C. Chung and C. I. Chang, "Computer-aided diagnostic detection system of venous beading in retinal images," *Optical Engineering,* vol. 39, pp. 1293-1303, 2000.

[182] C. Agurto, H. Yu, V. Murray, M. S. Pattichis, S. Nemeth, S. Barriga and P. Soliz, "A Multiscale Decomposition Approach to Detect Neovascularization in the Optic Disc," *submitted to Transactions on Medical Imaging.*

[183] E. Chaum, T. P. Karnowski, V. P. Govindasamy, M. Abdelrahman and K. W. Tobin, "Automated Diagnosis of Retinopathy By Content-Based Image Retrieval," *Retina:November/December 2008.,* vol. 28, no. 10, pp. 1463-1477., 2008.

[184] C. Agurto, V. Murray, E. S. Barriga, S. Murillo, M. S. Pattichis, H. Davis, S. R. M. D. Abramoff and P. Soliz, "Multiscale AM-FM Methods for Diabetic Retinopathy Lesion Detection,"," *IEEE Transactions on Medical Imaging,* vol. 29, no. 2, pp. 502-512, 2010.

[185] A. Rocha, T. Carvalho, H. Jelinek, S. Goldenstein and J. Wainer, "Points of Interest and Visual Dictionaries for Automatic Retinal Lesion Detection," *IEEE Transaction on Biomedical Engineering ,* vol. 59, no. 8, pp. 2244-2253, 2012.

[186] H. Bay, A. Ess, T. Tuytelaars and L. V. Gool, "Speeded-up robust features (SURF)," *Comput. Vision Image Understanding,* vol. 110, no. 3, pp. 346-359, 2008.

[187] L. Giancardo, F. Meriaudeau, T. P. Karnowski, Y. Li, K. W. Tobin and E. Chaum, "Automatic retina exudates segmentation without a manually labelled training set," *Proc. IEEE Int. Symp. Biomed. Imag.: From Nano to Macro,* pp. 1396-1400, 2011.

[188] "The Hamilton Eye Institute Macular Edema Dataset (HEI-MED)," [Online]. Available: http://vibot.u-bourgogne.fr/luca/heimed.php.

[189] K. S. Deepak and J. Sivaswamy, "Automatic Assessment of Macular Edema From Color Retinal Images," *IEEE Transactions on Medical Imaging,* vol. 31, no. 3, pp. 766-776, 2012.

[190] N. Larsen, J. Godt, M. Grunkin, H. Lund-Andersen and M. Larsen, "Automated detection of diabetic retinopathy in a fundus photographic screening population," *Invest. Ophthalmol. Vis. Sci. ,* vol. 44, no. 2, pp. 767-771, 2003.

[191] M. Niemeijer, M. D. Abràmoff and B. v. Ginneken, "Information Fusion for Diabetic Retinopathy CAD in Digital Color Fundus Photographs," *IEEE Transactions on Medical Imaging,* vol. 28, no. 5, 2009.

[192] A. D. Fleming, K. A. Goatman, S. Philip, G. J. Prescott, P. F. Sharp and J. A. Olson, "Automated grading for diabetic retinopathy: a large-scale audit using arbitration by clinical experts," *Br J Ophthalmol. ,* 2010.

[193] L. Yannuzzi, K. Rohrer and L. Tindel, "Fluorescein angiography complication survey," *Ophthalmology,* vol. 93, pp. 611-617, 1986.

[194] M. D. Abramoff, M. Niemeijer and S. R. Rusell, "Automated detection of diabetic retinopathy: barriers to translation into clinical practice," *Expert Rev. Med. Devices,* vol. 7, no. 2, pp. 287-296, 2010.

[195] G. Quellec, M. Lamard, G. Cazuquel, L. Bekri, W. Daccache, C. Roux and B. Cochener, "Automated assessment of diabetic retinopathy severity using Content-Based Image retrieval in Multimodal Fundus Photographs," *Invest. Ophthalmol. Vis. Sci.,* vol. 52, no. 11, pp. 8342-8348, 2011.

[196] C. Agurto, S. Barriga, V. Murray, S.Nemeth, M. S. Pattichis, W. Bauman, G. Zamora and P. Soliz, "Automatic algorithm for detection of diabetic retinopathy pathologies," *Invest Ophthalmol Vis Sci.,* vol. 52, no. 8, pp. 5862-5871, 2011.

[197] "Fundus Photograph Reading Center, Dept. of Ophtalmology and Visual Sciences, University of Wisconsin, Madison," [Online]. Available: http://eyephoto.ophth.wisc.edu/ResearchAreas/Diabetes/DiabStds.htm.

[198] M. S. Pattichis and A. C. Bovik, "Analyzing image structure by multidimensional frecuency modulation," *IEEE Trans. Pattern Anal. Mach. Intell.,* no. 5, pp. 753-766, 2007.

[199] J. Havlicek, "AM-FM image models," *Ph.D. Dissertation, The University of Texas at Austin,,* 1996.

[200] C. Agurto, S. Murillo, V. Murray and et al., "Detection and Phenotyping of Retinal Disease using AM-FM Processing for Feature Extraction".," *42nd IEEE Asilomar Conference on Signals, Systems and Computers,* 2008.

[201] C. Agurto, S. Barriga, V. Murray, M. S. Pattichis, H. Davis and P. Soliz, "Effects of Image Compression and Degradation on an Automated Diabetic Retinopathy Screening Algorithm," *SPIE Medical Imaging,* 2010.

[202] E. S. Barriga, V. Murray, C. Agurto and et a. ", "Automatic System for Diabetic Retinopathy Screening Based on AM-FM, Partial Least Squares, and Support Vector Machines," *IEEE International Symposium on Biomedical Imaging,* 2010.

[203] "2010: (Agurto, C. et al. IOVS 2010;51: ARVO abstract 1793)".

[204] C. Agurto, S. Barriga, V. Murray, M. S. Pattichis, G. Zamora and P. Soliz, "Toward comprehensive detection of sight threatening retinal disease using a multiscale AM-FM methodology," *SPIE Medical Imaging. ,* 2011.

[205] J. Kinyoun, F. Barton, M. Fisher, L. Hubbard, L. Aiello and F. Ferris, "Detection of diabetic macular edema: ophthalmoscopy versus photography EarlyTreatment Diabetic Retinopathy Study Report Number 5, The ETDRS Research Group," *Ophthalmology,* vol. 96, pp. 746-750, 1989.

[206] C. J. Welty, A. Agarwal, L. M. Merin and A. Chomsky, "Monoscopic versus

stereoscopic photography in screening for clinically significant macular edema," *Ophthalmic Surg Lasers Imaging,* vol. 37, pp. 524-526, 2006.

[207] C. J. Rudnisky, M. T. Tennant, A. d. Leon, B. J. Hinz and M. Greve, "Benefits of stereopsis when identifying clinically significant macular edema via tele-ophthalmology," *Can J Ophthalmol.,* vol. 41, no. 6, pp. 727-732, 2006.

[208] S. Resnikoff and et al., "Global data on visual impairment in the year 2002," *Bull. World Health Organ.,* vol. 82, pp. 844-851, 2004.

[209] S. L. Angewandte, Statistik: Anwendung statistischer Methoden, Berlin: 7 ed. Springer,, 1992.

[210] J. Cohen, "A coefficient of agreement for nominal scales," *Educational and Psychological Measurement,* vol. 20, pp. 213-220, 1960.

[211] W. Chen and B. D. Gallas, "Training variability in the evaluation of automated classifers," *SPIE Medical Imaging 2010: Computer-Aided Diagnosis,* 2010.

[212] B. Sander, J. Godt, H. Lund-Andersen and et al., "Automatic Detection of Fundus Photographic Red Lesions in Diabetic Retinopathy," *ARVO poster, 4338,* 2001.

[213] A. Sharma, "Automated Depth analysis of optic nerve head from stereo fundus image," *Master thesis, University of Texas Tech..*

[214] S. M. Pizer, E. P. Amburn, J. D. Austin and et al., "Adaptive histogram equalization and its variations," *Computer Vision, Graphics, and Image Processing,* vol. 39, no. 3, pp. 355-368, 1987.

[215] S. de Jong, "SIMPLS: An Alternative Approach to Partial Least Squares Regression," *Chemometrics and Intelligent Laboratory Systems,* vol. 18, pp. 251-263, 1993.

[216] Prevent Blindness America and National Eye Institute. , "Vision Problems in the U.S.: Prevalence of Adult Vision Impairment and Age-Related Eye Disease in America.," 2012.

[217] F. K. Sutter, M. C. Gillies and H. Helbig, "Diabetic Macular Edema in Medical Retina," *(Editors FG Holze, RF Spaide),* pp. 131-146, 2007.

[218] Early Treatment diabetic Retinopathy Study research group, "Photocoagulation for

diabetic macular edema," *Arch Ophthalmol.,* vol. 103, no. 12, pp. 1796-1806, 1985.

[219] J. Kanski., "Clinical Ophthalmology: A Systematic Approach," *5th ed. Philadelphia, PA: Butterworth Heinemann Elsevier,* 2007.

[220] M. E. Tyler, L. D. Hubbard, K. Boydston and A. Pugliese, "Characteristics of Digital Fundus Camera Systems Affecting Tonal Resolution in Color Retinal Images".

[221] N. M. Salem and A. K. Nandi, "Novel and adaptive contribution of the red channel in pre-processing of colour fundus images," *in Journal of the Franklin Institute,* 2007.

[222] R. M. Haralick, K. Shanmugan and I. Dinstein, "Textural Features for Image Classification," *IEEE Transactions on Systems, Man, and Cybernetics,* vol. 3, pp. 610-662, 1973.

[223] A. R. Bhavsar, G. G. Emerson, M. V. Emerson and D. J. Browning, "Diabetic Retinopathy," in *Epidemiology of Diabetic Retinopathy*, New York, Springer, 2010.

[224] L. M. Aiello, L. P. Aiello and J. D. Cavallerano, "Ocular complications of diabetes mellitus," *In: Kahn CR, Weir GC, King GL, Jacobson AM, Moses AC, Smith RJ (ed). Joslin's Diabetes Mellitus,* pp. 901-924, 2005.

[225] R. Klein, B. E. Klein, S. E. Moss and et al., "The Wisconsin Epidemiologic Study of Diabetic Retinopathy. X. Four-year incidence and progression of diabetic retinopathy when age at diagnosis is 30 years or more," *Arch Ophthalmol 1989,* vol. 107, pp. 244-249, 1989.

[226] N. R. Pal and S. K. Pal, "Entropic Thresholding," *Signal Processing,* vol. 16, pp. 97-108, 1989.

[227] P. Perona and J. Malik, "Scale-Space and Edge Detection Using Anisotropic Diffusion," *IEEE Transactions on Pattern Analysis and Machine Intelligence,* vol. 12, no. 7, pp. 629-639, 1990.

[228] A. Avakian, R. E. Kalina, E. H. Sage, A. H. Rambhia, K. E. Elliott, E. L. Chuang, J. I. Clark, J. Hwang and P. Pasons-Wingerter, "Fractal analysis of region-based vascular changes in the normal and non-proliferative diabetic retina," *Current Eye*

Research, vol. 24, no. 4, pp. 274-280, 2002.

[229] T. MacGillivray and N. Patton, "A reliability study of fractal analysis of the skeletonised vascular network using the 'box-counting' technique," *in Proceedings of the 28th IEEE EMBS Annual International Conference,* p. 4445–4448, 2006.

[230] V. Vapnik, Statistical Learning Theory, New York, 1998.: John Wiley and Sons, Inc., 1998.

[231] P. Refaeilzadeh, L. Tang and H. Liu, "Cross Validation," *Encyclopedia of Database Systems, Springer,* 2009.

[232] R. Klein, B. E. Klein, S. E. Moss and et al., "The wisconsin epidemiologic study of diabetic retinopathy: XVII. The 14 year incidence and progression of diabetic retinopathy and associated risk factors in type I," *Ophthalmology, 105, 1801,* 1998.